AD-A042 986 ACUREX CORP MOUNTAIN VIEW CALIF AEROTHERM DIV F/G 14/2
FEASIBILITY OF A HYBRID HYPERVELOCITY LAUNCHER.(U)
JAN 77 L M COHEN, T J DAHM, J D WATSON DNA001-76-C-0407
UNCLASSIFIED AEROTHERM-TR-77-238(7260) DNA-4226F NL

1 OF 2
AD
A042986

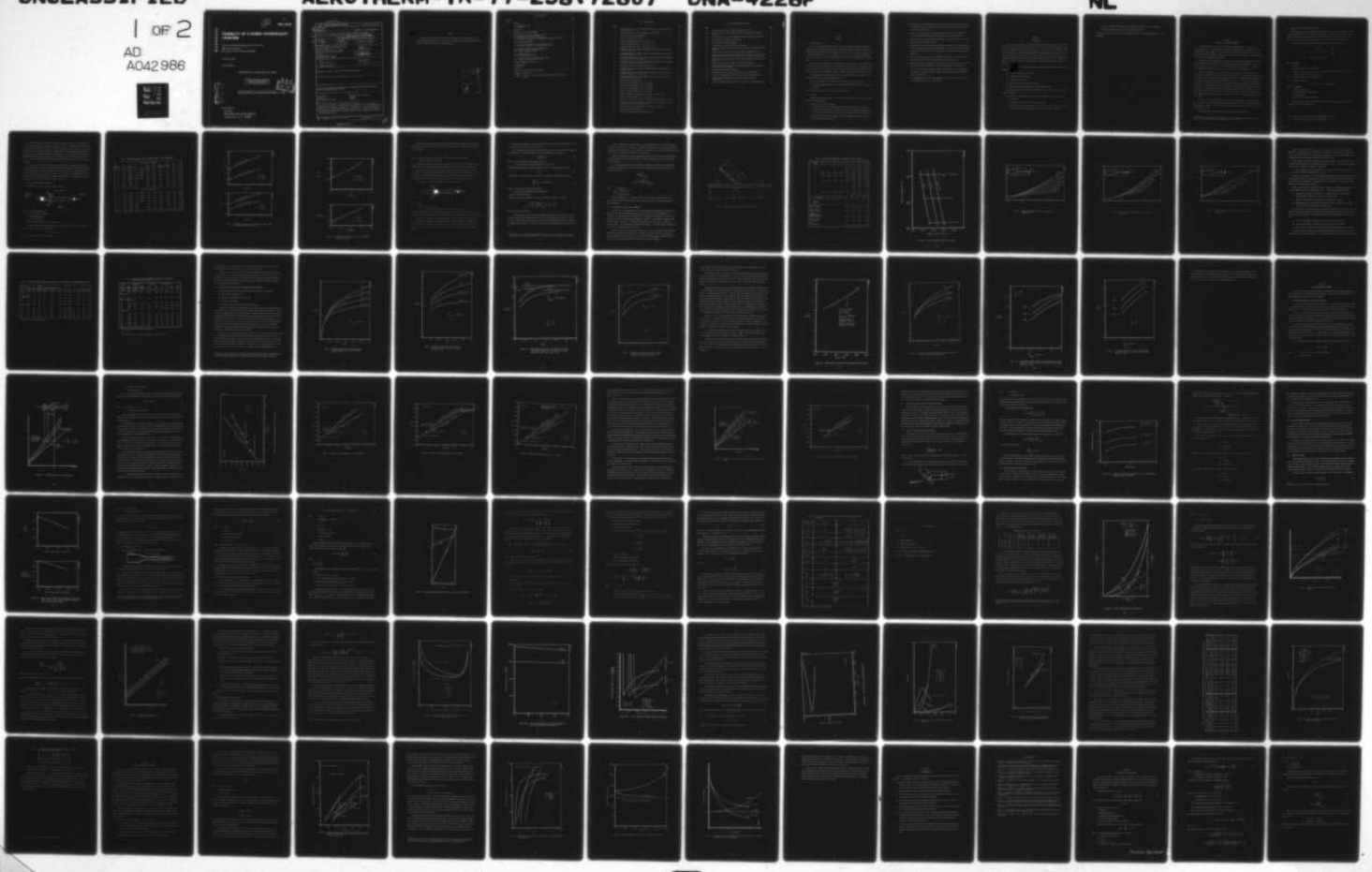

DNA 4226F

FEASIBILITY OF A HYBRID HYPERVELOCITY LAUNCHER

Acurex Corporation/Aerotherm Division
485 Clyde Avenue
Mountain View, California 94042

January 1977

Final Report

CONTRACT No. DNA 001-76-C-0407

THIS WORK SPONSORED BY THE DEFENSE NUCLEAR AGENCY
UNDER RDT&E RMSS CODE B34207T464 N99QAXAA12944 H2590D.

Prepared for
Director
DEFENSE NUCLEAR AGENCY
Washington, D. C. 20305

UNCLASSIFIED

SECURITY CLASSIFICATION OF THIS PAGE (When Data Entered)

REPORT DOCUMENTATION PAGE

READ INSTRUCTIONS BEFORE COMPLETING FORM

1. REPORT NUMBER: DNA 4226F	2. GOVT ACCESSION NO.
3. RECIPIENT'S CATALOG NUMBER	
4. TITLE (and Subtitle): FEASIBILITY OF A HYBRID HYPERVELOCITY LAUNCHER	5. TYPE OF REPORT & PERIOD COVERED: Final Report
6. PERFORMING ORG. REPORT NUMBER: TR-77-238 (7260)	
7. AUTHOR(s): L. M. Cohen, T. J. Dahm, J. D. Watson, A. D. Anderson	8. CONTRACT OR GRANT NUMBER(s): DNA 001-76-C-0407
9. PERFORMING ORGANIZATION NAME AND ADDRESS: Acurex Corporation/Aerotherm Division, 485 Clyde Avenue, Mountain View, California 94042	10. PROGRAM ELEMENT, PROJECT, TASK AREA & WORK UNIT NUMBERS: Subtask N99QAXAA129-44
11. CONTROLLING OFFICE NAME AND ADDRESS: Director, Defense Nuclear Agency, Washington, D.C. 20305	12. REPORT DATE: January 1977
	13. NUMBER OF PAGES: 110
14. MONITORING AGENCY NAME & ADDRESS (if different from Controlling Office): 194 p.	15. SECURITY CLASS (of this report): UNCLASSIFIED
	15a. DECLASSIFICATION/DOWNGRADING SCHEDULE

16. DISTRIBUTION STATEMENT (of this Report)

Approved for public release; distribution unlimited.

17. DISTRIBUTION STATEMENT (of the abstract entered in Block 20, if different from Report)

18. SUPPLEMENTARY NOTES

This work sponsored by the Defense Nuclear Agency under RDT&E RMSS Code B34207T464 N99QAXAA12944 H2590D.

19. KEY WORDS (Continue on reverse side if necessary and identify by block number)

Light Gas Gun
Projectile
Hypervelocity Launcher
Reentry Vehicle Studies
Erosion
Ablation

20. ABSTRACT (Continue on reverse side if necessary and identify by block number)

This report documents an investigation of the feasibility of a hybrid hypervelocity launcher. Included are evaluations of: (1) the thermodynamic performance of the working medium, (2) the ballistic cycles necessary to achieve the desired projectile muzzle velocities, (3) possible loss mechanisms which can degrade ballistic performance, and (4) material response to predicted heat loads.

DD FORM 1 JAN 73 1473 EDITION OF 1 NOV 65 IS OBSOLETE

UNCLASSIFIED

SECURITY CLASSIFICATION OF THIS PAGE (When Data Entered)

404 435

PREFACE

Aerotherm wishes to express its appreciation to Physics International Company. Their friendly cooperation, provided by Mr. Kerry Seifert, in supplying all requested information was invaluable to the execution of the work documented herein.

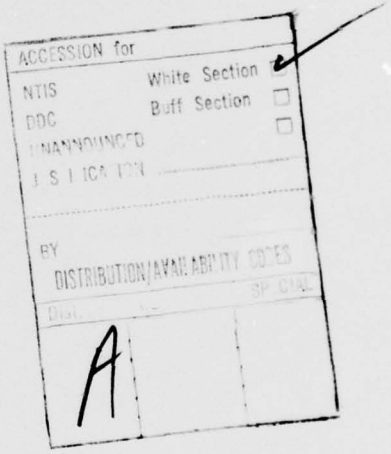

TABLE OF CONTENTS

Section		Page
1	SUMMARY	4
	1.1 Background and Scope	4
	1.2 Conclusions	4
2	INTRODUCTION	7
3	ESTIMATES OF PI LAUNCHER PERFORMANCE	9
	3.1 Shocked Gas State in the Explosive Drivers	10
	3.2 Calculation of Reservoir Conditions	11
	3.3 Calculation of Ballistic Cycle Performance	17
	3.4 Sensitivity of Muzzle Velocity to Reservoir and Launcher Parameters	27
4	FACTORS DEGRADING PERFORMANCE	38
	4.1 Gas Conditions Generated by the Explosive Drivers	38
	4.2 Injection of Shocked Gas into the Compressor Section	48
	4.2.1 Injection Through a Standing Oblique Shock	48
	4.2.2 Subsonic Injection of Driver Gases	49
	4.2.3 Driver Termination Dynamics	52
	4.3 Projectile Friction	52
	4.4 Barrel Boundary Layer Effects	54
	4.4.1 Momentum Losses Due to Boundary Layer Closure	55
	4.4.2 Energy Losses Due to Heat Transfer	69
5	MATERIAL RESPONSE TO HEAT TRANSFER	82
6	RECOMMENDATIONS	90
	REFERENCES	91
	APPENDIX A — EQUATION OF STATE FOR HYDROGEN	93
	REFERENCES FOR APPENDIX A	101
	APPENDIX B — EXAMPLE OF CALCULATION PROCEDURE FOR HYBRID LAUNCHER BALLISTIC CYCLES	103

LIST OF ILLUSTRATIONS

Figure		Page
1	Mach number and density ratio dependence on shock velocity, with and without covolume effects	13
2	Pressure and particle velocity dependence on shock velocity	14
3	PI hybrid two stage launcher geometry	18
4	Loci of possible reservoir states	20
5	Launcher performance with $D_{21} = 2$ and $\gamma_{isent} = 1.1$	21
6	Launcher performance with $D_{21} = 2$ and $\gamma_{isent} = 1.4$	22
7	Launcher performance with $D_{21} = 2$ and $\gamma_{isent} = 1.667$	23
8	Performance sensitivity to barrel dimensions for various ratios of gas mass to projectile mass, $p_4 = 5$ kb	28
9	Performance sensitivity to barrel dimensions for various ratios of gas mass to projectile mass, $p_4 = 10$ kb	29
10	Performance sensitivity to ratio of gas mass to projectile mass for representative scaled reservoir sound speeds, $p_4 = 5$ kb	30
11	Performance sensitivity to ratio of gas mass to projectile mass for representative scaled reservoir sound speeds, $p_4 = 10$ kb	31
12	Performance sensitivity to maximum piston velocity	33
13.	Performance sensitivity to reservoir pressure for various ratios of gas mass to projectile mass	34
14	Performance sensitivity to scaled reservoir sound speed for various ratios of gas mass to projectile mass, $p_4 = 5$ kb	35
15	Performance sensitivity to scaled reservoir sound speed for various ratios of gas mass to projectile mass, $p_4 = 5$ kb	36
16	Ideal explosive driver operation	39
17	Explosive driver performance for PI, Test Number 5	41
18	Explosive driver performance for PI, Test Number 6	42
19	Explosive driver performance for PI, Test Number 7	43
20	Explosive driver performance for PI, Test Number 8	44
21	Schematic diagram of jet particle trajectories in a jetting driver	46
22	Explosive driver performance for PI, Test Number 1	47
23	Influence of driver shock velocity on oblique shock turning angle at injection	50
24	Choked area and mass flow degradation resulting from a normal shock returning back through the driver cross sectional area	53
25	Turbulent boundary layer shape factors, 1/7 power velocity profile	57
26	Generalized ballistic performance	64
27	Growth of maximum boundary layer momentum thickness	66

LIST OF ILLUSTRATIONS (Concluded)

Figure		Page
28	Projectile locations at the times of boundary layer closure	68
29a	Axial distribution of heat transfer coefficient at the time of projectile expulsion	71
29b	Axial distribution of recovery enthalpy at the time of projectile expulsion	72
30a	Time histories of heat transfer coefficient	73
30b	Time histories of recovery enthalpy	75
31	Time histories of total barrel heat transfer rates	76
32	Influence of type of ballistic cycle and muzzle velocity on total heat load to the barrel	77
33	Effect of heat transfer on projectile velocity, method of Reference 11	80
34	Thermal response of three barrel surface materials to convection near the chambrage plane. CBPL, conditions of Figure 30 (i.e., 3 km/sec, p_o = 1000 atm)	84
35	Tungsten thermal response at two locations near the chambrage plane, CBPL and SWL cycles	86
36	Stagnation enthalpy history input to calculation of Figure 35	87
37	Pressure histories associated with an 86 gram projectile muzzle velocity of 6 km/sec, 762 cm barrel length	88
A-1	Modified mollier diagram for hydrogen	A-4
A-2	Pressure dependence on density for hydrogen at various temperatures	A-5
A-3	Dissociation dependence on density for hydrogen at various temperatures	A-6
A-4	Acoustic velocity dependence on density for hydrogen at various temperatures	A-7
A-5	Isentropic index dependence on density for hydrogen at various temperatures	A-8

SECTION 1

SUMMARY

1.1 BACKGROUND AND SCOPE

In 1973 a concept for obtaining higher performance from two-stage light gas launchers was proposed by Physics International Company (PI). The method used explosive drivers to shock heat a light-gas working medium and inject it ahead of a compressor piston. Calculations indicated that a significant improvement in ballistic performance would result, making possible the launching of projectiles three to four times more massive than can be done with existing launchers of the same bore.

From April 1974 through August 1975, PI conducted a program (Reference 1) to demonstrate the concept with a launcher of 2.54-cm bore. The objective of that program was to launch 86-gm projectiles to velocities in the range of 3 to 6 km/sec. However, the highest velocity obtained in eight tests was 2.5 km/sec and the compressor chamber and barrel of the launcher were damaged by erosion.

The Aerotherm Division of Acurex Corporation investigated the PI launcher concept for the Defense Nuclear Agency. Aerotherm's objectives were:

- Evaluate thermodynamic and gasdynamic limitations of the PI hybrid launcher
- Recommend configuration and materials changes that promise to significantly improve performance

This report presents the results of Aerotherm's investigations.

1.2 CONCLUSIONS

The observed performance shortfall is ascribed to the particular design of the PI apparatus, and not to the hybrid concept.

Specifically, Aerotherm has concluded:

- The most important factor in performance shortfall observed with the PI launcher was insufficient working medium for the ballistic cycle. The design mass of hydrogen was too small, and a significant quantity failed to be injected into the compressor tube.
- The maximum attainable kinetic energy of the 75-mm compressor piston is marginal for achieving 6 km/sec muzzle velocities

- The junction block configurations exceeded the maximum angle(s) for favorable injection of the driver gas, causing reduction of the driver gas injection rate for large driver to compressor diameter ratios
- Driver injection and termination dynamics resulted in a significant fraction of the driver gases being trapped between the termination flanges and injection ports
- The explosive drivers jetted, which may have led to contamination of the driver gas and particle erosion of internal surfaces
- Momentum losses through the boundary layer within the barrel severely limited acceleration of the projectiles beyond 300 barrel diameters. PI's design calculations excluded viscosity effects, and because of this, the barrel length chosen was much too large (576 diameters)
- Heat losses were not a major cause of performance shortfall; they could account for no more than about one-tenth of the observed reduction of muzzle velocity
- Computed heat loads are high enough to cause melting of the steel barrel's inner surface, particularly near the chambrage plane. Melting was observed in the experiments.
- If used in conjunction with properly tailored ballistic cycles, barrel inserts/liners of tungsten (or possibly an ablative material such as carbon) can protect the barrel from destructive melting
- The thermodynamic description of the hydrogen driver gas must account for molecular co-volume and vibration as well as dissociation

SECTION 2

INTRODUCTION

The PI projectile launcher is a hybrid design incorporating a shock-heated light-gas working medium with a conventional two-stage ballistic cycle. In principle, the preheated working medium leads to substantially higher reservoir energy densities for a given volume of compressor section. This in turn leads to lower pressure gradients throughout the launcher for any ballistic cycle, including a constant base pressure cycle. As a result, substantially higher muzzle velocities for large mass to diameter projectiles are possible within the pressure limitations of launcher design. With the PI launcher, however, ballistic performance, gauged by projectile muzzle velocities, was deficient.

In an effort to determine the causes for performance shortfall, the following possible loss mechanisms were identified:

- Improperly operating explosive drivers
- Incompatible injection geometry
- Projectile/barrel friction
- Momentum losses to the barrel boundary layer
- Heat losses through the boundary layer and consequent erosion

This report documents the Aerotherm investigation of the feasibility of the PI projectile launcher as follows:

- Hydrogen is characterized as a Van der Waals gas subject to molecular vibration and dissociation
- Baseline predictions define ideal launcher performance
- Parametric results show performance sensitivities to the amount of working medium available for ballistic cycles and to various other important ballistic parameters

- The loss mechanisms discussed above are evaluated for impact on ballistic performance
- Material response is determined for the predicted heat loads

On the basis of these considerations, design modifications to achieve desired performance levels are recommended.

SECTION 3

ESTIMATES OF PI LAUNCHER PERFORMANCE

This section describes a method for estimating the performance of the PI launcher under idealized conditions. This method leads to reasonably accurate estimates of projectile velocity for representative launcher conditions and is used to assess the sensitivity of muzzle velocity to variations of key ballistic parameters. These idealized performance estimates define the framework within which various loss mechanisms can be evaluated.

The method of estimating performance is based on a simple thermodynamic approach to describe the shock compression and injection of gas by the explosive drivers, the compression of the gas by the first stage piston to a reservoir state, and the acceleration of the projectile. Throughout these calculations, an accurate equation of state for hydrogen is used (see Appendix A).

Performance estimates are made by considering the operation of the launcher system. The system begins at an ambient state characterized by a mass of gas at initial pressure and temperature. The explosive drivers are then actuated to process the driver gas, increasing the energy of the gas by an amount equal to the work done by the collapsing driver, $p\Delta V$. The driver gas is considered to be completely injected into the compressor section and the compressor piston then covers the driver gas injection ports. The compressor piston, having been accelerated into a vacuum prior to reaching these ports, will add energy to the gas by compression as it decelerates to zero velocity. In this model, the compressor piston decelerates to rest before the projectile is allowed to accelerate. The final compressed state is then used to estimate projectile velocity with a preburned-propellant ballistic model.

In reality, the projectile begins to accelerate before the compressor piston decelerates to rest. Consequently, the method used here somewhat overestimates the reservoir pressures, temperatures, and sound speeds. However, for a sufficiently long launch tube, the estimated muzzle velocity using this method is accurate.*

The various steps in the performance calculation are now described in detail.

---

*Future performance estimates should be made using a 1-1/2-D finite difference code incorporating the more accurate equation of state for hydrogen used in this report.

3.1 SHOCKED GAS STATE IN THE EXPLOSIVE DRIVERS

The explosive drivers can be modeled as a constant velocity piston (at the detonation velocity of the explosive) which drives a shock wave into the driver gas. Knowing the initial driver gas pressure and temperature and by measuring the shock velocity, the gas conditions behind the shock can be calculated by solving the conservation equations and the equation of state of the gas.

The conservation equations across the shock, expressed in shock coordinates are:

$$\left.\begin{aligned} \rho_1 v_1 &= \rho_2 v_2 \\ p_2 + \rho_2 v_2^2 &= p_1 + \rho_1 v_1^2 \\ \beta_2 \frac{p_2}{\rho_2} + \frac{v_2^2}{2} &= \beta_1 \frac{p_1}{\rho_1} + \frac{v_1^2}{2} \end{aligned}\right\} \qquad (1)$$

where p = pressure

ρ = density

v = particle velocity in shock coordinates

$\beta = \frac{e + p/\rho}{p/\rho}$, (enthalpy parameter introduced for convenience to preserve the ideal form of the shock jump relations for a nonideal gas)

and e = specific internal energy (see Appendix A)

The equation of state is:

$$p = p(T, \alpha, \rho, a, b, \theta_v) \qquad \text{(see Appendix A)}$$

where T = temperature

α = degree of dissociation

a = Van der Waal's attraction constant

b = covolume constant

θ_v = characteristic vibrational temperature

These equations are solved by an iterative process to obtain p_2, ρ_2, e_2, and v_2, and transformed back to laboratory coordinates by

$$u_2 = v_2 + s$$

$$s = v_1$$

where u_2 = particle velocity behind the shock in laboratory coordinates

s = observed shock velocity in laboratory coordinates

The shocked gas states for various shock wave velocities (6.0 km/sec $\leq$ s $\leq$ 10.0 km/sec) into hydrogen initially at 300°K and 350 psia are summarized in Table 1. Intermolecular attraction and dissociation are negligible, but covolume and molecular vibration play an important role. Pressure behind the shock is relatively insensitive to covolume forces, but flow Mach number and density ratio across the shock are significantly affected by covolume forces. The calculated variation of flow Mach number and density ratio with shock velocity are shown in Figure 1 with and without covolume forces. Calculated particle velocity and shocked pressure variation with shock velocity are shown in Figure 2.

When the explosive driver is operated within its range of ideal performance, the particle velocity behind the shock is equal to the detonation velocity of the explosive and conditions behind the shock are constant. PI used nitromethane explosive (D = 6.25 km/sec). For hydrogen initially at 300°K and 350 psia, the shock velocity should be 7.8 km/sec; thus, in subsequent launcher performance estimates, the explosive drivers are assumed to operate ideally and shocked gas conditions corresponding to a driver's shock velocity of 7.8 km/sec are used.

3.2 CALCULATION OF RESERVOIR CONDITIONS

The initial state of the PI launcher system is taken as

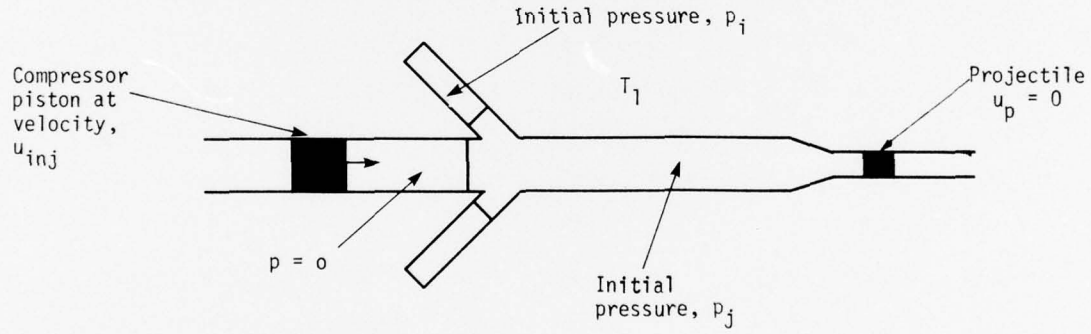

where p_i = initial driver pressure

p_j = initial compressor pressure

T_1 = ambient temperature

u_p = projectile velocity

u_{inj} = compressor piston velocity at injection port

From the initial temperature and loading pressures the mass of gas, G, can be determined. The initial energy of the system is then given by:

$$E_i = 5/2\ RT_1 \times G \qquad (2)$$

where R = gas constant of molecular hydrogen

TABLE 1. CONDITIONS BEHIND A SHOCK IN HYDROGEN INITIALLY AT 350 PSI AND 300°K

s (km/sec)	T_2 (°K)	ρ_2 (gm/cm^3)	P_2 kb	α_2	γ_{adiab}	γ_{isent}	c_2 (km/sec)	u_2 (km/sec)	M_2	ρ_2/ρ_1
Full Equation of State										
9.0	2699	0.0104	1.31	0.0009	1.410	1.497	4.35	7.31	1.68	5.31
8.5	2467	0.0101	1.16	0.0004	1.415	1.497	4.15	6.86	1.65	5.20
8.0	2239	0.0099	1.03	0.0001	1.420	1.501	3.96	6.42	1.62	5.07
7.5	2019	0.0096	0.90	<0.0001	1.424	1.503	3.75	5.98	1.59	4.95
7.0	1810	0.0094	0.78		1.427	1.509	3.55	5.55	1.56	4.81
6.5	1610	0.0091	0.67		1.431	1.514	3.35	5.11	1.53	4.67
6.0	1422	0.0088	0.57		1.433	1.519	3.15	4.67	1.48	4.51
Covolume Suppressed										
9.0	2804	0.0116	1.34	0.0012	1.358	1.316	3.90	7.49	1.92	5.96
8.5	2561	0.0113	1.19	0.0005	1.364	1.321	3.74	7.04	1.88	5.81
8.0	2324	0.0110	1.05	0.0002	1.369	1.327	3.57	6.59	1.85	5.66
7.5	2096	0.0107	0.92	<0.0001	1.375	1.334	3.40	6.14	1.81	5.50
7.0	1878	0.0104	0.80		1.380	1.343	3.22	5.69	1.77	5.31
6.5	1671	0.0100	0.69		1.385	1.352	3.05	5.24	1.72	5.12
6.0	1476	0.0097	0.58		1.388	1.362	2.88	4.79	1.66	4.94

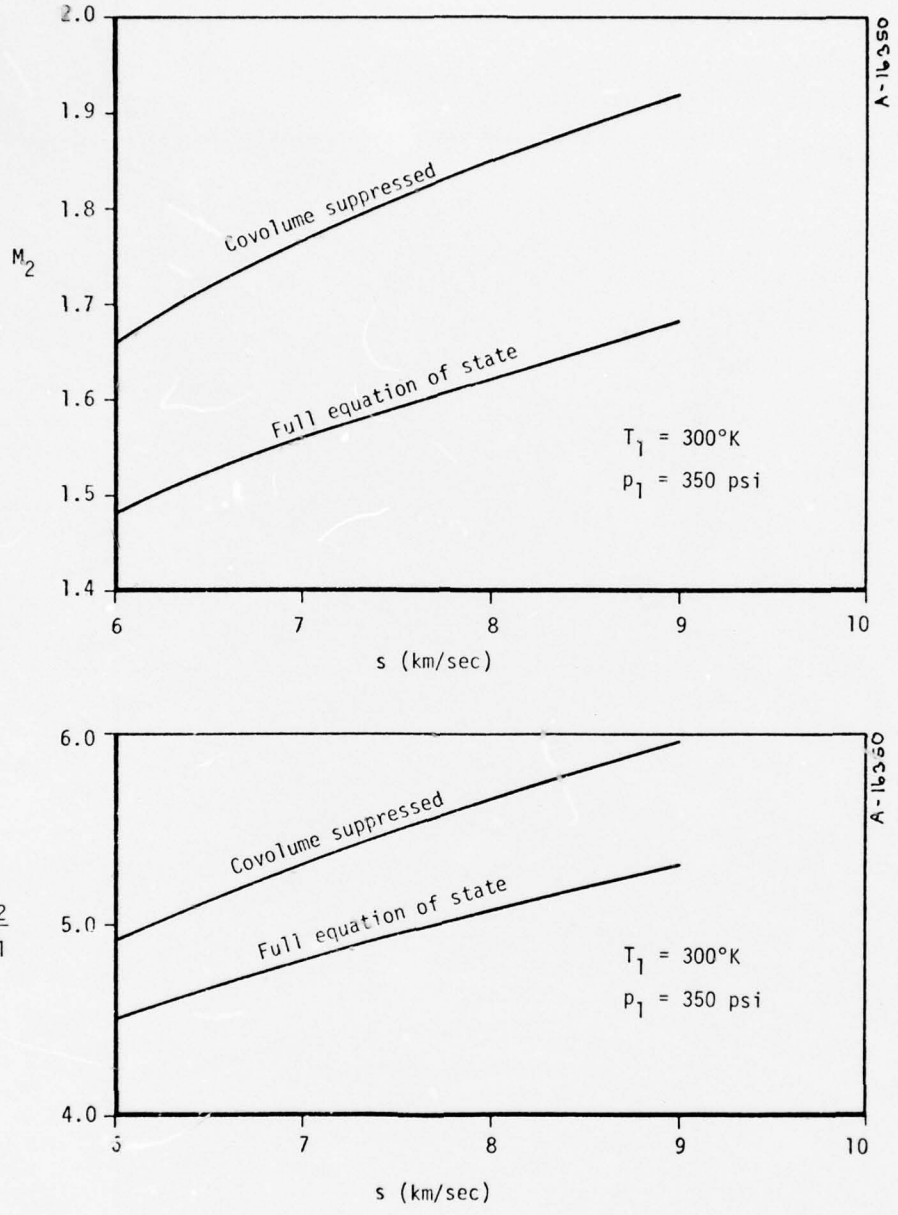

Figure 1. Mach number and density ratio dependence on shock velocity, with and without covolume effects.

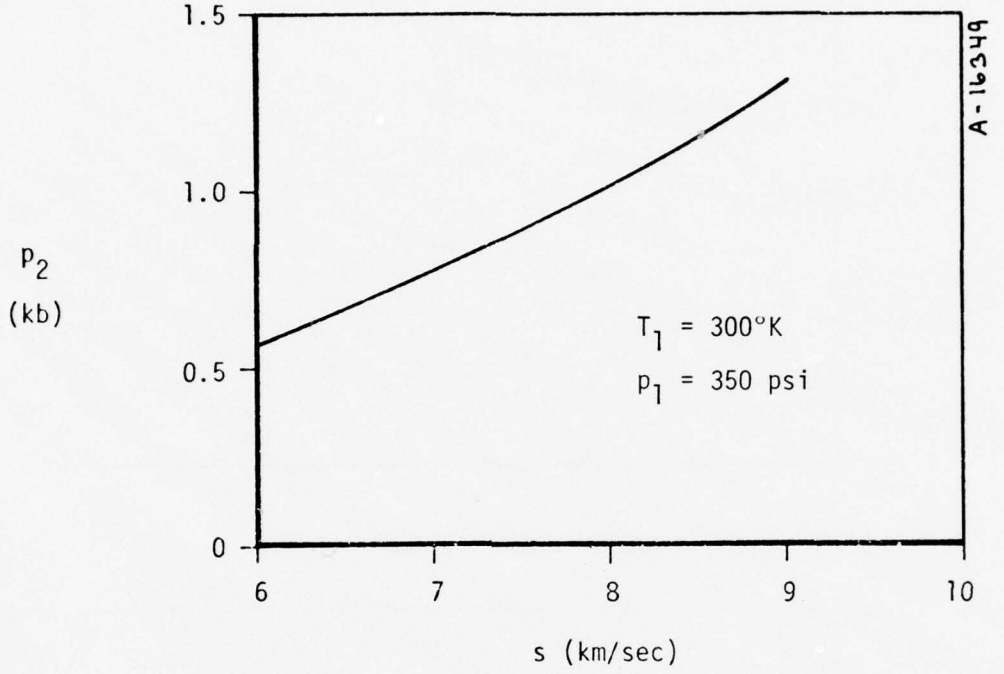

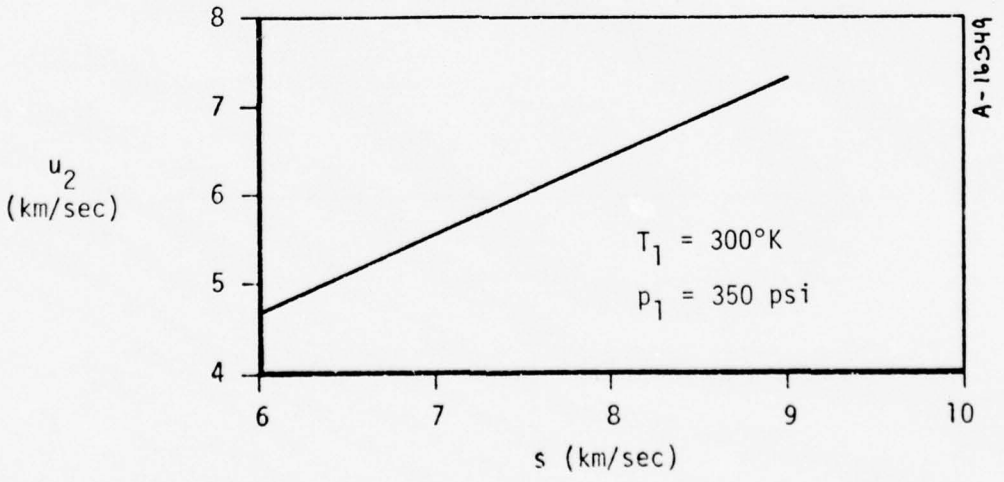

Figure 2. Pressure and particle velocity dependence on shock velocity.

When the explosive drivers are actuated, the volume of the system changes and the explosively formed "pistons" do work at constant pressure. After driver operation is complete, the system has a total energy of:

$$E_2 = E_i + p_2 \Delta V \tag{3}$$

where ΔV = change in volume for both drivers resulting from pressure tube collapse

p_2 = pressure behind the driver shock

All gas processed by the explosive drivers is now assumed to be carried by its own momentum into the compressor section and trapped there when the compressor piston just covers the injection ports.

The compressor piston, separated from the rest of the system by a diaphragm, is accelerated into a vacuum. In moving from the diaphragm position just upstream of the injection ports to the point where it just covers the injection ports, trapping the injected gas, the compressor piston does negligible work on the system. System energy is still accurately given by Equation (3).

At this point, the system is considered to be in a state shown by:

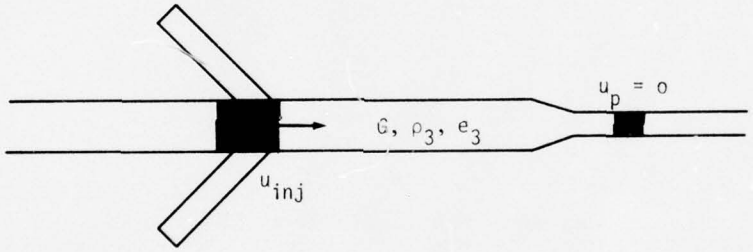

where $e_3 = \frac{E_2}{G}$

ρ_3 = density of the gas, G/V_{inj}

(V_{inj} = volume of the compressor section at injection port closure)

These two state variables are sufficient to determine all other state variables in the system using Figures A-1 through A-5 in Appendix A, or numerically using relations (A-1) to (A-7), also in Appendix A.

Compression is assumed to take place isentropically, and work is done on the system by the compressor piston as it decelerates and gives up its kinetic energy to the gas. Compression begins at piston velocities of 3,500 fps (1.1 km/sec) or less, so that the kinetic energy of the gas is always much less than its internal energy. Compression can be modeled as a series of equilibrium states.

Pressures and densities at constant entropy are determined graphically from Figures A-1 to A-5, or numerically from relations (A-1) through (A-7).

As the compressor piston decelerates, the gas density increases as the volume of the compressor section decreases. The relation between gas density and compressor section geometry is

$$\rho = \frac{G}{[V_{inj} - Ax]} \tag{4}$$

where A = cross sectional area of compressor section

x = distance measured from downstream edge of injection port

The pressures and densities at constant entropy are fitted to a power relation of the form*

$$p = \eta\rho^{\gamma} \tag{5}$$

Using (4) and (5), the deceleration of the piston is calculated by integrating the expression

$$\int_{p_3}^{p_4} pdx = (1/2)\,\frac{M_{pist}\,u_{inj}^{2}}{A} \tag{6}$$

where p_4 = pressure when compressor piston stops

p_3 = pressure after injection but before compression

M_{pist} = compressor piston mass

Performing the indicated integration to the position where the piston comes to a stop:

$$x_{ps} = \frac{V_{inj}\left[\frac{(\gamma-1)\,M_{pist}\,u_{inj}^{2}}{2\eta G^{\gamma}} + V_{inj}^{(1-\gamma)}\right]^{\frac{1}{1-\gamma}}}{A} \tag{7}$$

where ps indicates "piston stop."

This equation gives the distance from the downstream edge of the injection port to the point at which the piston stops, assuming full injection, no losses, and no projectile motion. However, in reality, complete injection never happens, losses occur, and the projectile begins to move before the compressor piston stops. As a result, the piston will stop further downstream than indicated by (7).

*This equation gives an accurate representation of pressure variation with density for calculating the deceleration of the compressor piston. This is the only place it is used in this procedure.

Once x_{ps} is determined, reservoir density, ρ_4 is determined from (4). Since compression was assumed to be isentropic, $S_4 = S_3$ (where S = entropy) and the reservoir state is completely determined from the two state variables ρ_4, S_4, and Equations (A-1) through (A-7). Alternately, the reservoir state can be determined graphically from Figures (A-1) through (A-5).

Dimensions and volumes for various configurations used by PI are given in Figure 3 and Table 2. Calculated reservoir states are given in Table 3 for several configurations and initial conditions of the PI launcher.

Since the hydrogen is partially dissociated and influenced by covolume forces and molecular vibration, the sound speeds and isentropic indices were computed numerically from relations (A-1), (A-2), and (A-5) using

$$C = \left[\frac{\Delta p}{\Delta \rho}\right]^{1/2}_{\substack{\Delta S = 0 \\ \Delta T = 1°K}}$$

$$\gamma_{isent} = \left(\frac{\rho}{p}\right)\left[\frac{\Delta p}{\Delta \rho}\right]_{\substack{\Delta S = 0 \\ \Delta T = 1°K}}$$

where C = sound speed

γ_{isent} = isentropic index

ΔS = change in entropy

Reservoir temperature, T_4, is shown in Figure 4 as a function of reservoir density, for several pressures and scaled sound speeds, C_4/γ_4. Figure 4 is used later in estimating heat loss from the reservoir.

3.3 CALCULATION OF BALLISTIC CYCLE PERFORMANCE

The calculation of projectile velocity is made by isentropically expanding the gas from the reservoir state using the preburned-propellant gun model and curves of Seigel (Reference 2). In this model, the compressor piston is assumed to have decelerated to rest permanently, prior to projectile acceleration, hence the reservoir geometry is constant. In using Seigel's preburned-propellant gun results, the reservoir is characterized by pressure, p_4; sound speed, C_4; gas mass, G; isentropic index, γ_4; and compressor to barrel diameter ratio, D_{21}. The launch tube has length L and the projectile is characterized by its mass, M_p.

Typical performance curves are shown in Figures 5 to 7. These curves were derived by computer solution of the characteristic equations for various gas to projectile mass ratios, G/M_p, and the reservoir to launch tube diameter ratio, D_{21}. The curves are displayed with the dimensionless projectile velocity $\bar{u} = u_p/C_4$ plotted against the ballistic parameter $\bar{x} = \frac{P_4 AL}{M_p C_4^2}$.

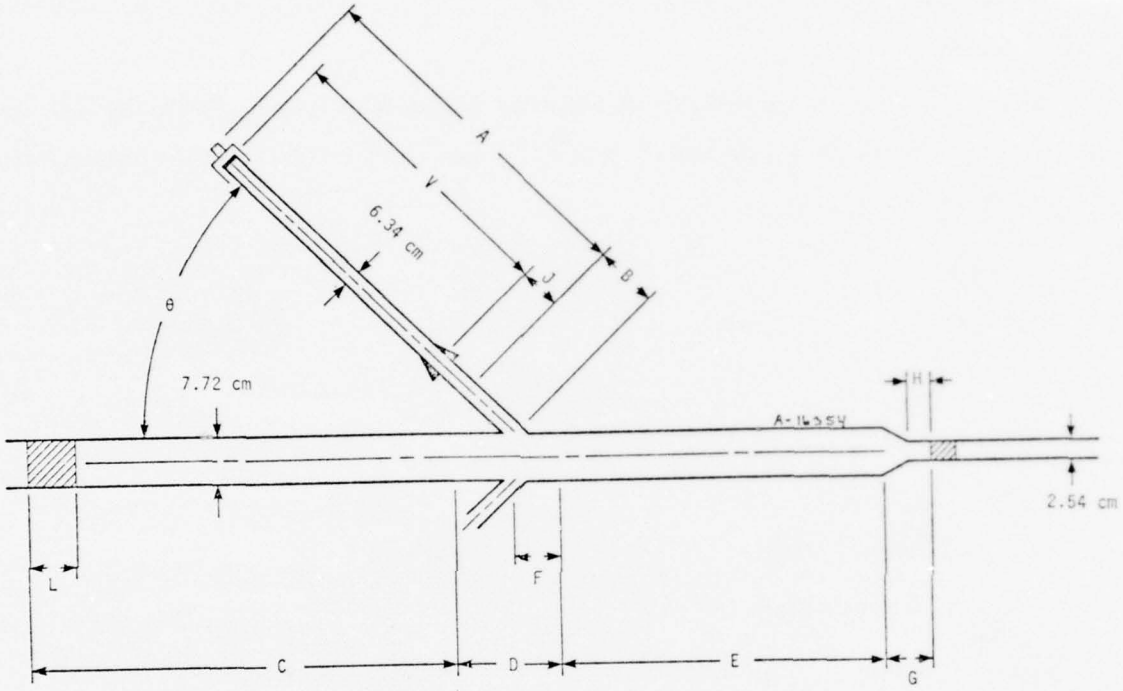

Figure 3. PI hybrid two stage launcher geometry (see Table 2).

TABLE 2. DIMENSIONS AND VOLUMES FOR PI LAUNCHER TESTS (SEE FIGURE 3)

Length (cm)	Test 1	Test 2	Test 3	Test 4	Test 5	Test 6	Test 7	Test 8
A					417.83	417.83	417.83	417.83
B					20.32	20.32	20.32	38.74
C	394.97	394.97	394.97	394.97	394.97	394.97	394.97	394.97
D	35.56	35.56	35.56	35.56	35.56	35.56	35.56	45.72
E					240.94	240.94	240.94	240.94
F	18.03	18.03	18.03	18.03	18.03	18.03	18.03	18.03
G						19.69	19.69	19.69
H						5.08	5.08	5.08
J						11.43	11.43	11.43
L	22.86	22.86	50.80	50.80	50.80	50.80	57.15	57.15
V						400.05	400.05	400.05
θ (degrees)		45°	45°	45°	45°	45°	45°	24°
Volume (cm^3)								
Driver pressure tubes to flange					25,963	25,963	25,963	12,982
Driver flange to compressor port					1,287	1,287	1,287	1,227
Compressor between diaphragm and projectile					13,304	13,304	13,304	13,780
Compressor after port closure					12,352	12,352	12,352	11,710
ΔV due to driver operation					25,242	25,242	25,242	12,621

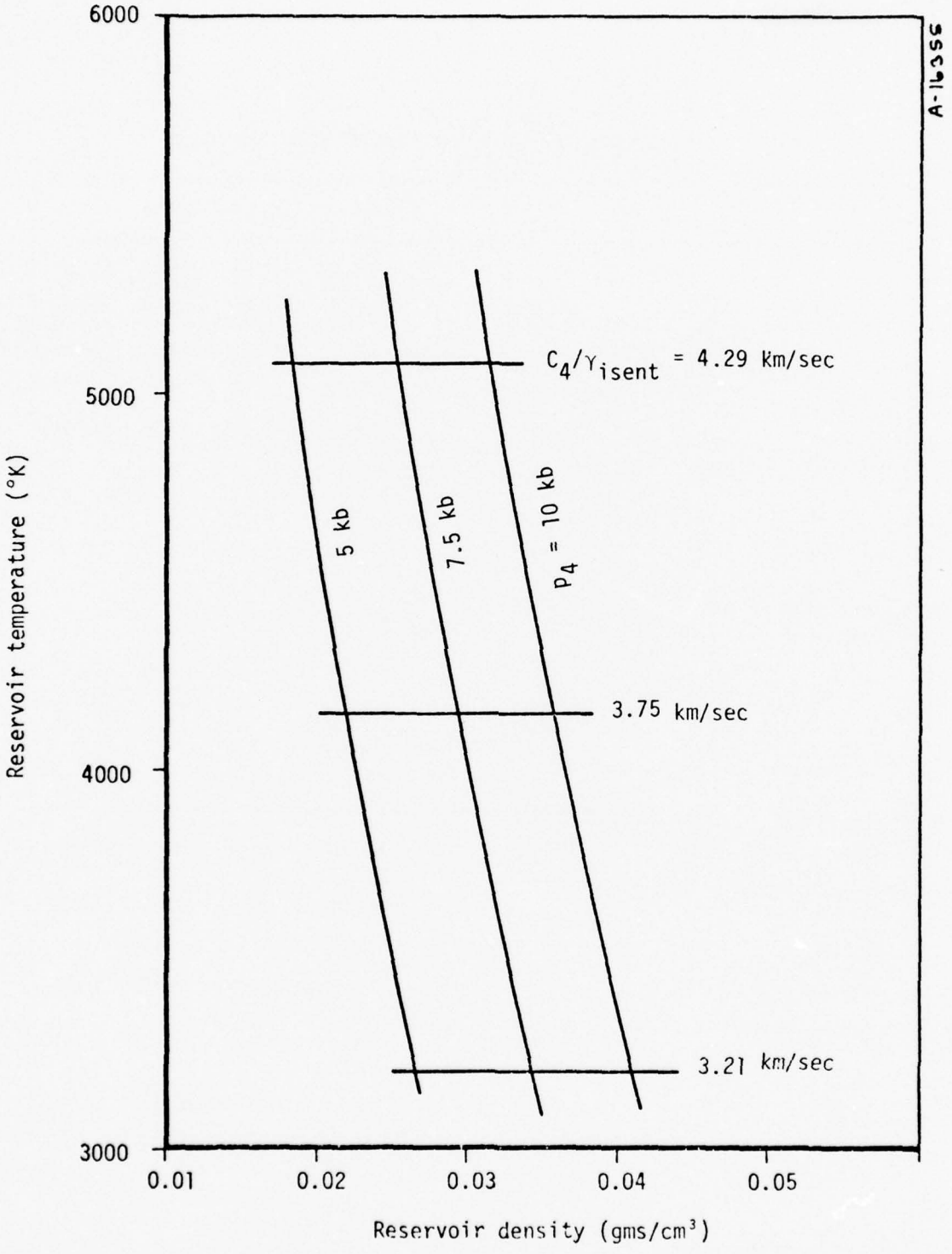

Figure 4. Loci of possible reservoir states.

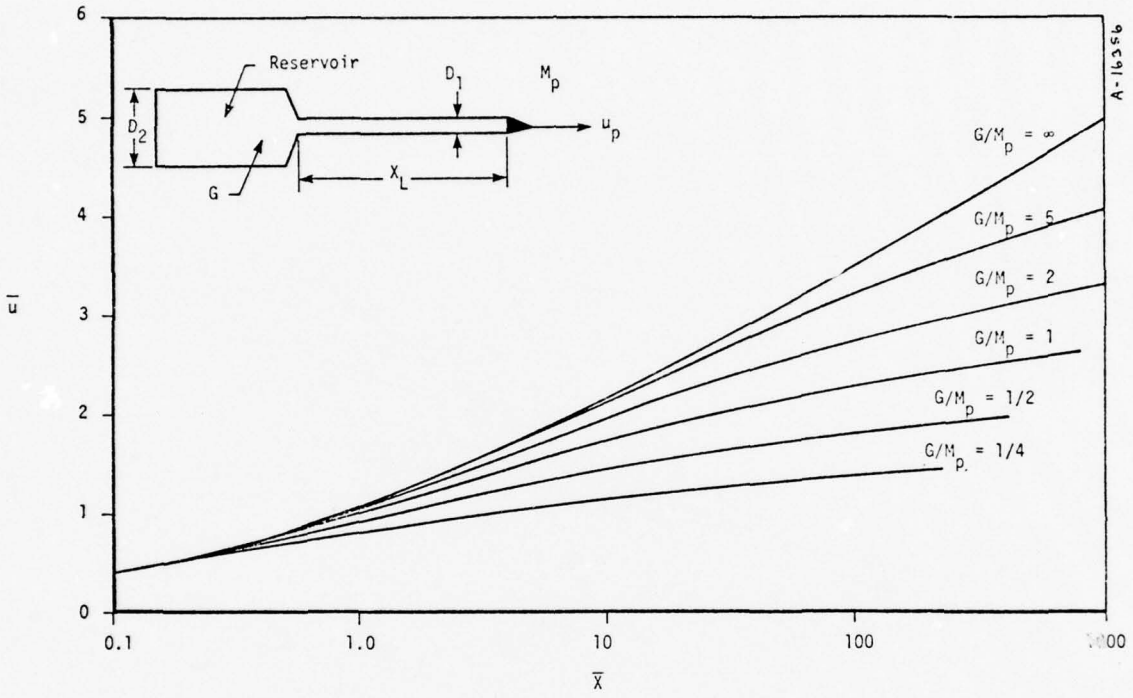

Figure 5. Launcher performance with $D_{21} = 2$ and $\gamma_{isent} = 1.1$ (Reference 2).

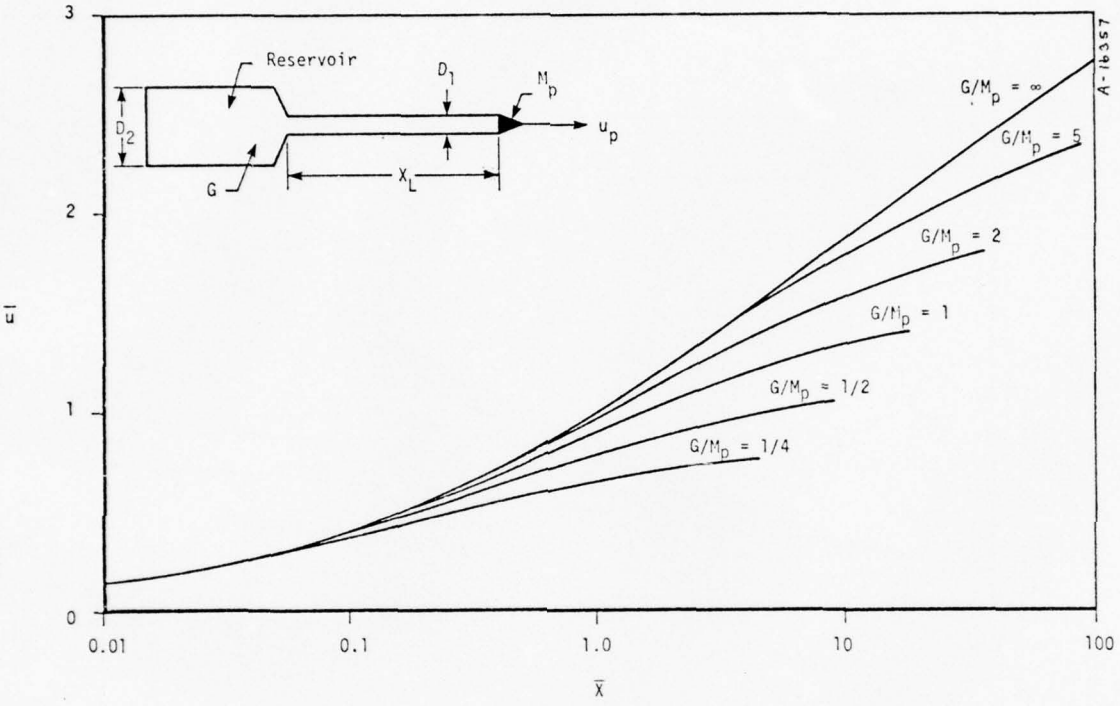

Figure 6. Launcher performance with $D_{21} = 2$ and $\gamma_{isent} = 1.4$ (Reference 2).

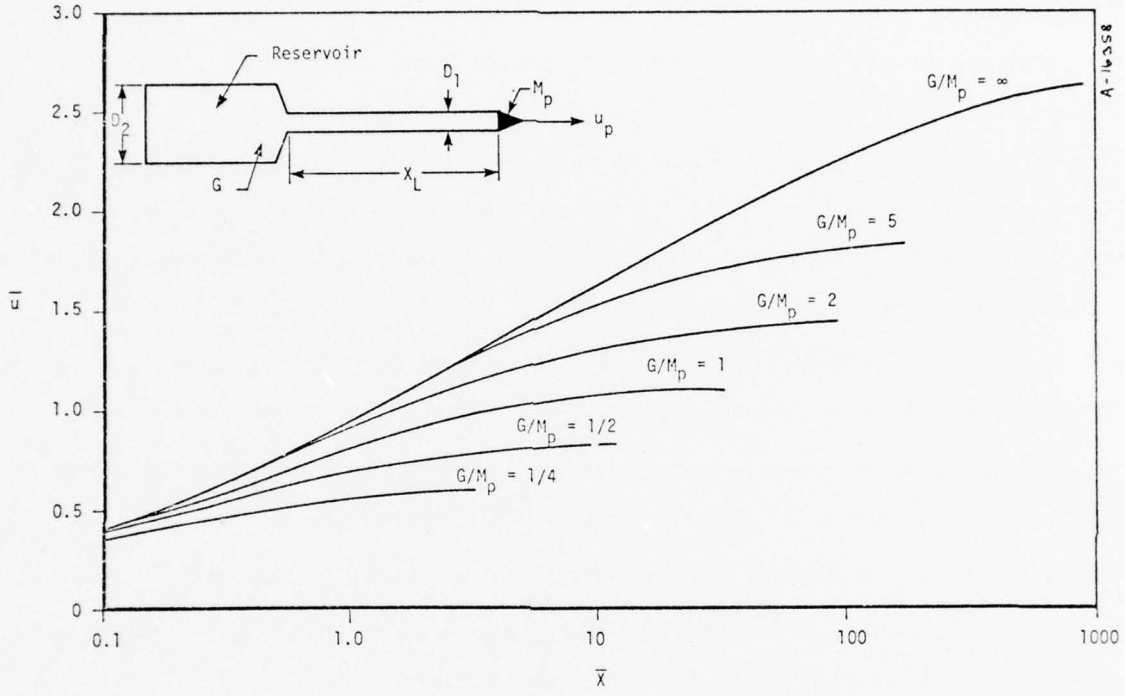

Figure 7. Launcher performance with $D_{21} = 2$ and $\gamma_{isent} = 1.667$ (Reference 2).

These curves are available for γ_{isent} = 1.1, 1.4, and 1.67. In the range of conditions in which the PI launcher operates, the reservoir gas is vibrationally excited, partially dissociated, and is in a density range where covolume forces are significant. These reservoir conditions must be converted into equivalent conditions compatible with Siegel's curves.

Glass (Reference 3) has shown that muzzle velocities are nearly invariant for reservoir gases of the same scaled sound speed, C_4/γ_4 where the condition $u_p < 2\ C_4/\gamma_4$ is satisfied. For conditions typical of the PI launcher, this condition is always met.

Thus, for a reservoir with a calculated C_4 and γ_4, an equivalent reservoir with C_4' and γ_4' = 1.1, 1.4, or 1.67 can be specified where $C_4/\gamma_4 = C_4'/\gamma'_4$.

The Seigel curves assume γ_4' is constant throughout the projectile acceleration. When covolume forces are not present, this assumption is valid over the range of operating conditions characteristic of the PI launcher (Reference 4). When covolume forces are important, this assumption leads to slightly lower calculated muzzle velocities.

Based on the calculation procedure illustrated in Appendix B, performance estimates for the initial conditions of Table 3 are presented in Table 4. Some conclusions are worth noting:

- Evacuating the compressor section results in a smaller G/M_p but a higher reservoir specific energy. Projectile velocity is only slightly higher.
- Substantial performance increases result if piston energy is increased
- Optimum performance is achieved if the compressor section is evacuated, piston energy is maximized, and if the G/M_p ratio is greater than 1

The upper limit on muzzle velocity for the present configuration of the PI launcher can be estimated by this method. As noted previously, this estimate assumes ideal driver operation, full injection, and no loss mechanisms. To estimate the upper limit, the following initial conditions are used:

- Initial driver pressure is doubled to 700 psia to increase the G/M_p ratio
- The compressor chamber is evacuated to maximize reservoir specific energy
- The 75 mm gun is operated at its performance limit to maximize compressor piston energy

The state variables and conditions which are achieved through these modifications are presented in Tables 3 and 4 (Table Index T8). The calculated muzzle velocity for the 86 gram projectile

TABLE 3. CALCULATED[a] DRIVER, COMPRESSOR, AND RESERVOIR STATES FOR SEVERAL DRIVER/COMPRESSOR CONDITIONS

Driver		Compressor				Reservoir						
Initial Pressure (psi)	Shock Pressure (kilobars)	Piston Mass (gms)	Piston Velocity (km/sec)	Initial Pressure (psi)	Max piston stop from transition (cm)	P_4 (kilobars)	T_4 (°K)	ρ_4 (gm/cm^3)	α_4 (%)	γ_{isent}	C_4 (km/sec)	Table Index
350 Test 7	0.974	2724	0.91	350	101.35	2.98	3715	0.0159	1.0	1.52	5.34	T1
350 Test 7, covolume suppressed	0.953	2724	0.91	350	84.58	2.89	3715	0.0187	.0	1.26	4.43	T2
350	0.974	2724	0.91	3.7	81.79	2.94	4785	0.0124	5.5	1.40	5.75	T3
350	0.974	3450	0.91	3.7	63.25	4.07	5050	0.0156	5.0	1.43	6.12	T4
350 Test 8 1 driver	0.974	2724	0.91	350	52.32	3.88	3613	0.0201	1.0	1.64	5.66	T5
700	1.99	4540	0.91	350	118.36	5.20	4155	0.0226	1.8	1.66	6.18	T6
700	1.99	4540	0.91	3.7	105.92	5.05	4803	0.0196	4.5	1.52	6.29	T7
700	1.99	4540	1.07	3.7	81.03	7.40	5120	0.0250	5.5	1.61	6.95	T8
700	1.99	4540	0.76	3.7	134.87	3.61	4534	0.0156	3.5	1.45	5.80	T9
700	1.99	4540	1.22	3.7	64.01	10.47	5425	0.0308	6.5	1.71	7.63	T10

[a]Calculation procedure is described in Appendix B.

TABLE 4. CALCULATED[a] LAUNCHER PERFORMANCE[b] FOR SEVERAL DRIVER/COMPRESSOR CONDITIONS (RESERVOIR CONDITIONS OF TABLE 3)

Driver		Compressor		Reservoir		Launch Cycle			
Initial Pressure (psi)	Piston Mass (gms)	Piston Velocity (km/sec)	Initial Pressure (psi)	p_4 (Kilobars)	C_4/γ_4 (km/sec)	M_p (gms)	G/M_p	u_p (km/sec)	Table Index
350	2724	0.91	350	2.98	3.51	86	0.96	3.70	T1
Like Test 7[c]									
350	2724	0.91	350	2.89	3.52	86	0.96	3.67	T2
Covolume suppressed									
350	2724	0.91	3.7	2.94	4.11	86	0.62	3.80	T3
350	3450	0.91	3.7	4.07	4.28	86	0.62	4.28	T4
350	2724	0.91	350	3.88	3.45	87.4	0.64	3.74	T5
Like Test 8[c]									
700	4540	0.91	350	5.20	3.72	86	1.57	4.65	T6
700	4540	0.91	3.7	5.05	4.14	86	1.23	4.81	T7
700	4540	1.07	3.7	7.40	4.32	86	1.23	5.39	T8
700	4540	0.76	3.7	3.61	4.00	86	1.23	4.28	T9
700	4540	1.22	3.7	10.47	4.46	86	1.23	6.12	T10

[a] Calculation procedure is described in Appendix B

[b] For L/D = 300

[c] Experimental velocities were about 70 percent of these ideal results

is 5.39 km/sec. Thus in the present configuration (75 mm gun, 2 drivers), the upper performance limit under ideal conditions appears to be about 5.5 km/sec (18,000 fps).

Reconfiguration of the system, such as addition of another driver and use of a larger first stage, is necessary to increase the performance limit to the design goal of 6.1 km/sec. In fact, the performance limit calculated under the above idealized conditions should be somewhat greater than 6.1 km/sec to provide some margin for loss mechanisms such as incomplete gas injection, reservoir heat loss, and boundary layer effects.

3.4 SENSITIVITY OF MUZZLE VELOCITY TO RESERVOIR AND LAUNCHER PARAMETERS

The sensitivity of muzzle velocity to the following parameters has been evaluated:

- Barrel length to diameter ratio, L/D
- Hydrogen gas to projectile mass ratio, G/M_p
- Compressor piston energy
- Reservoir pressure, p_4 and scaled sound speed C_4/γ_{isent}

Figures 8 and 9 show the variation of muzzle velocity with barrel L/D for conditions typical of the PI tests. As will be discussed in Section 4, projectile velocity is not expected to increase significantly beyond a barrel L/D of about 300 because of boundary layer effects. The performance predicted by PI, however, depends on the velocity calculated for a barrel L/D of 576. For conditions representative of the PI tests, the last half of the barrel would contribute an additional 15 to 20 percent to projectile velocity, if boundary layer effects did not exist. It is therefore important in future work to use barrel lengths no greater than about 300 L/D's in preliminary performance estimates.* In assessing the sensitivity of muzzle velocity to varying G/M_p, p_4, and C_4/γ_4, the barrel length is henceforth considered fixed at 300 L/D's.

Figures 10 and 11 cover the range of p_4 and C_4/γ_4 of the PI tests; they show that muzzle velocity is quite sensitive to the G/M_p ratio for the range of design G/M_p values in the PI tests ($0.62 \leq G/M_p \leq 0.92$ without any losses). From these results it can be concluded that any loss of driver gas during driver operation, injection, compression, or initial projectile acceleration in the PI tests would seriously degrade anticipated performance. A G/M_p ratio of 1.5 to 2.0 would seem to be a good design goal since small gas losses could be incurred without seriously degrading performance.

---

*However, no performance penalty should result from experimenting with a large L/D launcher to derive experimental data on the benefits of incremental lengths. Similarly, larger L/D's could be considered when boundary layer effects are adequately accounted for in the evaluation procedure.

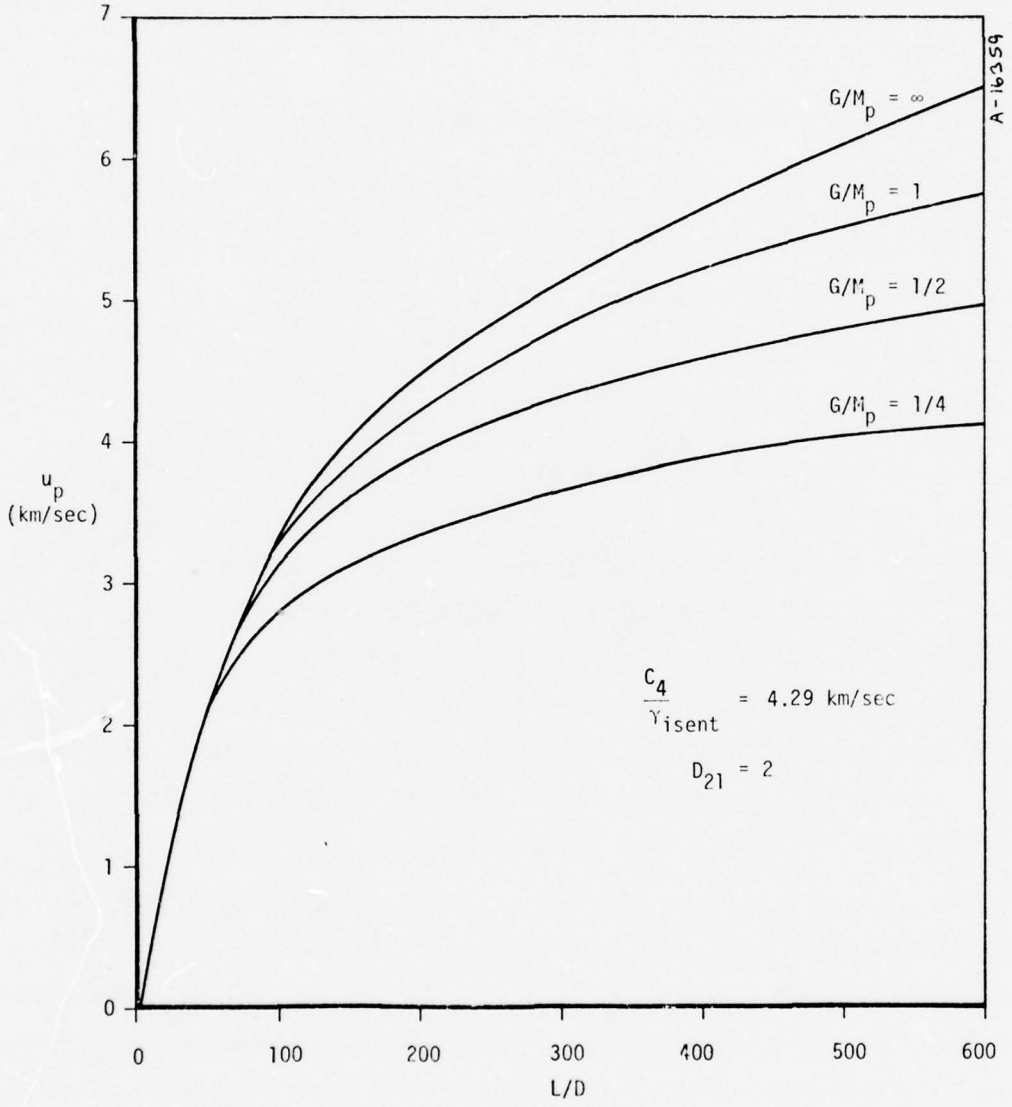

Figure 8. Performance sensitivity to barrel dimensions for various ratios of gas mass to projectile mass, p_4 = 5 kb.

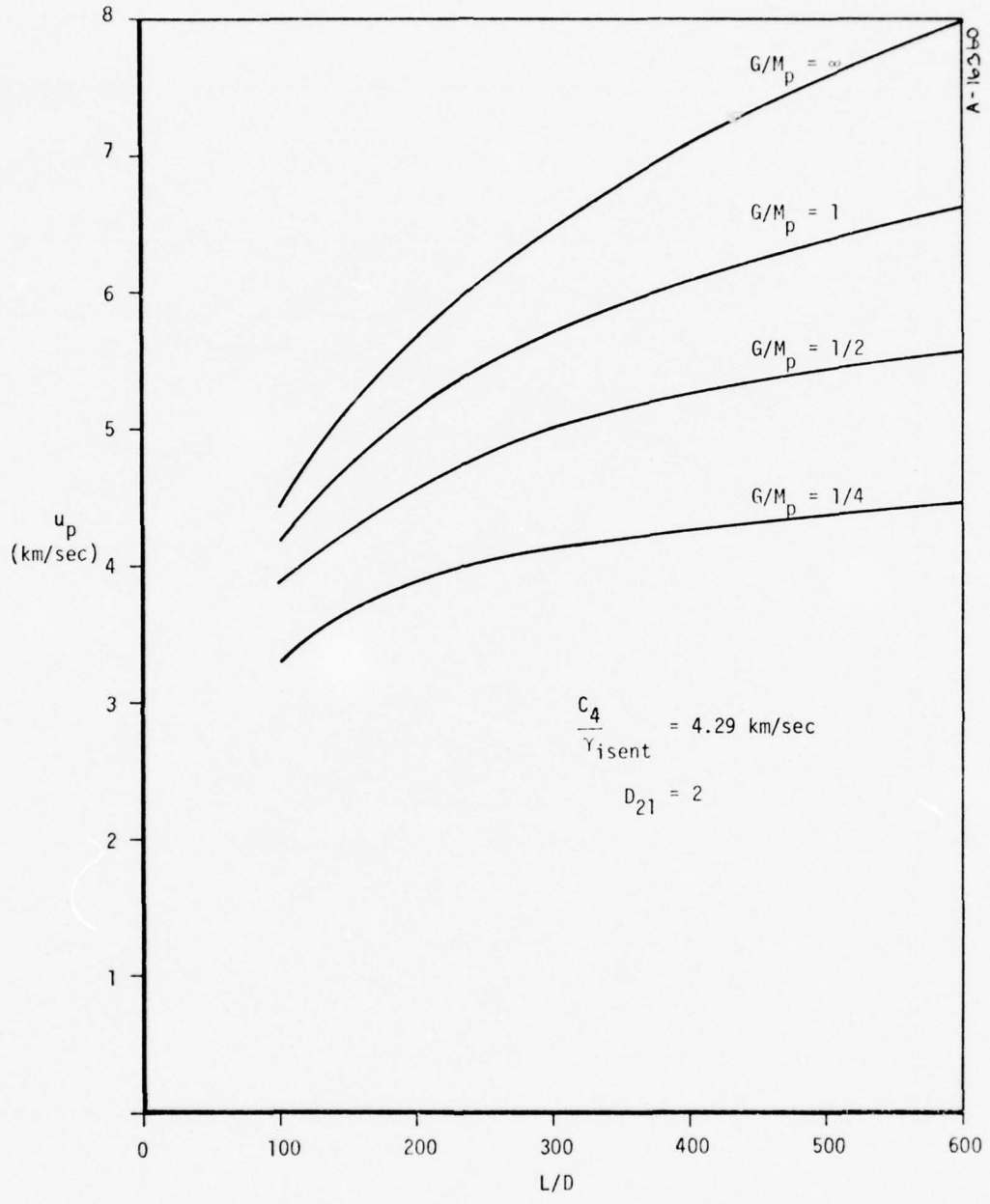

Figure 9. Performance sensitivity to barrel dimensions for various ratios of gas mass to projectile mass, p_4 = 10 kb.

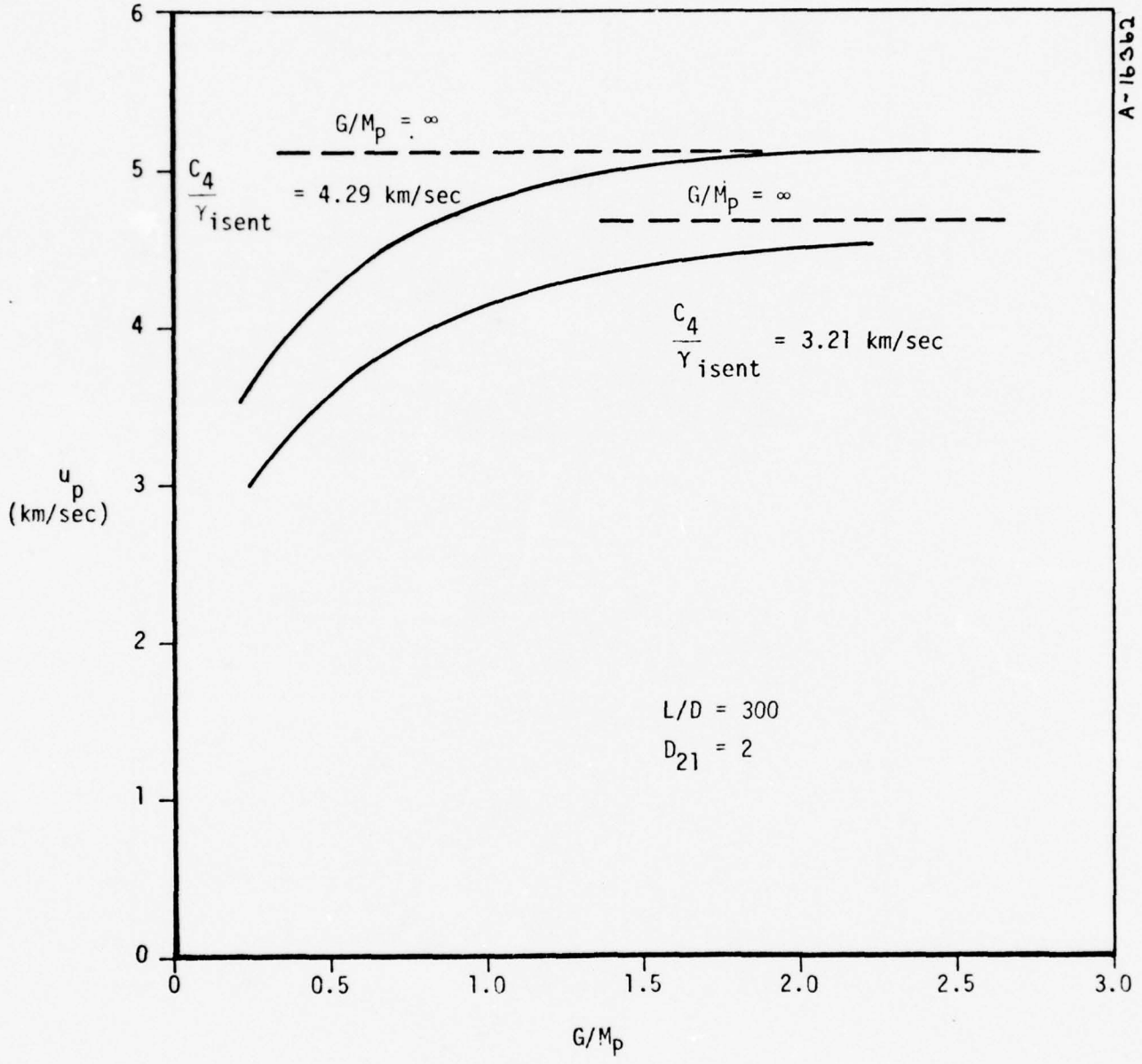

Figure 10. Performance sensitivity to ratio of gas mass to projectile mass for representative scaled reservoir sound speeds, p_4 = 5 kb.

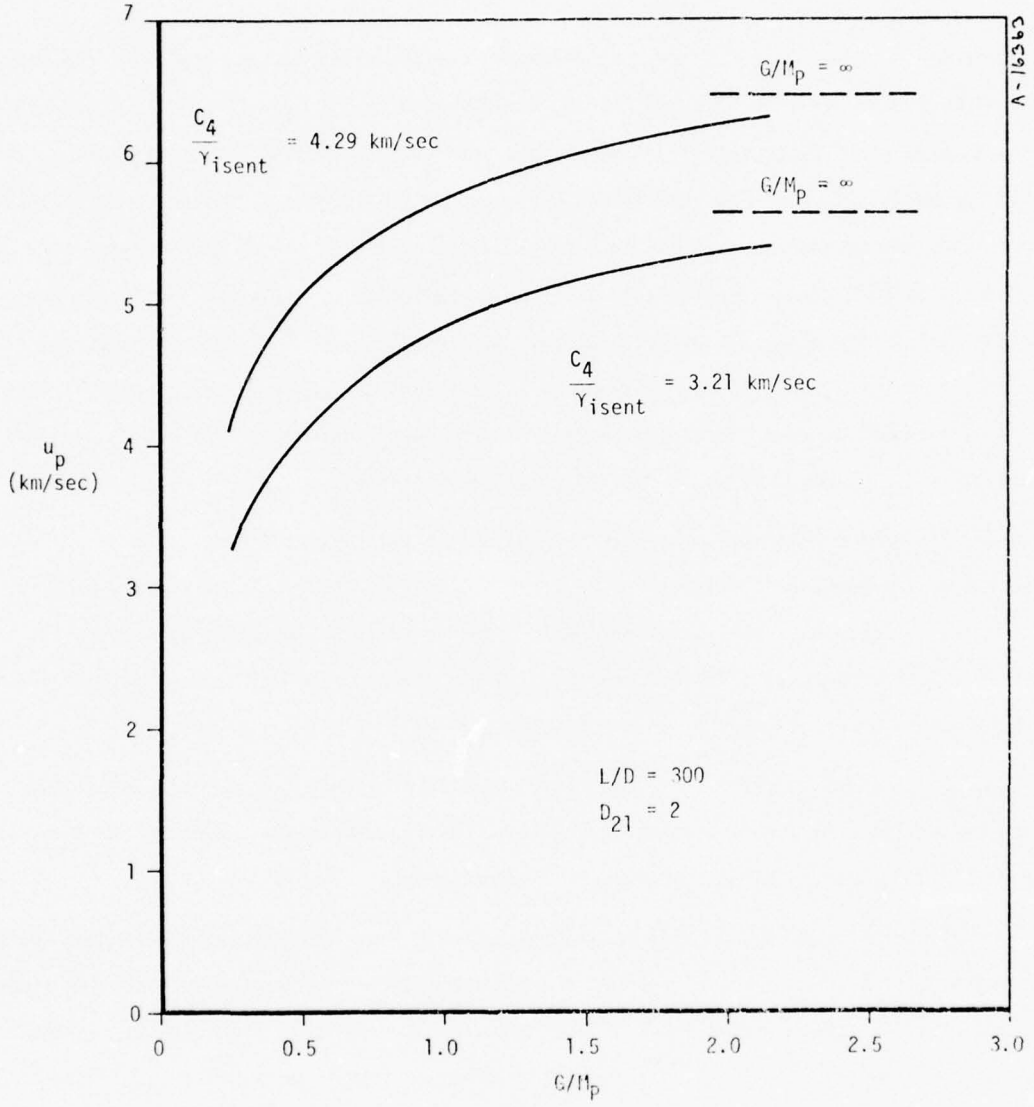

Figure 11. Performance sensitivity to ratio of gas mass to projectile mass for representative scaled reservoir sound speeds, p_4 = 10 kb.

Further increases in the G/M_p ratio would not lead to substantially better performance, but would provide a larger margin against the inevitable gas losses.

Another important design goal would be to maximize the compressor piston energy, since piston energy has a strong effect on muzzle velocity. (For example, piston energy controls final reservoir density and adds substantial energy to the reservoir.) Figure 12 shows that under typical operating conditions, a 40-percent increase in piston velocity results in a 26-percent increase in muzzle velocity.

The method used herein is accurate for estimating muzzle velocities and assessing the sensitivity of performance to variations in G/M_p ratio, scaled sound speed, C_4/γ_4, etc. In these calculations, it is assumed that the projectile is restrained until the compressor piston has come to rest. Actually, the projectile is well into the launch cycle before the compressor piston comes to rest, so that peak reservoir pressures and sound speeds are considerably lower than those calculated. The calculated pressure levels shown in Figure 13 are thus unrealistically high, but the figure does illustrate the sensitivity of muzzle velocity to peak pressure. If the G/M_p ratio is adequate (i.e., $G/M_p > 1$), the failure to develop full design pressures will not seriously affect muzzle velocity, provided that the scaled sound speed remains high. At G/M_p levels much less than 1.0, as in some of the PI experiments, performance is quite sensitive to reservoir pressure levels.

Figures 14 and 15 illustrate the sensitivity of muzzle velocity to scaled sound speed, C_4/γ_4 in the reservoir. The combination of high sound speed, C_4 and low isentropic index, γ_4, leads to the highest muzzle velocities. The scaled reservoir sound speed is an important parameter. It can be substantially lowered by heat transfer losses during the launch cycle and lowered further if heat transfer is severe enough to trigger erosion and ablation.

In a gas where covolume effects are important, both sound speed, C_4, and isentropic index, γ_4, increase rapidly with further increases in density. However, the scaled sound speed, C_4/γ_4 increases gradually and closely follows the rise in internal energy, e_4.

In summary, these studies show that projectile velocity increases with barrel length, gas-to-mass ratio, compressor piston velocity, reservoir pressure, and scaled speed of sound in the reservoir. The L/D effect is small beyond 300 even when boundary layer effects are ignored. On the other hand, performance is quite sensitive to gas-to-mass ratio below unity, which was typical of the PI experiments.

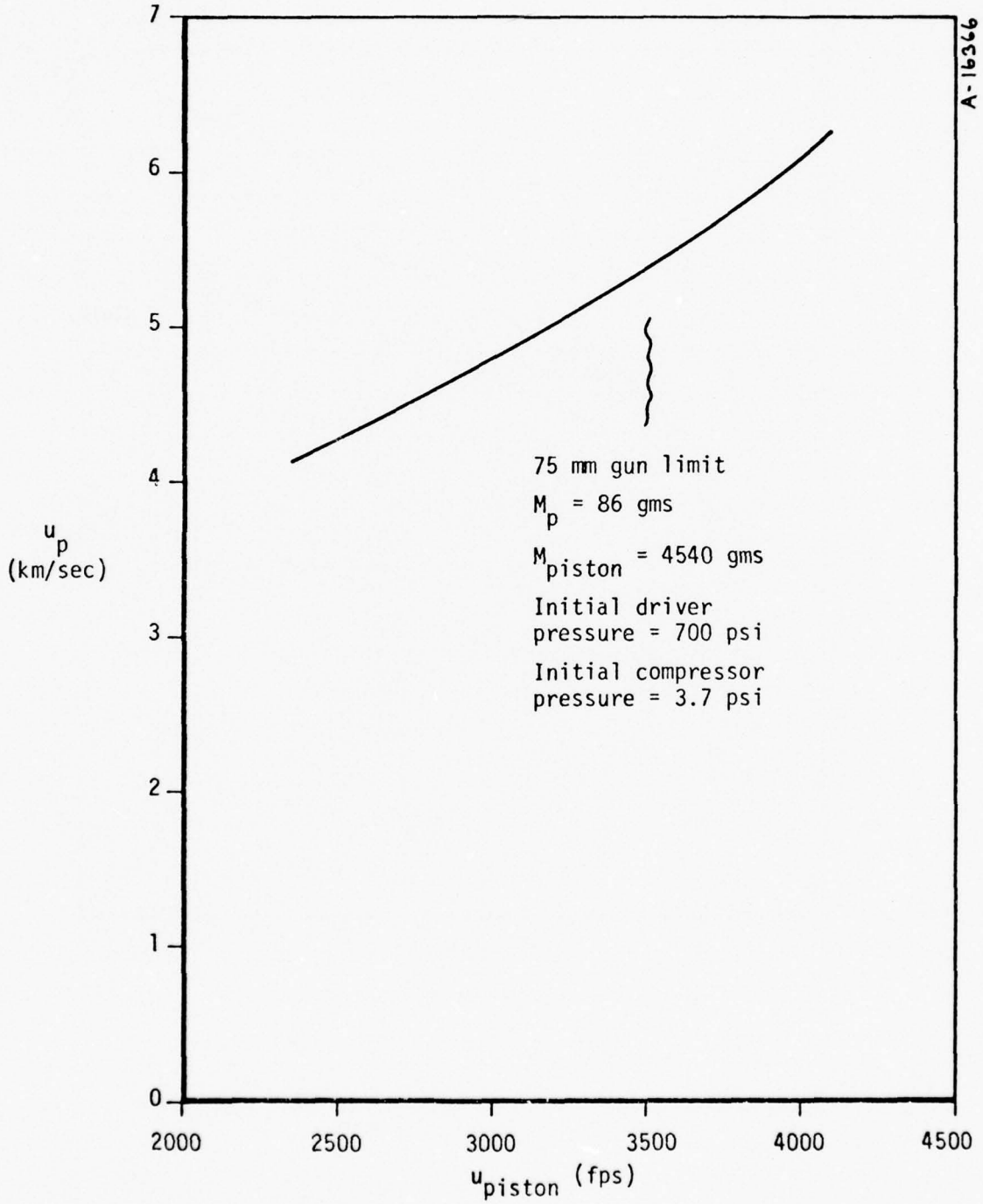

Figure 12. Performance sensitivity to maximum piston velocity.

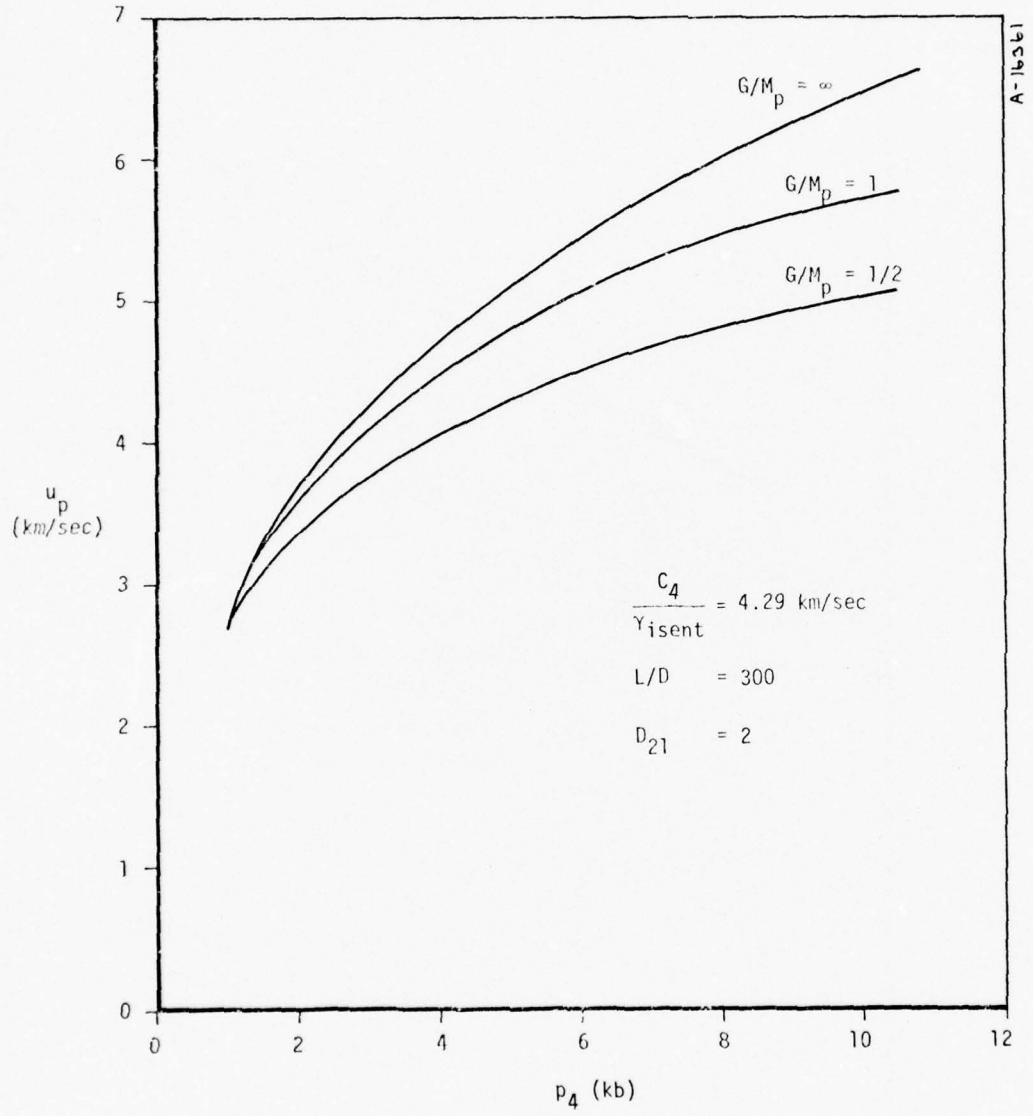

Figure 13. Performance sensitivity to reservoir pressure for various ratios of gas mass to projectile mass.

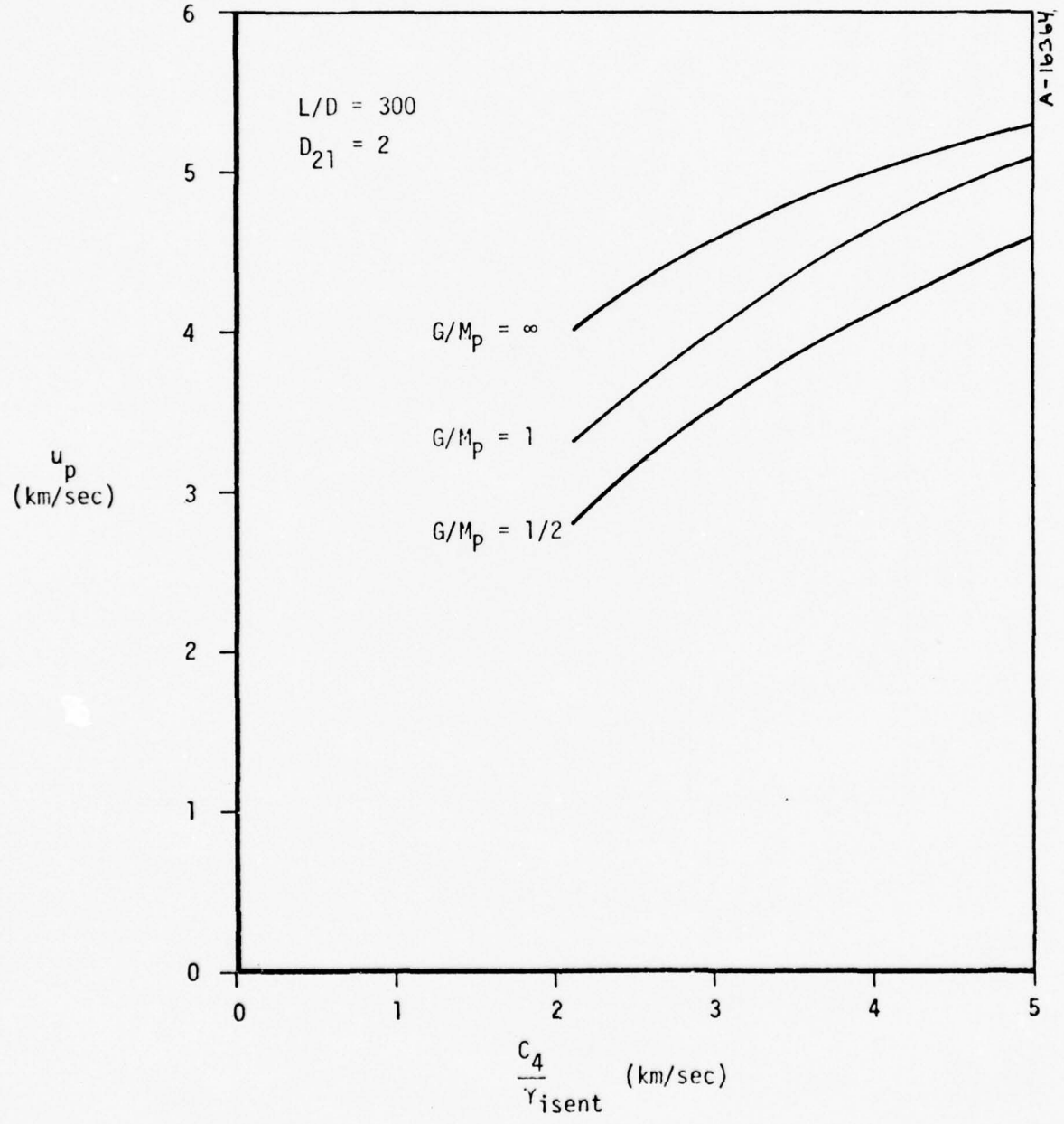

Figure 14. Performance sensitivity to scaled reservoir sound speed for various ratios of gas mass to projectile mass, p_4 = 5 kb.

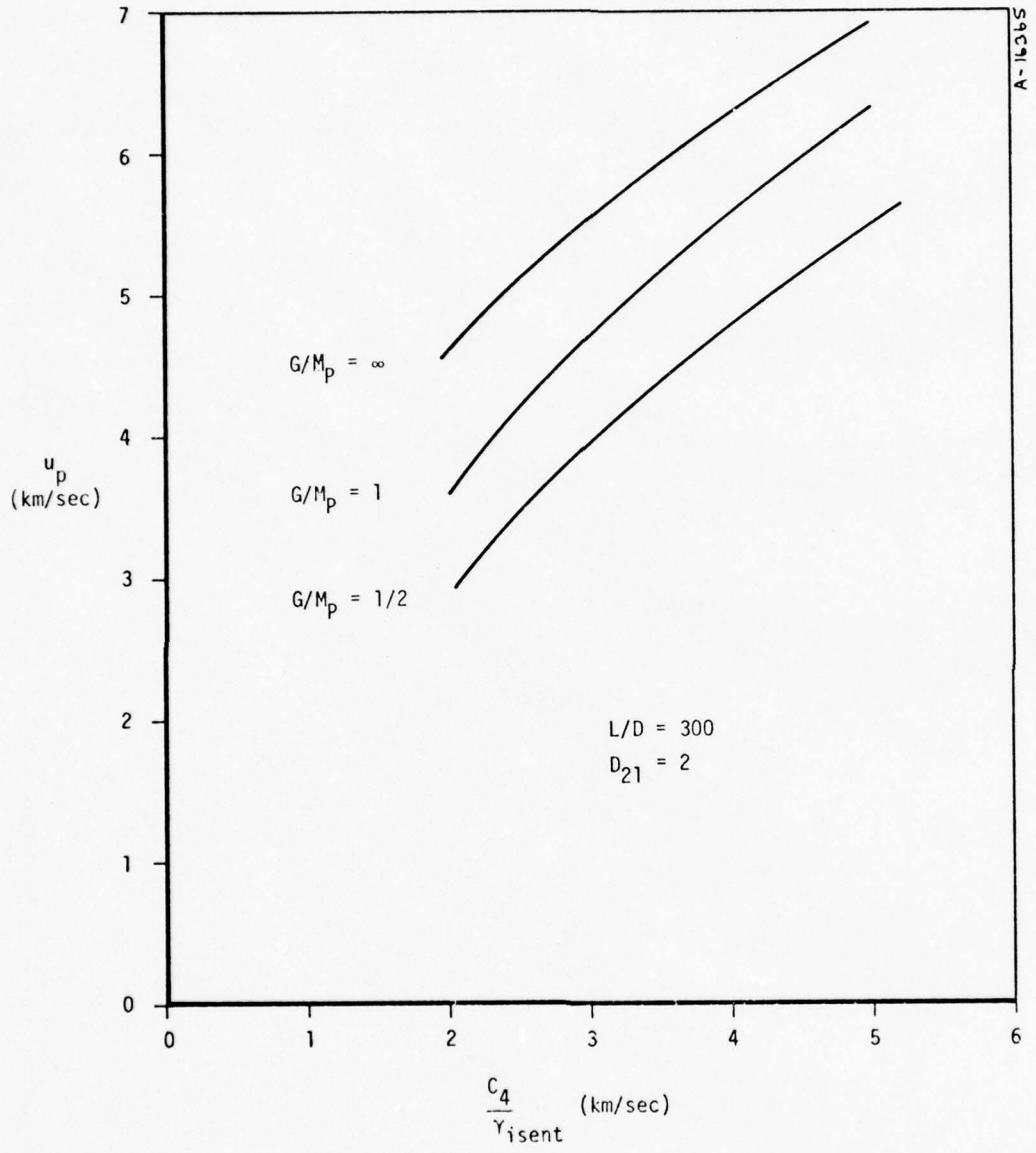

Figure 15. Performance sensitivity to scaled reservoir sound speed for various ratios of gas mass to projectile mass, p_4 = 10 kb.

Substantial gains in performance can be expected by utilizing the maximum capability of the 75 mm gun to benefit from increased peak chamber pressure and scaled speed of sound. However, the capability of the 75 mm gun is marginal in terms of achieving the desired 6.1 km/sec muzzle velocity for an 86 gm projectile in a 2.54-cm (1-inch) diameter launch tube.

SECTION 4

FACTORS DEGRADING PERFORMANCE

This section will deal with the difficulties in obtaining the desired chamber conditions in the launcher, based on the driver and injection processes. Losses accrued during the ballistic cycle after completion of injection will also be evaluated.

4.1 GAS CONDITIONS GENERATED BY THE EXPLOSIVE DRIVERS

In the ideal mode of explosive driver operation shown in Figure 16 (no jetting, no gas loss, no radial expansion), the particle velocity behind the shock is equal to the explosive driver detonation velocity. The shocked gas density and pressure remain constant behind the shock.

In practice, this mode of operation can be maintained up to approximately 10 pressure tube diameters of shocked gas. Thereafter, the momentum of boundary layer gases is sufficient to prevent complete collapse of the pressure tube. The system then begins to lose driver gas, with an accompanying decrease in shock velocity after a suitable communication time.

During ideal operation, the volume of shocked gas compressed by the shock wave is equal to the total volume processed by the shock, divided by the compression ratio across the shock. Also, to properly determine the position of the shock relative to the detonation wave, the volume of the collapse cone must be included. This is true because with a typical collapse half-angle of 9°, the volume of the collapse cone is about 10 percent of the total volume for the maximum length of shocked gas in ideal drivers.

It can be shown that the distance between the shock and the detonation wave, should be

$$\Delta x = \frac{x_s}{\rho_{21}} - \frac{D_t}{6 \tan \sigma} \tag{8}$$

where x_s = distance shock has travelled in unshocked gas

ρ_{21} = compression ratio

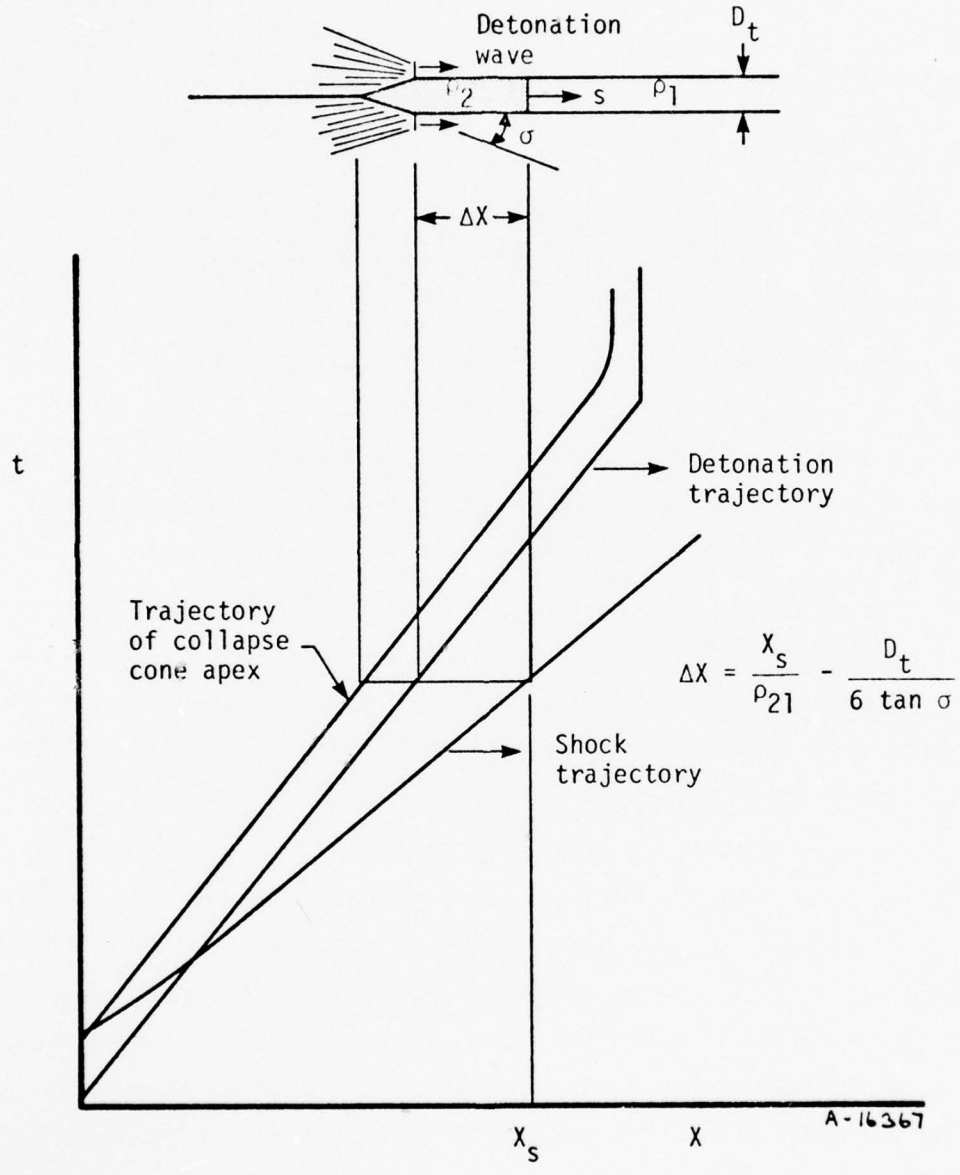

Figure 16. Ideal explosive driver operation.

D_t = pressure tube inside diameter

σ = collapse half-angle

A driver will jet when the collapse process is overdriven. Under these conditions, the maximum amount of jet material possible is determined from the classical jetting formula (Reference 5):

$$\frac{m_j}{m_\ell} = \frac{1 - \cos \sigma}{2} \tag{9}$$

where m_j = mass of jet

m_ℓ = mass of liner or pressure tube

In practice, however, the maximum jet mass is never realized since driver gas pressure, irreversible plastic working of the liner during collapse, and liner compressibility effects all tend to suppress jetting.

For a nitromethane driver (detonation velocity D = 6.25 km/sec) operating in its ideal range, the calculated shock velocity is 7.8 km/sec. The calculated compression ratio across the shock is 5.03 for hydrogen initially at 300°K and 350 psia. Examination of the PI data for the drivers used in Tests 5 to 8 (Figures 17 to 20) shows abnormally high shock velocities ranging from 8.6 to 9.0 km/sec, characteristic of severely jetting drivers.

In Test 7 for example, the observed shock velocity is 8.7 km/sec and the distance between the shock and detonation wave (Figure 19) leads to an apparent compression ratio of 3.48 (Equation (8) for σ = 9°), if shocked gas conditions are assumed uniform. For a shock velocity of 8.7 km/sec, however, a compression ratio of 5.2 is calculated (Figure 1). Therefore, shocked gas conditions for this driver must be very nonuniform.

The observed shock velocities are constant over the length of the drivers and are reproducible from driver to driver. The most likely explanation of this type of reproducible nonideal performance is that the collapsing pressure tube is overdriven and jets a spray of metal particles into the driver gas. At the pressures and temperatures involved, the jet particles would be solid or liquid and their volume would be negligible. However, the particles are jetted into the driver gas at about twice detonation velocity (i.e., about 12.5 km/sec) in laboratory coordinates. As these particles are decelerated by the shocked gas, they transfer momentum to the gas and thereby can support pressure and density gradients.

If it is assumed that this expanding cloud of steel particles "snowplows" and forms an impermeable piston, then this particle piston would have to support a pressure differential of 1.2 kb

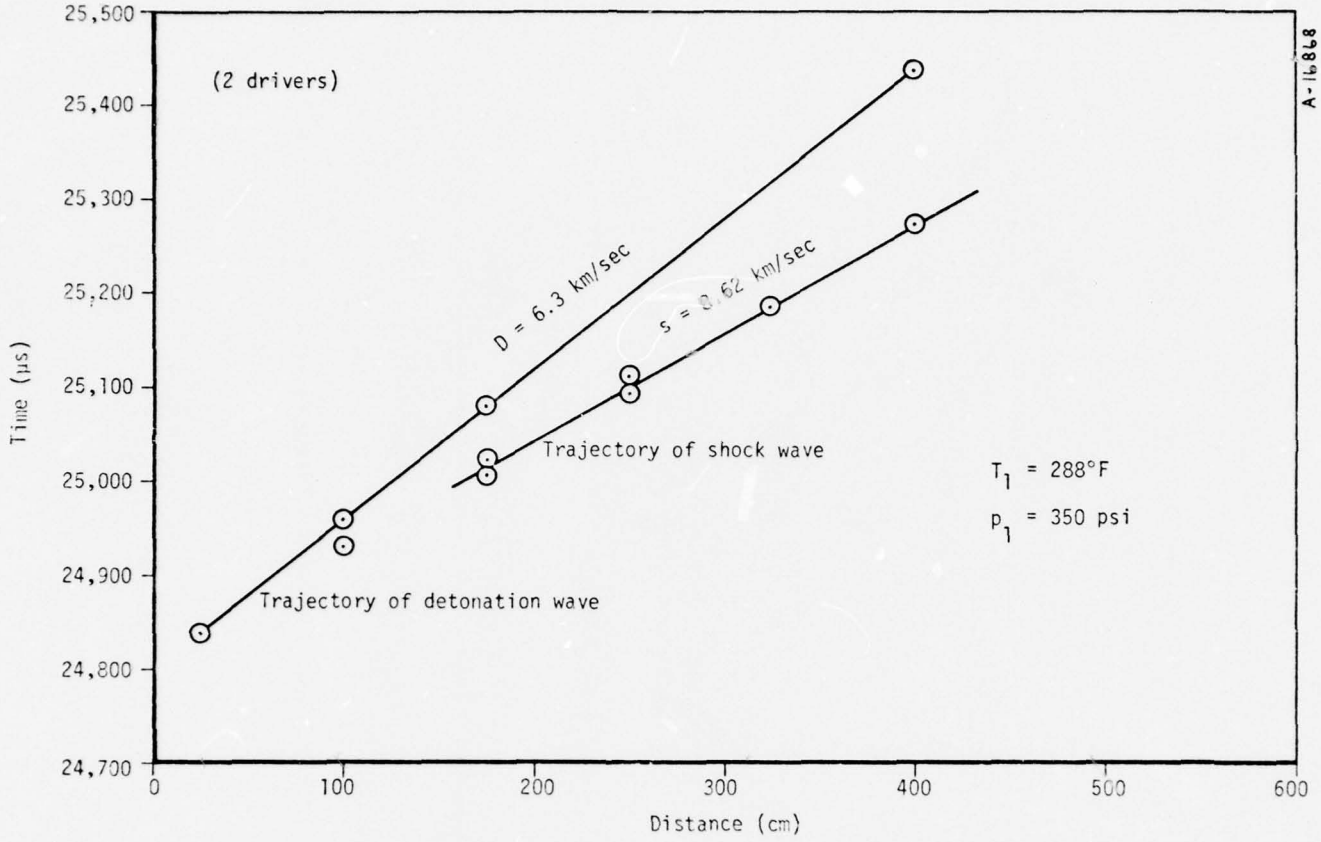

Figure 17. Explosive driver performance for PI, Test Number 5.

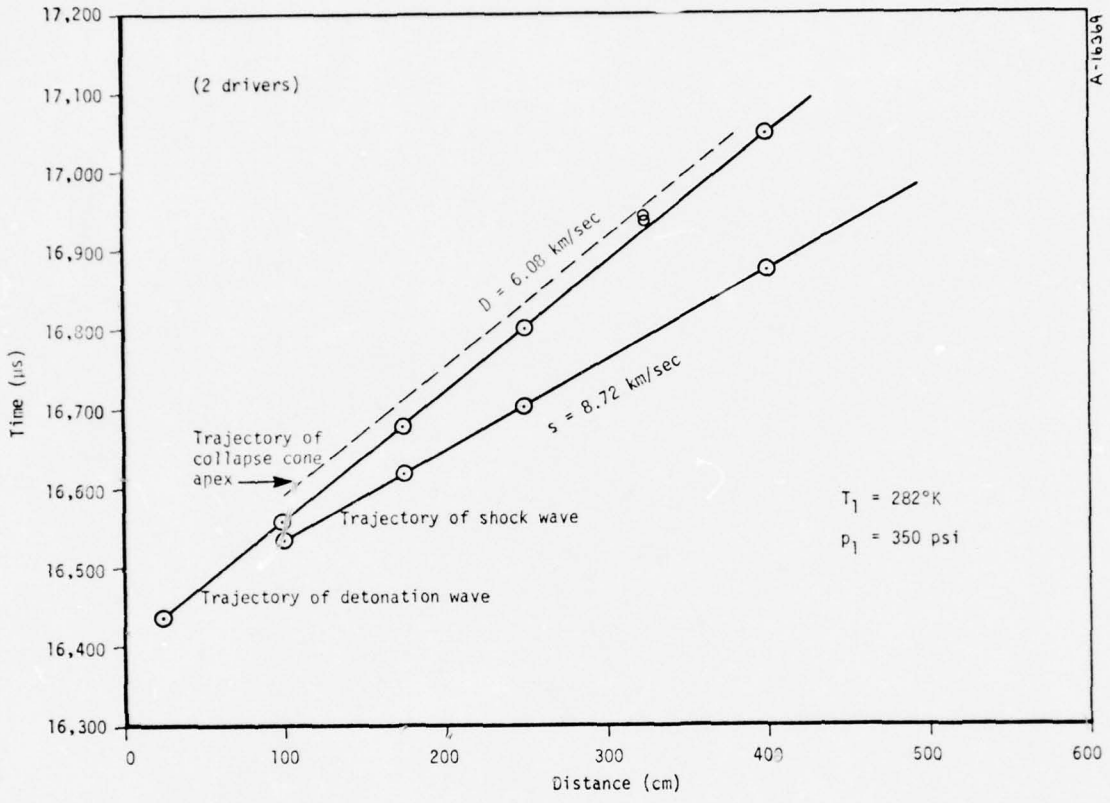

Figure 18. Explosive driver performance for PI, Test Number 6.

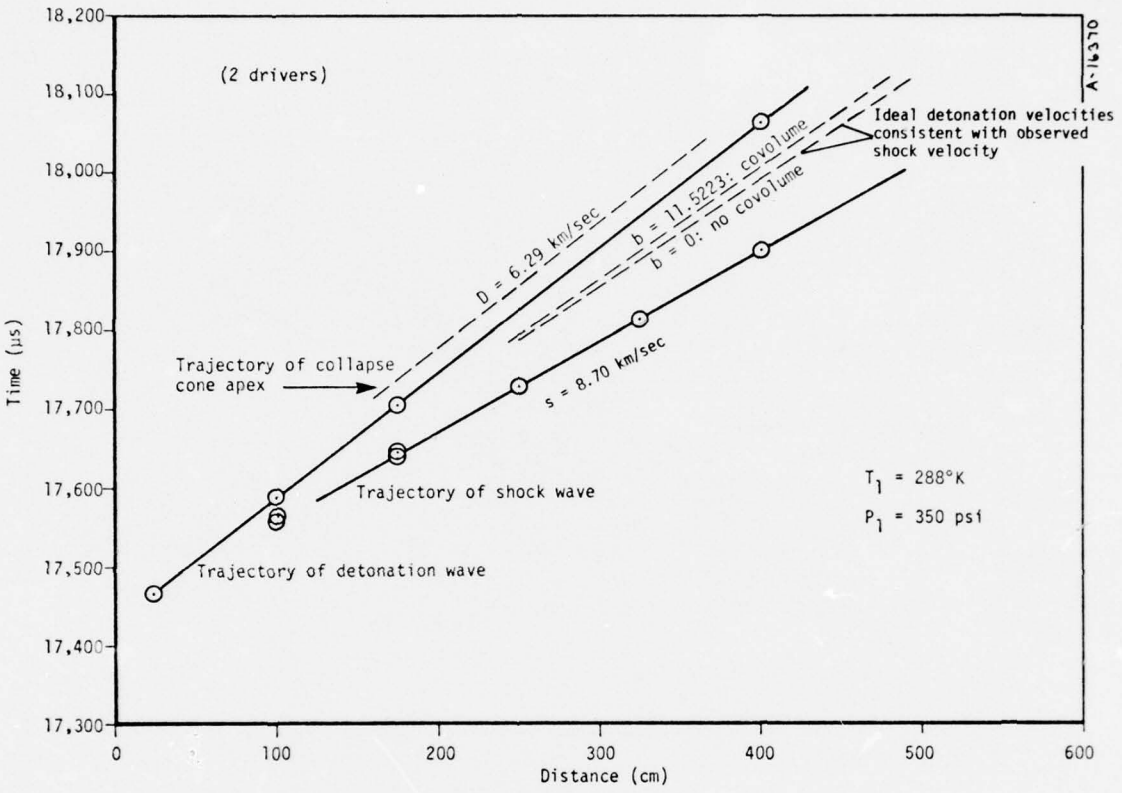

Figure 19. Explosive driver performance for PI, Test Number 7.

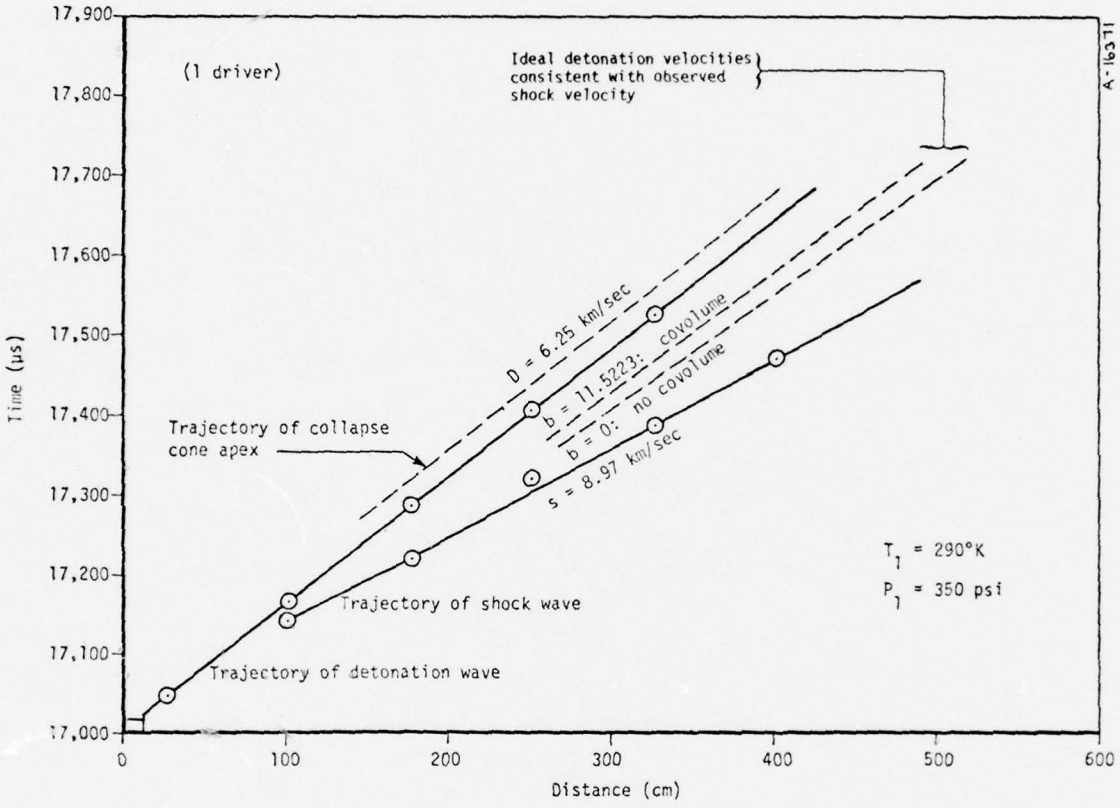

Figure 20. Explosive driver performance for PI, Test Number 8.

to produce the observed shock velocity of 8.7 km/sec. By conservation of momentum, the flux of jet particles would be 80 percent of the theoretical maximum established by Equation (9) for $\sigma = 9°$ and $m_{\ell} = 16.4$ gms/μs.

However, it is more likely that the jet particles would be distributed throughout the shocked gas. Initially jet particles would penetrate the gas ahead of the shock, then as the shock moves downstream, it would engulf the original particles. Meanwhile, the constant flux of new particles would drag decelerate to local flow velocity and travel with the gas behind the shock. This process is illustrated schematically in Figure 21. While the particles can be viewed as decelerating in the gas by drag, the gas can be viewed as flowing through a constant area duct with friction (the sum of particle cross sections is negligible compared to the pressure tube cross section, and the total particle drag can be considered as an average friction factor). Thus, pressure and density would decrease from a maximum behind the shock and the flow Mach number relative to the shock would increase towards unity. The pressure drop through the gas would reflect the jet momentum input. The density drop through the gas would explain the apparent increase in length of the shocked gas.

Assuming a particle diameter of 1.0 mm, the maximum possible flux of jet material would produce 24 particles per microsecond (μs). This production rate seems too low to account for the observed uniformity and reproducibility of the shock trajectories in the PI tests. An assumed particle diameter of 0.1 mm would result in a production of 24,000 particles per μs (which seems to be a more reasonable value) for the theoretical maximum flux of jet material.

If these solid or liquid particles were roughly spherical, the drag coefficient would be about 0.4 and constant (10^3 < Reynolds number < 10^5). A typical deceleration time from 12.5 km/sec to 7 km/sec in the shocked hydrogen is 250 μs. A deceleration time of 250 μs is consistent with the model in which many small particles decelerate and distribute themselves throughout a volume of shocked gas.

A jet mass flux of 25 to 50 percent of the theoretical maximum seems reasonable in view of the above considerations. This would lead to an injection of 15 to 30 grams of small steel particles into the driver gas for each driver.

The drivers used by PI in Tests 1 to 4 do not exhibit the severe jetting characteristics as do the drivers used in Tests 5 to 8. Results of Test 1 are presented in Figure 22. The layer of nitromethane used to collapse the pressure tube was increased after Test 4, resulting in the badly jetting driver operation described above. It is not certain what effect the limited jetting observed in Tests 1 to 4 would have on launcher performance, however, with the severely jetting

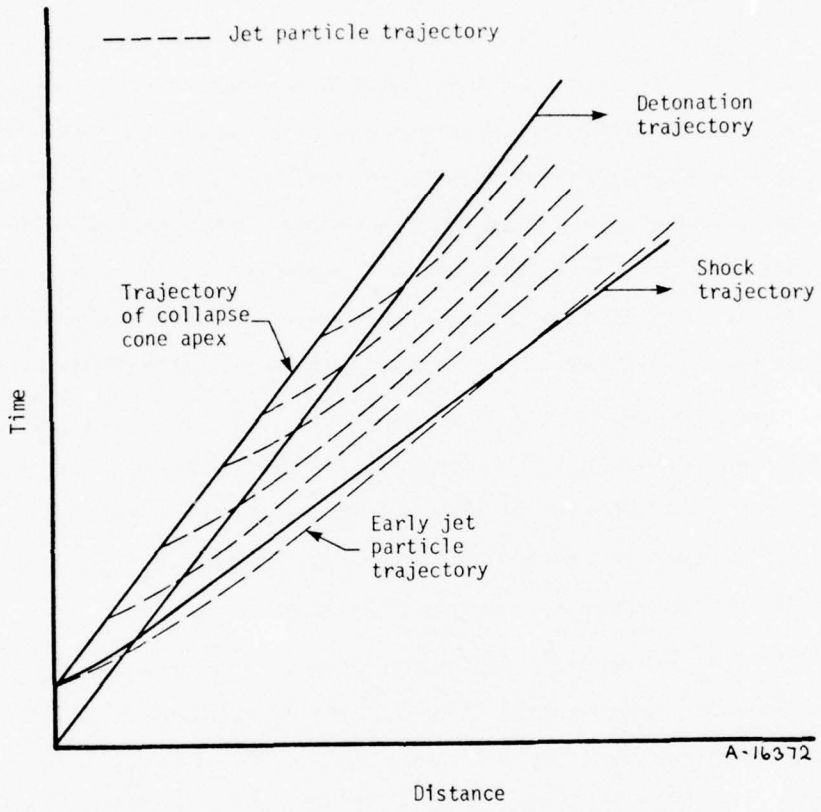

Figure 21. Schematic diagram of jet particle trajectories in a jetting driver.

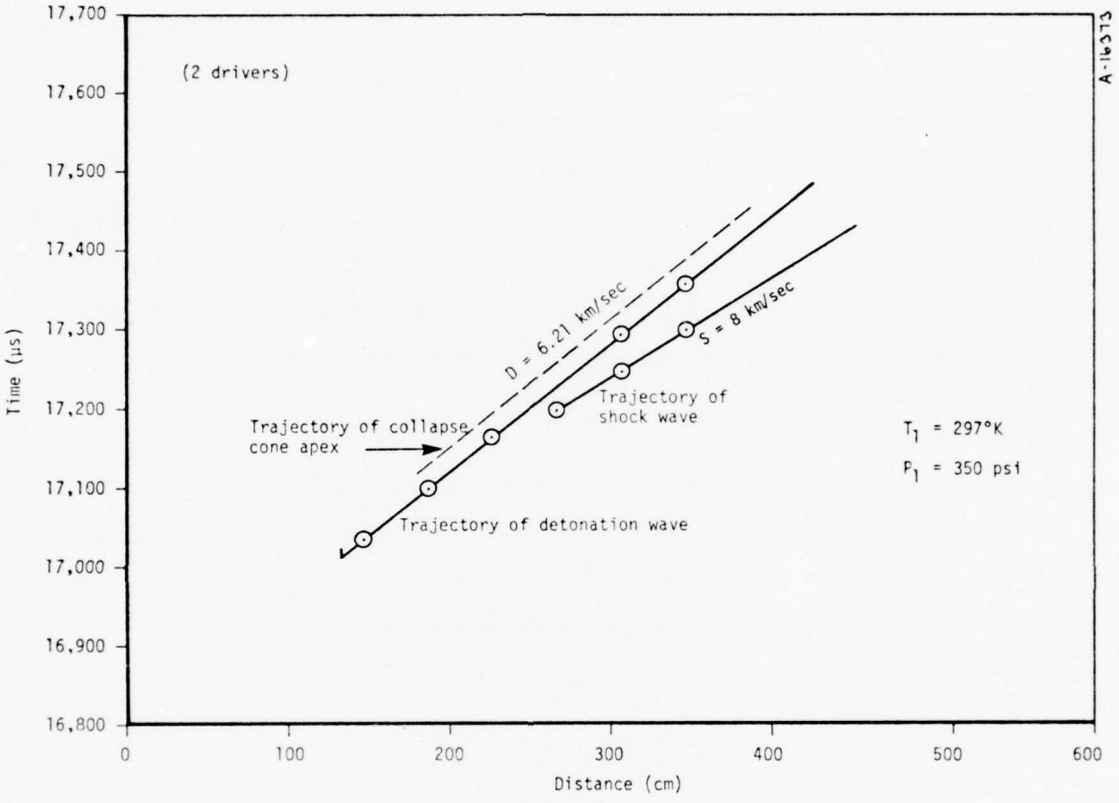

Figure 22. Explosive driver performance for PI, Test Number 1.

drivers used in Tests 5 to 8, launcher performance can be expected to be adversely affected. The many small particles may cause erosion of the launcher parts downstream of the injection ports and possibly into the launch tube. If driver jet particles are carried into the launch tube they can also absorb reservoir energy as they reaccelerate with the flow.

4.2 INJECTION OF SHOCKED GAS INTO THE COMPRESSOR SECTION

In the launcher configuration used by PI, two relatively large drivers were used to inject shocked gas into the compressor. Because the combined cross sectional area of the drivers is somewhat greater than that of the compressor, the flow of injected gases can choke. The resulting reduction in mass flowrate can be a major design problem. In calculating injection gas dynamics, the most accurate equation of state for hydrogen should be used, since the nature of the injection wave system is sensitive to flow Mach number, isentropic index, etc. In addition, a considerable fraction of the driver gases may be trapped between the driver termination flange and the injection ports in the PI design, even if there is no reduction in injection mass flowrate.

4.2.1 Injection Through a Standing Oblique Shock

In the geometries tested by PI, the shocked driver gases must negotiate a turn during injection. In Tests 1 through 7 the turning angle was 45° for both drivers. In Test 8, only one driver was used and the turning angle was reduced to 24°. For Tests 1 through 7, the compressor cross section available to the flow was less than the sum of the cross sections of the two drivers. Specifically,

$$\frac{A_{\text{compressor}}}{A_{\text{both drivers}}} = 0.739$$

In Test 8 the cross section available to the flow increased from driver to compressor. The area ratio was 1.479.

It is postulated that under favorable conditions and after a start-up process, most of the driver gases will be injected through a standing oblique shock at the injector port as shown below:

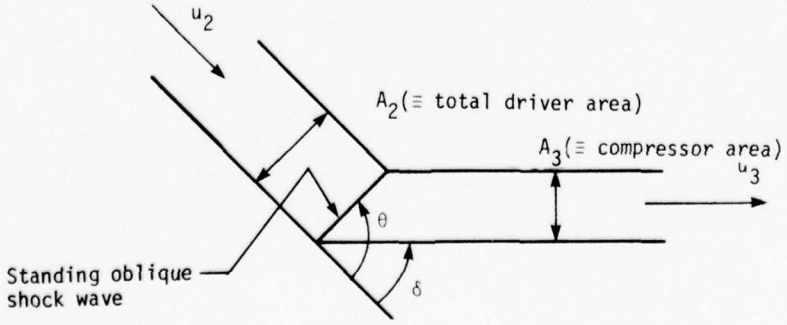

Here θ = shock angle

δ = flow deflection angle

The jump relations across the oblique shock are solved iteratively, using the full equation of state for hydrogen given by Equations (A_1) to (A_7) and noting the invariance across the shock of the tangential velocity component (Reference 5).

The flow deflection angle is computed using

$$\delta = \tan^{-1} \left\{ \frac{\tan \theta \, (1 - \rho_2/\rho_3)}{\rho_2/\rho_3 \, \tan^2\theta + 1} \right\} \tag{10}$$

In Figure 23, the variation of deflection angle with shock angle is shown for the range of shock velocities 7.5 km/sec < s < 9 km/sec. The maximum possible flow deflection angle with this postulated wave system is about 13° with a shock velocity of 7.8 km/sec, characteristic of a properly operating driver. If covolume effects are suppressed, the calculated maximum flow deflection angle is 21°, which illustrates the importance of accurately representing the equation of state.

By the above analysis, the minimum required area ratio to pass the flow is formed from

$$\frac{A_3}{A_2} = \left[\frac{\sin (\theta - \delta)}{\sin \theta} \right]_{\delta = \delta_{max}} \tag{11}$$

For a properly operating driver

$$\left. \frac{A_3}{A_2} \right|_{min} = 0.857$$

It must be concluded that a single stationary oblique shock cannot turn the flow in the PI launcher configuration, since the injection angle is too large and the available compressor cross section is too small. Most likely, a normal shock must propagate back up the driver injection ports to reduce the flow to subsonic conditions for injection.

4.2.2 Subsonic Injection of Driver Gases

A simple flow model is presented here to provide a rough estimate of mass flowrate reduction as the driver gas is injected into the compressor. After a transient startup process, a return shock is assumed to propagate back up the injection port into the explosive driver. The flow behind the return shock is subsonic and is assumed to choke as it flows into the smaller available cross

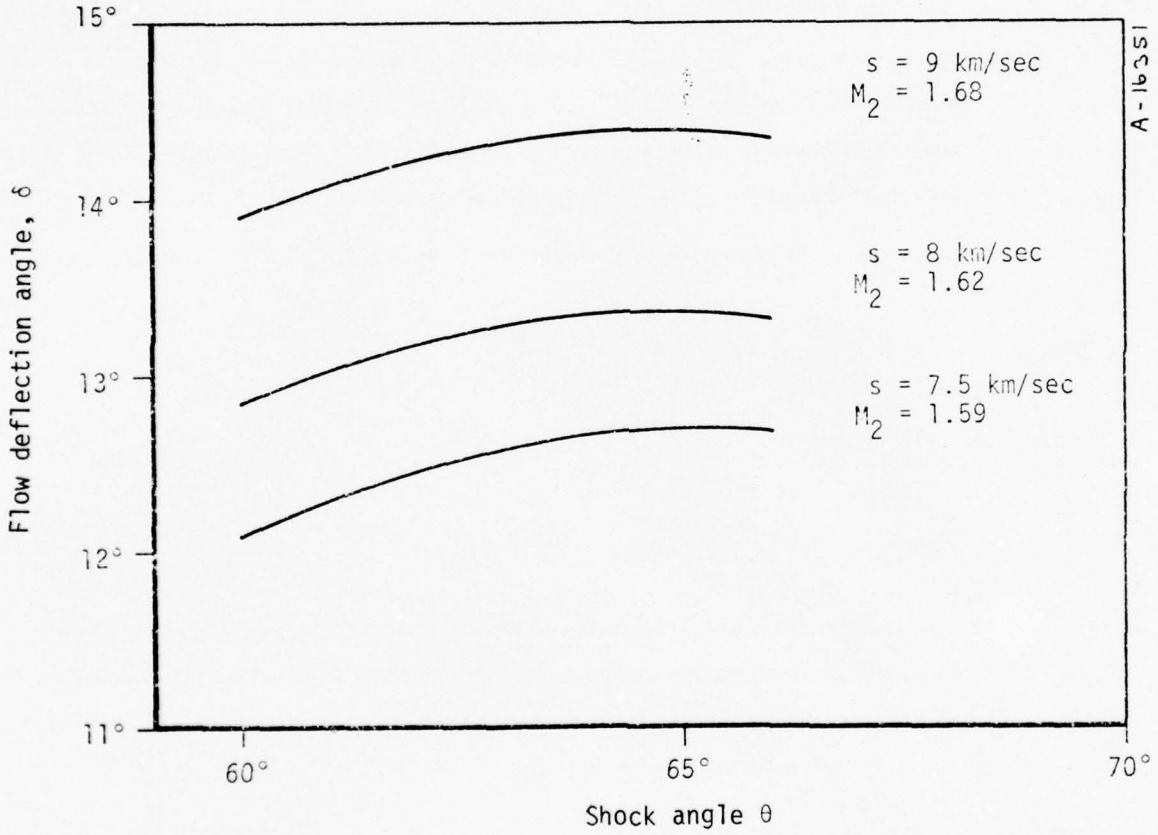

Figure 23. Influence of driver shock velocity on oblique shock turning angle at injection.

section of the compressor. The strength of the return shock is adjusted so that the flow down the compressor is at sonic or choked conditions as shown below:

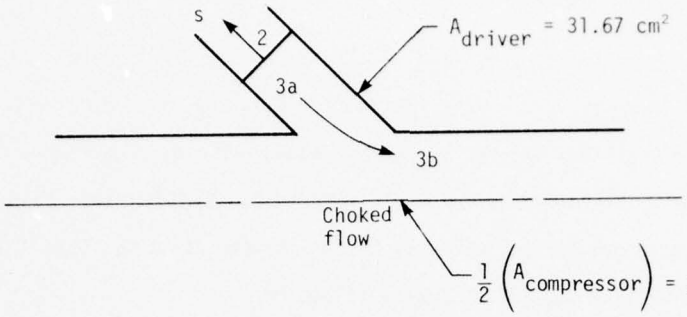

This simple model neglects the change in momentum of the flow as it turns and other three-dimensional effects, such as a vena contracta, which would tend to further restrict mass flowrates.

Conditions across the return shock are calculated iteratively using the full equation of state for hydrogen. The subsonic flow behind the return shock (State 3a) then undergoes an area reduction and accelerates to sonic conditions (State 3b) according to the steady energy and continuity equations and the isentropic condition, $\Delta S = 0$.

For example, in the geometry of PI Tests 1 to 7, the conditions behind the driver shock for ideal driver behavior are:

$$p_2 = 0.974 \text{ kb}$$

$$u_2 = 6.25 \text{ km/sec}$$

$$\rho_2 = 0.0098 \text{ gm/cm}^3$$

Behind a return shock propagating back up the driver at 0.75 km/sec, the conditions are:

$$p_{3a} = 3.5 \text{ kb}$$

$$u_{3a} = 2.52 \text{ km/sec}$$

$$\rho_{3a} = 0.0210 \text{ gm/cm}^3$$

After injection into the compressor section, the flow is sonic with:

$$p_{3b} = 2.1 \text{ kb}$$

$$u_{3b} = 4.7 \text{ km/sec}$$

$$\rho_{3b} = 0.0153 \text{ gm/cm}^3$$

This combination of conditions is sufficient to provide sonic flow in the cross sectional area which is available in the compressor. For the return shock speed of 0.75 km/sec, the mass flowrate is reduced to 86 percent of its unimpeded value.

The compressor cross sectional area ratio required to choke the flow is shown in Figure 24 as a function of return shock velocity. The reduction in mass flowrate as a function of return shock velocity is also given. From this figure, it can be shown that a vena contracta of 10 percent of the compressor diameter would further reduce mass flowrate to about 75 percent of its unimpeded value. For precisely timed compressor piston arrivals typical of the PI tests, these reduced mass flowrates could result in significant gas losses during injection.

4.2.3 Driver Termination Dynamics

In the PI launcher configurations, the termination of the explosive drivers is considerably upstream of the injection ports. Simple calculations indicate that the rarefaction generated by the termination of the explosively formed piston can bring to rest (and therefore trap) a substantial fraction of driver gases within the drivers. For conditions typical of PI Test 7, rough estimates indicate that 35 to 40 percent of the driver gas can be lost to the system by this mechanism (after accounting for the return shock condition considered above).

In conclusion, a substantial fraction of driver gases was not injected in the PI tests because of explosive driver termination dynamics and mass flowrate reduction during injection. Thus, the effective G/M_p ratios in the PI tests might have been only about half as great as expected. Since PI launcher performance was already shown to be sensitive to changes in the G/M_p ratio (Section 3.4), it is not surprising that muzzle velocities were substantially lower than anticipated.

4.3 PROJECTILE FRICTION

Friction between the projectile and launch tube can substantially reduce projectile acceleration, if the prelaunch clearances are too small. A 5-kb pressure applied to the base of an aluminum projectile* which is free to expand in the radial direction dictates a minimum acceptable prelaunch clearance of about 0.003 cm. The PI clearances, before the barrel was enlarged due to erosion, ranged from approximately 0 to 0.005 cm. Projectile friction clearly existed in some instances.

For example, assuming negligible prelaunch clearance, the radial wall stress is (Reference 4)

$$S_R = \frac{\mu_p}{1 - \mu_p} \frac{p}{2} \tag{12}$$

*Modulus of elasticity ≈ 700 kb (10^7 psi), Poisson's ratio ≈ 0.33.

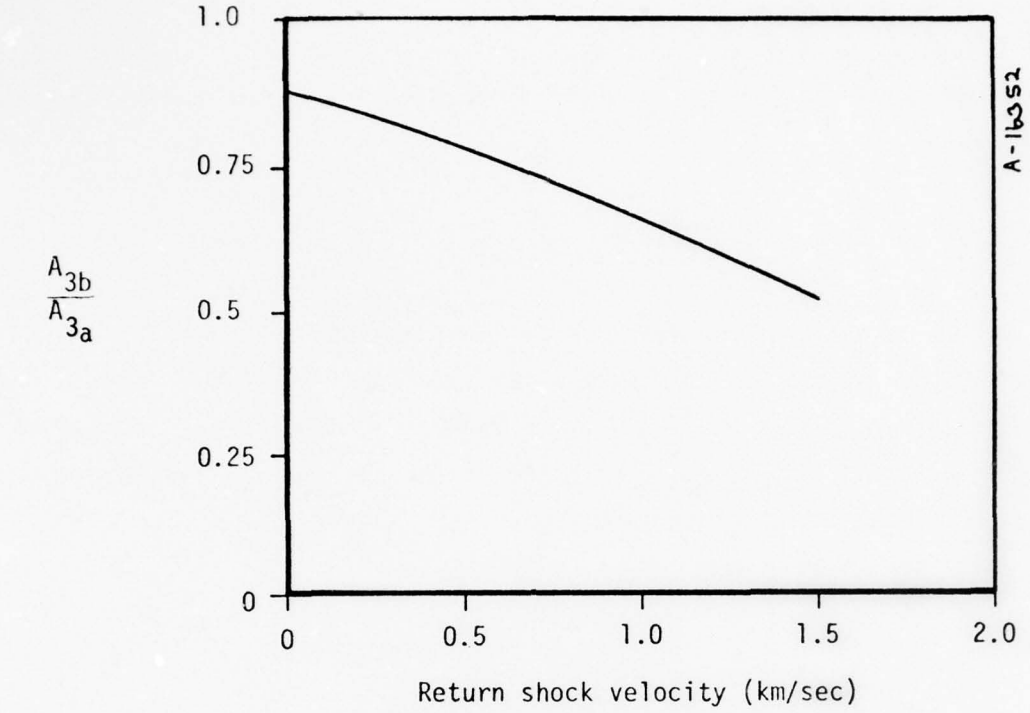

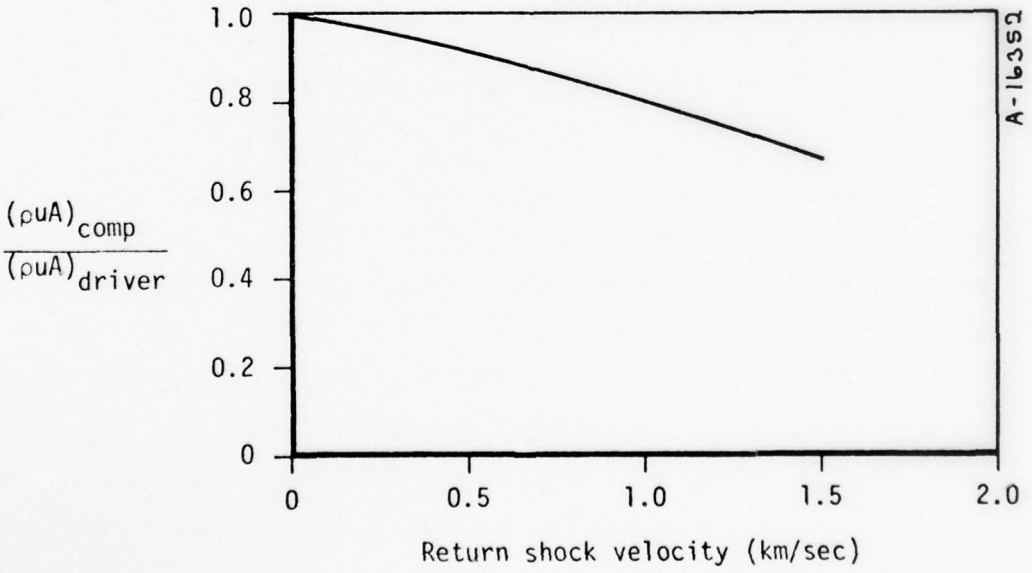

Figure 24. Choked area and mass flow degradation resulting from a normal shock returning back through the driver cross sectional area.

where μ_p = Poisson's ratio

p = projectile base pressure

For a projectile of diameter, D, and length, ℓ, the accelerating force is $p(\pi/4)/d^2$, and the retarding force is $f_s[\mu_p/(1 - \mu_p)]\ p/2$, where f_s is the coefficient of sliding friction. The ratio of retarding force to accelerating force is

$$\phi = 2\ f_s \frac{\mu_p}{1 - \mu_p} \frac{\ell}{D} \tag{13}$$

This ratio is independent of pressure level. For the PI configuration, the projectile ℓ/d is 2.4, the coefficient of sliding friction (aluminum on steel) is 0.47, and Poisson's ratio is 0.33. The ratio of retarding force to accelerating force is calculated to be slightly greater than 1. This is clearly not possible, but this simple approach does indicate that projectile friction can be a significant loss mechanism if very close tolerances are used.

4.4 BARREL BOUNDARY LAYER EFFECTS

The shape of the boundary layer in a launcher is approximated below.

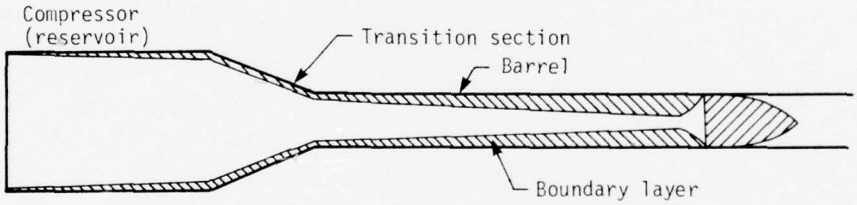

The boundary layer has a number of competing effects on ballistic performance which warrant the following general discussion before proceeding with specific evaluations.

The condition at the wall of zero velocity causes a retarding effect to exist through the shear action within the boundary layer. The retardation approaches zero as the edge of the boundary layer, or the core flow, is approached. If the internal surface of the launcher barrel were at the same temperature as the core, this retardation would cause a deficit of mass flux compared to the core flow. However, local continuity considerations would dictate that the core be accelerated to compensate for the deficit of mass flux within the boundary layer.*

The internal surface temperature of the launcher barrel is usually much lower than the core temperature. Consequently, the higher densities near the wall within the thermal boundary layer

*It is more precise to say that the core flow would behave as though the flow were inviscid, but with the core flow area varying with distance down the barrel. This influences global continuity, which may or may not cause the local core flow to be accelerated.

tend to compensate the mass flux for the lower velocities within the hydrodynamic boundary layer. The net effect is that the core flow is typically influenced very little by the boundary layer. This effect depends upon the magnitude of the boundary layer displacement thickness

$$\delta^* = \int_0^{\delta} \left(1 - \frac{\rho u}{\rho_i u_i}\right) dy \tag{14}$$

where ρ = density

u = velocity

y = direction normal to surface

δ = boundary layer thickness

i = core property

which is typically near zero in a launcher barrel.

If the core flow is not affected by the boundary layer (i.e., $\delta^* \approx 0$), then the ballistic performance will not be modified. That is, in spite of significant heat and momentum transfer from the gas flow behind the projectile, the influence on the projectile base pressures will be negligible as long as the boundary layer does not extend to the center of the barrel. In other words, boundary layer momentum and heat transfer effects could be ignored in terms of ballistic performance, if the launcher L/D is small enough to obviate boundary layer closure.

Subsequent to boundary layer closure, shear is transmitted across the entire cross section (leading to reduced base pressures), and the entire cross section obtains lower temperatures due to heat transfer (also leading to lower base pressures). Consequently, the discriminating boundary layer parameter is its thickness, δ, which is evaluated below.

4.4.1 Momentum Losses Due to Boundary Layer Closure

The nonsteady boundary layer is evaluated herein based on the integral analysis of Reference 7. The details of the evaluations that were performed for this program are presented in Reference 8. The following presentation outlines this detailed evaluation.

The nonsteady integral boundary layer momentum equation is derived for quite general boundary conditions in Reference 7. A restricted form of this equation for stationary wall conditions and zero transpiration (or ablation) is:

$$\frac{\partial F}{\partial t} + \frac{u_i}{G}\frac{\partial F}{\partial x} + \left\{\frac{1}{G}\frac{\partial G}{\partial t} + \frac{(H - G)}{G\,u_i}\frac{\partial u_i}{\partial t} + \frac{(1 + H)}{G}\frac{\partial u_i}{\partial x}\right\} F = \frac{\tau_w}{G} \tag{15}$$

where $F = \rho_i u_i \theta$

$\theta = \int_0^\delta \frac{\rho u}{\rho_i u_i} (1 - u/u_i)\, dy$

$H = \delta^*/\theta$

$G = H - \delta^*_\rho/\theta$

$\delta^*_\rho = \int_0^\delta (1 - \rho/\rho_i)\, dy$

τ_w = wall shear $\equiv \rho_i u_i^2 C_f/2$

x = axial coordinate

t = time

Reynolds numbers within launcher barrels are typically high enough to produce turbulent boundary layer conditions along all surfaces. Under these conditions, but for steady flow, a convenient relation for friction factor is (Reference 9)

$$\frac{C_f}{2} = 0.013\, I_p \left(\frac{\rho_i u_i \theta}{\mu_i}\right)^{-1/4} \tag{16}$$

where

$$I_p = \frac{\rho'}{\rho_i}\left(\frac{\mu'}{\mu_i}\right)^{1/4}$$

' symbol denotes properties evaluated at reference enthalpy conditions, $h' = 0.36\, h_i + 0.19\, h_r + 0.45\, h_w$

h_r = recovery enthalpy = $h_i + R\, u_i^2/2$

R = recovery factor (usually slightly less than 1.0 in gases)

w denotes gas properties evaluated at the wall temperature

μ = viscosity ($= 1.137 \times 10^{-6}\, T^{(\omega)}(°K)$ - gm/(cm·sec), $\omega = 0.75$)

Various boundary layer shape parameters have been evaluated (Reference 10) based on the approach outlined in Reference 9. The results for a turbulent 1/7 power velocity profile are presented in Figure 25. It is noted that G is approximately equal to 1.3, independent of wall temperature. Note also that the function, I_p, increases with decreasing wall to edge temperature ratio

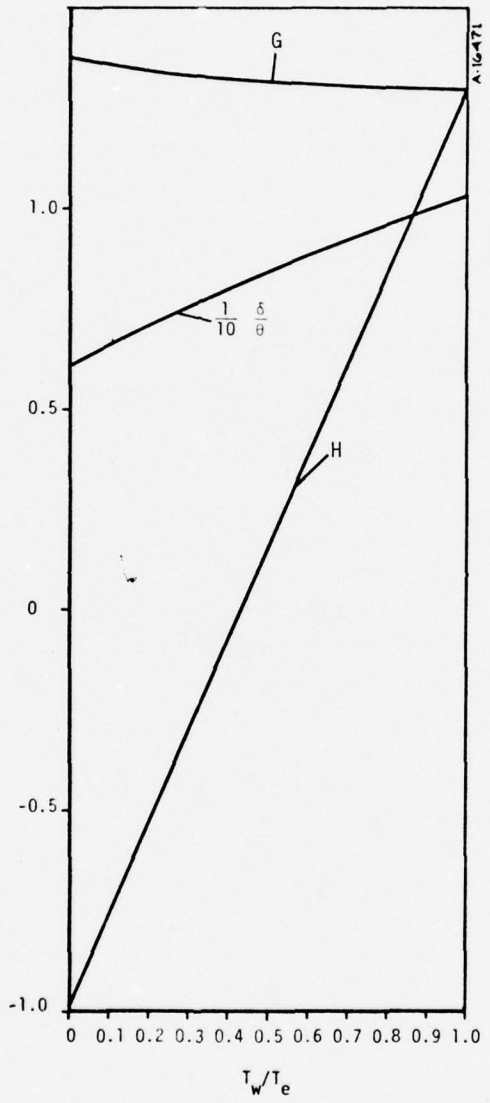

Figure 25. Turbulent boundary layer shape factors, 1/7 power velocity profile.

($I_p \approx 1.5$ at $T_w/T_i \approx 0.2$). Consequently, the shear function employed in the remainder of this evaluation is based on Equation (16) and these latter observations.

$$\frac{\tau_w}{G} = \frac{0.013\ I_p}{G} \frac{\rho_i u_i^2}{\left(\frac{\rho_i u_i \theta}{\mu_i}\right)^{1/4}} \approx \frac{0.015\ \rho_i u_i^2}{\left(\frac{\rho_i u_i \theta}{\mu_i}\right)^{1/4}} \tag{17}$$

Equation (15) can be solved using the method of characteristics. In this method, a partial differential equation in two independent variables is solved by simultaneous solutions of two total differential equations in one independent variable (one equation being the integral momentum equation, the other being the equation for the characteristic). Choosing time as the independent variable, after inclusion of Equation (17) the appropriate equations are:

$$\left.\frac{dF}{dt}\right|_c + \left\{ \frac{H - G}{G\ u_i} \left.\frac{du_i}{dt}\right|_c + \left[\frac{(1 + H)}{G} - \frac{H - G}{G\ u_i} \left.\frac{dx}{dt}\right|_c \right] \left.\frac{\partial u_i}{\partial x}\right|_c \right\} \quad F = 0.015\ \mu_i^{1/4} \rho_{i,c} u_{i,c}^2\ F^{-1/4} \tag{18}$$

$$\left.\frac{dx}{dt}\right|_c = \frac{dx_c}{dt} = \frac{u_{i,c}}{G} \tag{19}$$

where c denotes properties along a characteristic.

Equations (18) and (19) can be solved for arbitrary core flow condition histories. However, for this effort, particular core behaviors have been selected for certain idealized ballistic cycles, such that

$$\left.\frac{\partial u_i}{\partial x}\right|_c = \frac{d\ \ln\ \xi}{dt}\ ,\ \xi = \xi(t)\ \text{(to be defined)} \tag{20}$$

The solution of Equation (18) can be obtained by formal means after invoking:

- Equation (20)
- The boundary condition of zero boundary layer thickness at the origin of a characteristic (at time t_1)
- The simplifications that H and G are constants.

$$F = \left\{ \frac{5}{4} \times 0.015\ u_{i,c}^{-B_1}\ \xi^{-B_2} \int_{t_i}^{t} u_{i,c}^{B_1+2}\ \xi^{B_2}\ \rho_{i,c} \mu_{i,c}^{1/4}\ dt \right\}^{4/5} \tag{21}$$

$$B_1 = \frac{5(H - G)}{4G}\ ,\ B_2 = \frac{[5(2G + H(G - 1)]}{4G^2}$$

Note that all the parameters in Equation (21) vary with time along characteristics. The characteristic is developed through solution of Equation (19). The properties and the solution of Equation (19) depend upon the core flow descriptions which are evaluated in the following paragraphs.

Two limiting ballistic cycles are considered:

- Constant base pressure launcher (CBPL)
- Simple wave launcher (SWL)

It is convenient to work in nondimensional coordinates to describe ballistic behavior

$$x^\star \equiv \frac{\nu(\gamma + 1)}{2a_o^2} x$$

$$t^\star \equiv \frac{\nu(\gamma + 1)}{2a_o} t$$

$$u^\star \equiv \frac{(\gamma + 1)}{2a_o} u$$

$\gamma \equiv$ isentropic exponent

$\nu \equiv$ initial acceleration of the projectile

$a_o =$ initial speed of sound in the chamber

Equation (21) is transformed with these variables to:

$$\theta^\star = \frac{0.0548}{u^\star_{i,c}} \left(\frac{\nu \mu_o}{a_o^3 (\gamma + 1)^2 \rho_o} \right)^{1/5} \left(\frac{\rho_o}{\rho_i} \right) \psi^{4/5} \tag{22}$$

$$\psi \equiv u^{\star\,-B_1}_{i,c} \xi^{-B_2} \int_{t^\star_{i,z}}^{t^\star} u^{\star\,B_1+2}_{i,c} \xi^{B_2} \left(\frac{\rho_{i,c}}{\rho_o} \right) \left(\frac{\mu_{i,c}}{\mu_o} \right)^{1/4} dt^\star$$

where $\theta^\star \equiv \frac{\nu(\gamma + 1)}{2a_o^2} \theta$

o denotes conditions at the initiation of projectile motion

z denotes the origin of a characteristic, either at the chambrage (z = c), or along the barrel where the characteristic is originated at the time of projectile passage (z = p)

In the constant base pressure launcher, acceleration is always equal to the initial acceleration, and so the projectile motion is easily evaluated. Continuity, momentum, and energy considerations dictate that gas velocity be independent of distance along the barrel, but vary with time in the same way as the projectile velocity does. (This solution is presented by Seigel in Reference 2.)

$$u_i^* = t^* \tag{23}$$

This cycle is particularly simple in that characteirstics vary in the same way throughout the barrel, and the function, ξ, is invariant ($\xi = 1.0$).

A simple wave launcher with the chamber and barrel cross sections equal is analyzed. The location of the chamber head end is chosen to be far enough away from the chambrage plane so that the reflection of the lead expansion wave (which is generated at the beginning of projectile motion) does not cross the chambrage plane prior to completion of the ballistic event.

This cycle is also considered by Seigel (Reference 2), but without obtaining an explicit evaluation of the distributions of gas properties along the barrel. Reference 8 has shown these properties to vary isentropically, with the following velocity distribution.

$$u_i^* = \frac{x^* + t^*}{1 + t^*} \tag{24}$$

such that

$$\xi_{SWL} = (1 + t^*)^{\frac{2}{\gamma+1}} \tag{25}$$

The equations of projectile motion and all equations which are necessary to the evaluation of Equation (22) are presented in Table 5. Both cycles yield pressures which decrease with distance down the barrel. However, pressure decreases with time at the chambrage plane of the SWL, whereas it must increase with time to maintain base pressure in the CBPL. Gas temperatures change in the same directions as the pressures, requiring isentropic compression of the chamber gases with time for the CBPL.

In terms of two-stage launchers, the CBPL can be thought of as representing a specific history of compressor piston movement toward the chambrage plane during the ballistic event. The SWL, however, can be thought of as representing a specific piston movement away from the chambrage plane. Presumably, results evaluated from these idealized cycles will reveal representative limits of boundary layer behaviors for two-stage launchers.

TABLE 5. TIME (t^*) VARIATIONS OF PROJECTILE MOTION AND INVISCID CHARACTERISTIC PROPERTIES

Parameters	CBPL	SWL
x_p^*	$\frac{t^{*2}}{\gamma + 1}$	$1 + \frac{2(1 + t^*)}{\gamma - 1} - \frac{\gamma + 1}{\gamma - 1}(1 + t^*)^{\frac{2}{\gamma+1}}$
u_p^*	t^*	$\frac{\gamma + 1}{\gamma - 1}\left[1 - (1 + t^*)^{-\frac{\gamma-1}{\gamma+1}}\right]$
x_c^* (1)	$x_{1,z}^* + \frac{t^{*2} - t_{1,z}^{*2}}{2\beta}$	$1 + \frac{1 - t^*}{\beta - 1} - \left(1 - x_{1,z}^* + \frac{1 + t_{1,z}^*}{\beta - 1}\right)\left(\frac{1 + t^*}{1 + t_{1,z}^*}\right)^{\frac{1}{\beta}}$
$x_{1,p}$ (2)	$\frac{t_{1,p}^{*2}}{\gamma + 1}$	$1 + \frac{2(1 + t_{1,p}^*)}{\gamma - 1} - \frac{\gamma + 1}{\gamma - 1}(1 + t_{1,p}^*)^{\frac{2}{\gamma+1}}$
$x_{1,c}^*$ (3)	0	0
$u_{i,c}^*$	t^*	$\frac{x_c^* + t^*}{1 + t^*}$
ξ	1.0	$(1 + t^*)^{\frac{2}{\gamma+1}}$
$\frac{T_{i,c}}{T_o}$	$1 + 2\frac{\gamma - 1}{\gamma + 1}\left(\frac{t^{*2}}{\gamma + 1} - x_c^*\right)$	$\left(1 - \frac{\gamma - 1}{\gamma + 1}\frac{x_c^* + t^*}{1 + t^*}\right)^2$
$\frac{\rho_{i,c}}{\rho_o}$	$\left(\frac{T_{i,c}}{T_o}\right)^{\frac{1}{\gamma-1}}$	
$\frac{p_{i,c}}{p_o}$	$\left(\frac{T_{i,c}}{T_o}\right)^{\frac{\gamma}{\gamma-1}}$	
$\frac{\mu_{i,c}}{\mu_o}$	$\left(\frac{T_{i,c}}{T_o}\right)^{\omega}$	

(1), (2), (3): See notes on following page

NOTES TO TABLE 5

(1) $t^* > t^*_{1,z}$

$$\beta = \frac{\gamma + 1}{2} G$$

p denotes projectile

c denotes chambrage plane

z denotes that either p or c applies

(2) $x^*_{1,p} = x^*_p (t^*_{1,p})$, projectile originated characteristic

(3) $x^*_{1,c} = 0$, chambrage plane originated characteristic

Projectile motions are presented for both cycles in Figure 26. These are compared with muzzle parameters which have been evaluated in Section 3.* For equivalent muzzle velocities and initial accelerations, the SWL travel time and barrel length are considerably longer than for the CBPL. However, for the same muzzle velocities and barrel lengths, the travel time is shorter for the SWL, requiring higher initial accelerations. These comparisons are made for a muzzle velocity of $u_m^* = 1.0$ in the following example:

COMPARISON OF CBPL AND SWL BALLISTICS, $u_m^* = 1.0$

	t_m^*	$L^*(= x_m^*)$	$\left(\frac{t_{SWL}}{t_{CBPL}}\right)_{v,u_m^*}$	$\left(\frac{L_{SWL}}{L_{CBPL}}\right)_{v,u_m^*}$	$\left(\frac{t_{SWL}}{t_{CBPL}}\right)_{L,u_m^*}$	$\left(\frac{v_{SWL}}{v_{CBPL}}\right)_{L,u_m^*}$
SWL	1.99	1.0	1.99	2.44	0.82	2.44
CBPL	1.0	0.41				

The simplified boundary condition of zero boundary layer thickness at the chambrage plane for all times is not strictly correct. It would be a reasonable approximation for a design with a sharp transition between the chamber and the barrel, but in terms of heat transfer this would be poor design practice. In steady flow, boundary layers are thinned under accelerating inviscid flow conditions. Since flow would be accelerated for practical transition section designs, it is probable that at least the boundary layers are thinnest at the chambrage plane. The assumption of zero thickness here has a negligible effect on boundary layer closure evaluations, and a conservative effect in terms of heat transfer evaluations.

When H is set equal to 0.2 G, B_1 becomes -1. In this case, the simplicity of the CBPL allows a formal integration to be carried out in Equation (22). (The integration must be performed by numerical means for the SWL due to the complexity of the equation for the characteristics.) The final relation for momentum thicknesses for the CBPL is (H = 0.2 G).

$$\theta^* = \frac{0.0315}{t^{*1/5}} \left(\frac{\nu \mu_o}{a_o^3 (\gamma + 1)^2 \rho_o} \right)^{1/5} \left(\frac{T_{i,c}}{T_o} \right)^{-\frac{1}{\gamma - 1}} \left\{ \frac{\left(\frac{T_{i,c}}{T_o} \right)^{\lambda} - \left(\frac{T_{i,z}}{T_o} \right)^{\lambda}}{B_3^{\lambda}} \right\}^{4/5} \qquad (26)$$

*The SWL and CBPL results generally span the earlier results. The results of Section 3 cluster near the SWL results, implying the possibility of higher ideal muzzle velocities than found in Section 3.

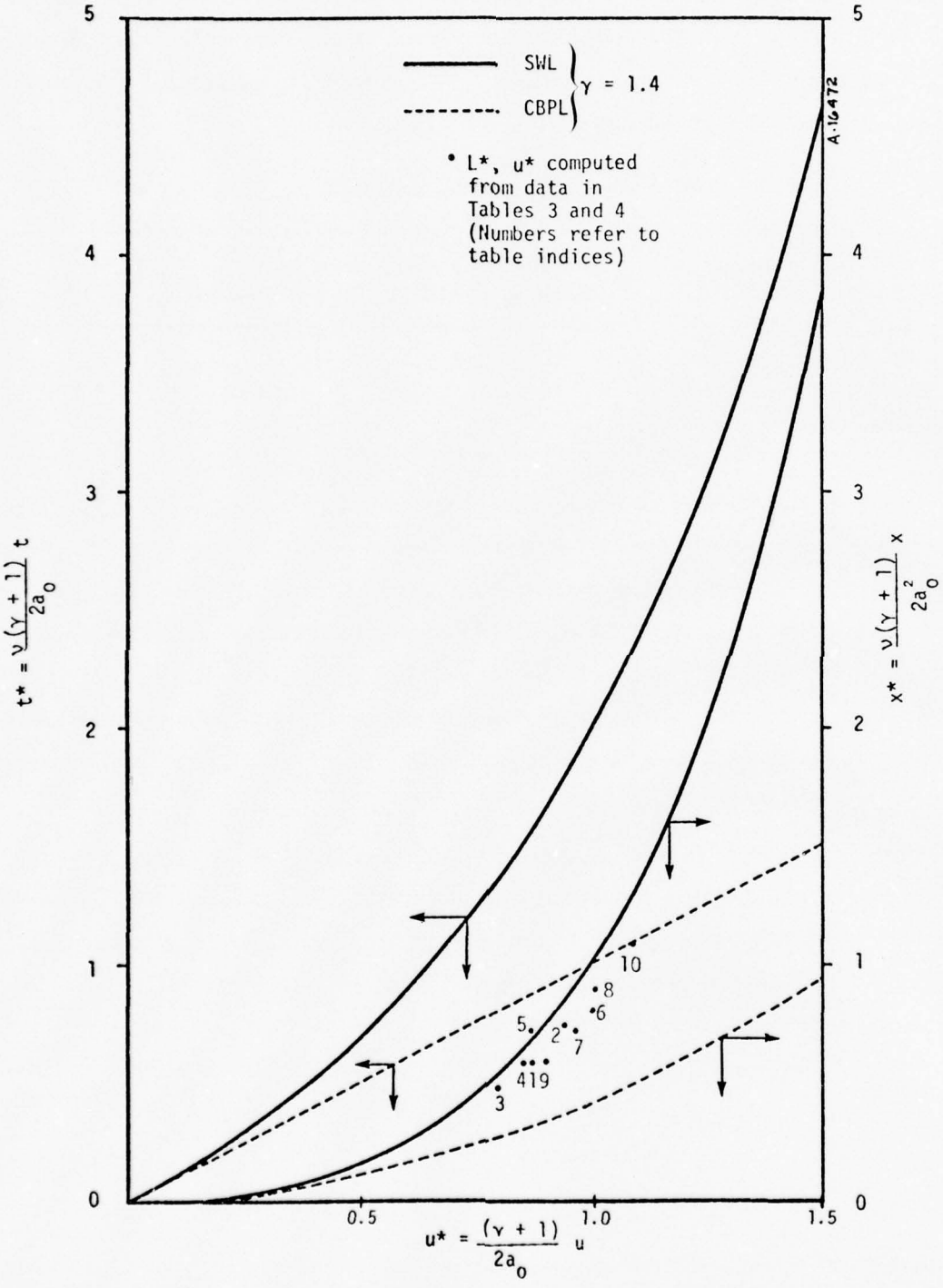

Figure 26. Generalized ballistic performance.

where $\lambda = \frac{\gamma}{\gamma - 1} + \frac{\omega}{4}$

$$B_3 = \frac{2(G - 1)}{G} \frac{\gamma - 1}{(\gamma + 1)^2}$$

For both cycles, maximum momentum thickness occurs very near the characteristic originated at zero time which is common to both the chambrage plane and projectile. For this characteristic, Equation (26) becomes:

$$\theta^*_{max} = \frac{0.0315}{t^{*1/5}} \left(\frac{\nu \mu_o}{a_o^3 (\gamma + 1)^2 \rho_o} \right)^{1/5} \left\{ \frac{(1 + B_3 t^{*2})^{\lambda} - 1}{B_3 \lambda} \right\}^{4/5} (1 + B_3 t^{*2})^{-\frac{1}{\gamma - 1}} \qquad (27)$$

For a very high speed of sound in the chamber, t^* is always small, leading to the following approximation of Equation (27):

$$\theta^*_{max, t^* \to o} \approx 0.0315 \left(\frac{\nu \mu_o}{a_o^3 (\gamma + 1)^2 \rho_o} \right)^{1/5} t^{*7/5} \qquad (28)$$

$$\approx 0.0315 \left(\frac{\nu \mu_o (\gamma + 1)^{3/2}}{a_o^3 \rho_o} \right)^{1/5} x^{*7/10}_p$$

Example solutions of Equation (22) along the common characteristics have been performed using both ideal cycles and a muzzle velocity of 6 km/sec. The barrel length is constrained for these calculations to 300 diameters, assuming a 2.54-cm diameter barrel. For the sake of consistency with the derivation of Equations (26) and (27), a wall temperature ratio of 0.55 has been selected which yields H = 0.2 G (Figure 25), and a value of $\delta/\theta = 8.6$. For these assumptions, closure occurs when θ is equal to 0.148 centimeters.

The results are presented in Figure 27. The boundary layer is thicker for a given projectile position for the CBPL than it is for the SWL. This follows from the constraint of the same muzzle velocity and barrel length for both cycles. The SWL starts with a higher chamber pressure and obtains higher projectile velocities at all positions along the barrel except at the muzzle. Gas temperatures are lower in the SWL, so viscosities are lower. For the early part of the SWL motion, the gas densities are higher than in the CBPL. The values of these parameters are such that core Reynolds numbers at the point of peak boundary layer thickness are always higher for the SWL than the CBPL (i.e., under the constraints of same muzzle velocity and barrel length). Consequently, the SWL boundary layers are thinner.

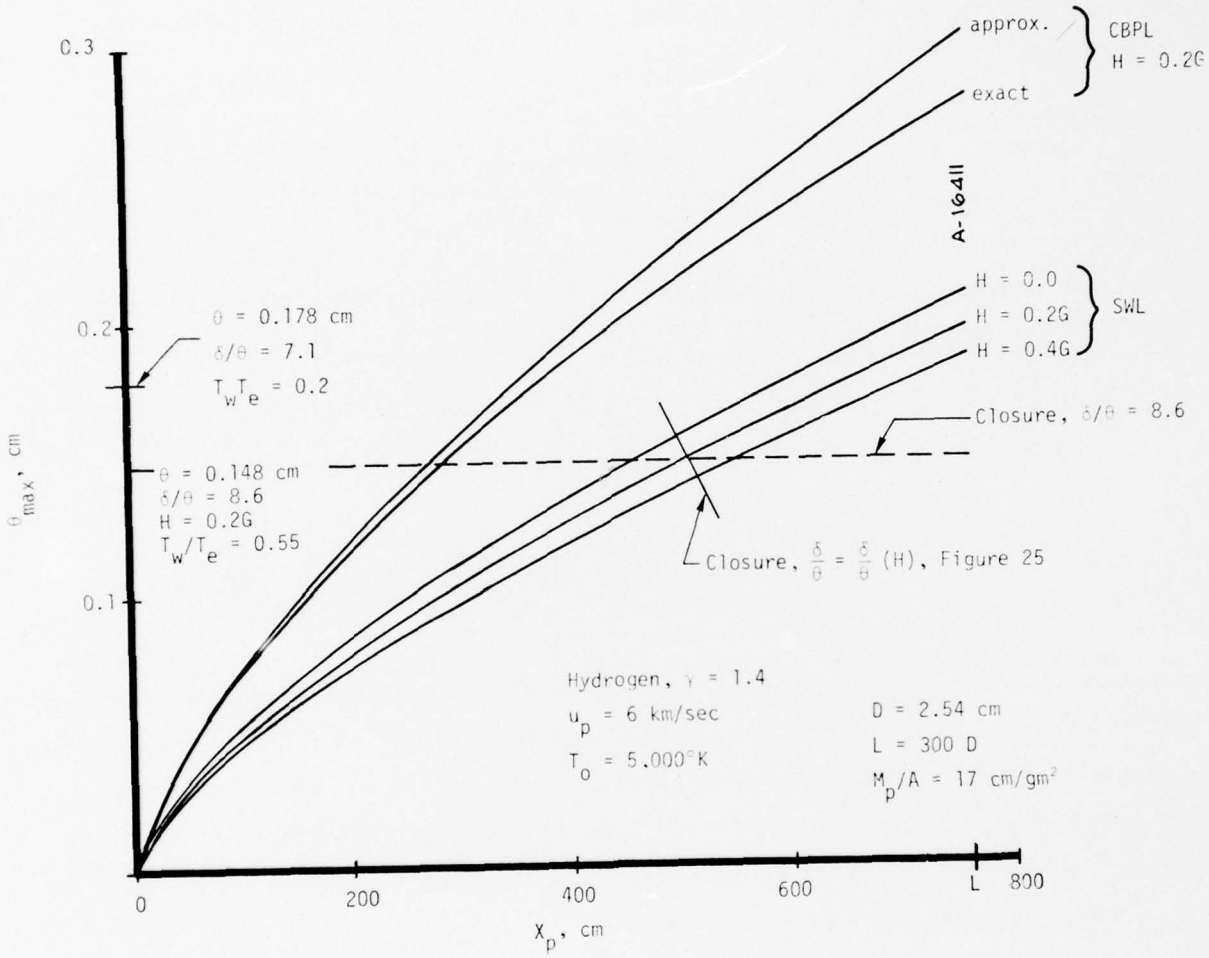

Figure 27. Growth of maximum boundary layer momentum thickness.

Parametric values of H have been employed in the calculations for the SWL. Although peak momentum thicknesses decrease with H, δ/θ increases with H. Consequently, the location of the projectile when closure is obtained is almost independent of H (projectile location varies less than 15 centimeters in Figure 27 for the range of H considered).

Evaluations of the exact solution of Equation (22), (i.e., Equation (26) with H = 0.2 G) and the approximate solution (Equation (28)), for the CBPL are presented in Figure 27. These results compare within about 3 percent near the point of closure, so the approximate results are sufficiently accurate for the following purposes.

It is of interest to determine the effects of muzzle velocity, chamber temperature, and launcher barrel L/D on the location of the projectile at the time of closure. This can be approximated from Equation (28) through setting $\theta_{max} = \frac{D}{2(\delta/\theta)}$:

$$\left(\frac{x_p}{D}\right)_{closure} = \frac{28.7\left(\frac{u_m}{a_o}\right)^{6/7}}{\left(\frac{\delta}{\theta}\right)^{10/7}\left(\frac{\mu_o}{\gamma a_o \bar{m}_p}\right)^{2/7}\left(\frac{L}{D}\right)^{3/7}} \tag{29}$$

where $\bar{m}_p$ = projectile mass per unit area.

Using former dependencies of viscosity and sound speed on temperature, and a perfect-ideal gas,

$$\left(\frac{x_p}{D}\right)_{closure} \propto (u_m)^{6/7}\left(\frac{L}{D}\right)^{-3/7}\left(\frac{\delta}{\theta}\right)^{-10/7} T_o^{-2/7(1+\omega)}\, \bar{m}_p^{2/7} \tag{30}$$

Equation (29) has been evaluated for the projectile areal density that was used in the PI launcher (17 gm/cm^2), and a δ/θ of 7.1. The results are presented in Figure 28.

It is significant to note that if insufficient mass is injected into the chamber, the ideal muzzle velocity will be low. Figure 28 shows that when this happens, boundary layer closure occurs at smaller values of projectile travel. This in turn makes the attainment of the ideal muzzle velocity difficult, since performance falls off after boundary layer closure. Thus, it is not only important to realize full chamber conditions in terms of obtaining maximum ideal velocity, but it is also important in order to minimize departures from ideal behavior due to boundary layer effects.

The results for the SWL in Figure 28 show a greater sensitivity of closure to ideal muzzle velocity than the CBPL does. It is probable that the SWL results approach the CBPL results asymptotically with decreasing muzzle velocity, based on the observed approach of the SWL ballistic performance results to the CBPL results at smaller u_p^* (Figure 26).

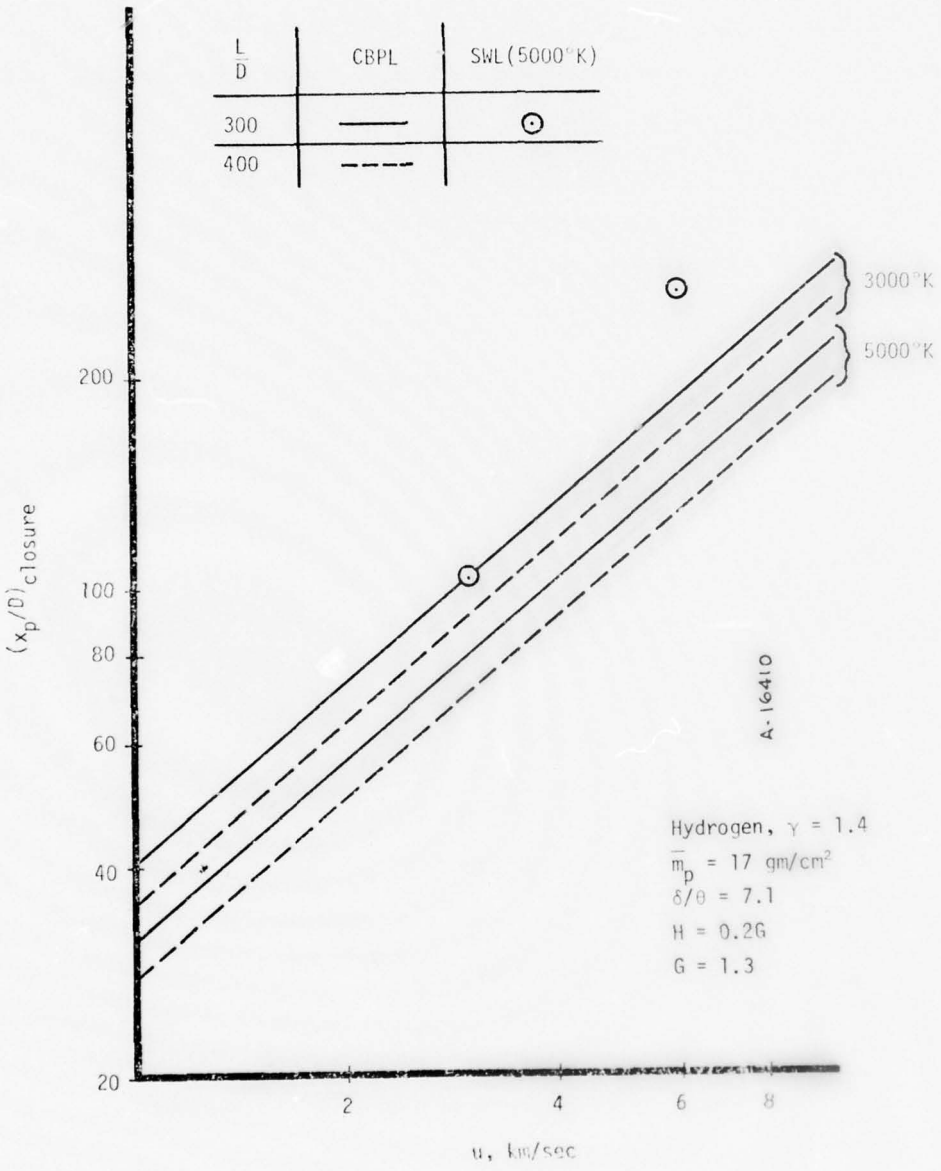

Figure 28. Projectile locations at the times of boundary layer closure.

Although the SWL allows more projectile motion before closure, it is important to remember that this is being obtained here by virtue of higher initial accelerations. If both guns are constrained to the same initial acceleration, the higher L/D required for the SWL offsets this apparent advantage (applying the CBPL rules of Equation (28) to the SWL, doubling the gun L/D will probably reduce the projectile travel to closure for the SWL by about 26 percent). The increased L/D decreases $(x_p/D)_{closure}$, and increases the distance that must be travelled after closure occurs.

The results of these evaluations can now be summarized:

- Boundary layers do not significantly influence ballistic performance until boundary layer closure occurs
- Launcher L/D should be small to minimize boundary layer effects on ballistics
- Allowable L/D's increase with increasing ideal muzzle velocity (i.e., increasing accelerations)
- Phenomena which degrade the chamber conditions in such a way as to reduce the ideal muzzle velocity also reduce the opportunity to achieve even the reduced ideal muzzle velocity because of adverse boundary layer effects
- Quantitative and accurate evaluations of the effects of boundary layer closure on performance require that momentum and heat transfer be coupled to the computation of bulk behavior
- The barrel L/D employed in the PI launcher tests was much greater than is useful. However, the excess barrel length probably neither enhanced nor reduced the muzzle velocity

Estimates of the effects of heat transfer on ballistic performance are presented in the next subsection.

4.4.2 Energy Losses Due to Heat Transfer

It is desirable to estimate the upper limits of ballistic losses due to heat transfer. In addition, heat transfer must be evaluated to estimate the thermal response of the launcher barrel internal surface material. Consequently, the analysis in Section 4.4.1 is extended here and will consider the spatial and temporal variations of heat transfer, as well as the effects of heat transfer on ballistic performance.

It is common, and appropriate in approximate evaluations of this sort, to invoke Reynolds' analogy to evaluate heat transfer, that is:

$$\frac{\dot{q}}{\rho_i u_i (h_r - h_w)} = \frac{C_f}{2} = \frac{0.0195}{\left(\frac{\rho_i u_i \theta}{\mu_i}\right)^{1/4}} \quad \text{(based on } \dot{I}_p = 1.5\text{)} \tag{31}$$

Operating on Equation (31) using the transformed variables, a heat transfer coefficient can be evaluated as follows:

$$H \equiv \frac{q}{(h_r - h_w)} = 0.0276 \left(\frac{\rho_o^3 a_o \mu_o \alpha}{(\gamma + 1)^2}\right)^{1/4} \left(\frac{T_{i,c}}{T_o}\right)^{1/4\left(\frac{3}{\gamma-1} + \omega\right)} u_{i,c}^{*\,3/4}\, \theta^{*\,-1/4} \tag{32}$$

Example axial distributions of heat transfer coefficient obtained through evaluations of Equation (32) for both the CBPL and SWL cycles are presented in Figure 29(a). The times chosen for presentation represent times when the projectile would reach the muzzle for the conditions noted on the figure. The infinite heat transfer coefficients at both the base of the projectile and at the chambrage plane are unrealistic. The finite thickness of the boundary layer at the chambrage plane was discussed in Section 4.4.1. Corrections to this result can by obtained by theoretical means quite easily in principle, but the effort is beyond the scope of the present program. However, except at the projectile, the results in Figure 29(a) at values of x/L greater than about 0.05 are probably quite accurate. As will be seen later, the condition at the base of the projectile is unimportant, because the attenuation of the heat flux there is very rapid.

Minimum heat transfer coefficients exist near the points of maximum boundary layer thickness ($x \approx 580$ cm). Transfer coefficients for the CBPL are on the order of 5 to 30 percent higher than for the SWL. Note that these results are somewhat in error (probably high) in the region where the boundary layer is fully developed (between about 150 and 750 cm for both cycles). Based on the higher heat transfer coefficients and recovery enthalpies* (Figure 29(a) and 29(b)) at the time of projectile exit, the CBPL heat transfer rate is considerably higher than that for the SWL.

The critical area for heat transfer is near the chambrage plane, where transfer coefficients are high and the surface is exposed to hot gases for the longest times. Transfer coefficient histories at two locations near the chambrage plane for both cycles are presented in Figure 30(a). The rapid attenuation of transfer coefficient after passage of the projectile and the attenuation of heat transfer with distance (Figure 29(a)) are apparent in this figure.

*Recovery enthalpies have been computed employing a recovery factor of unity.

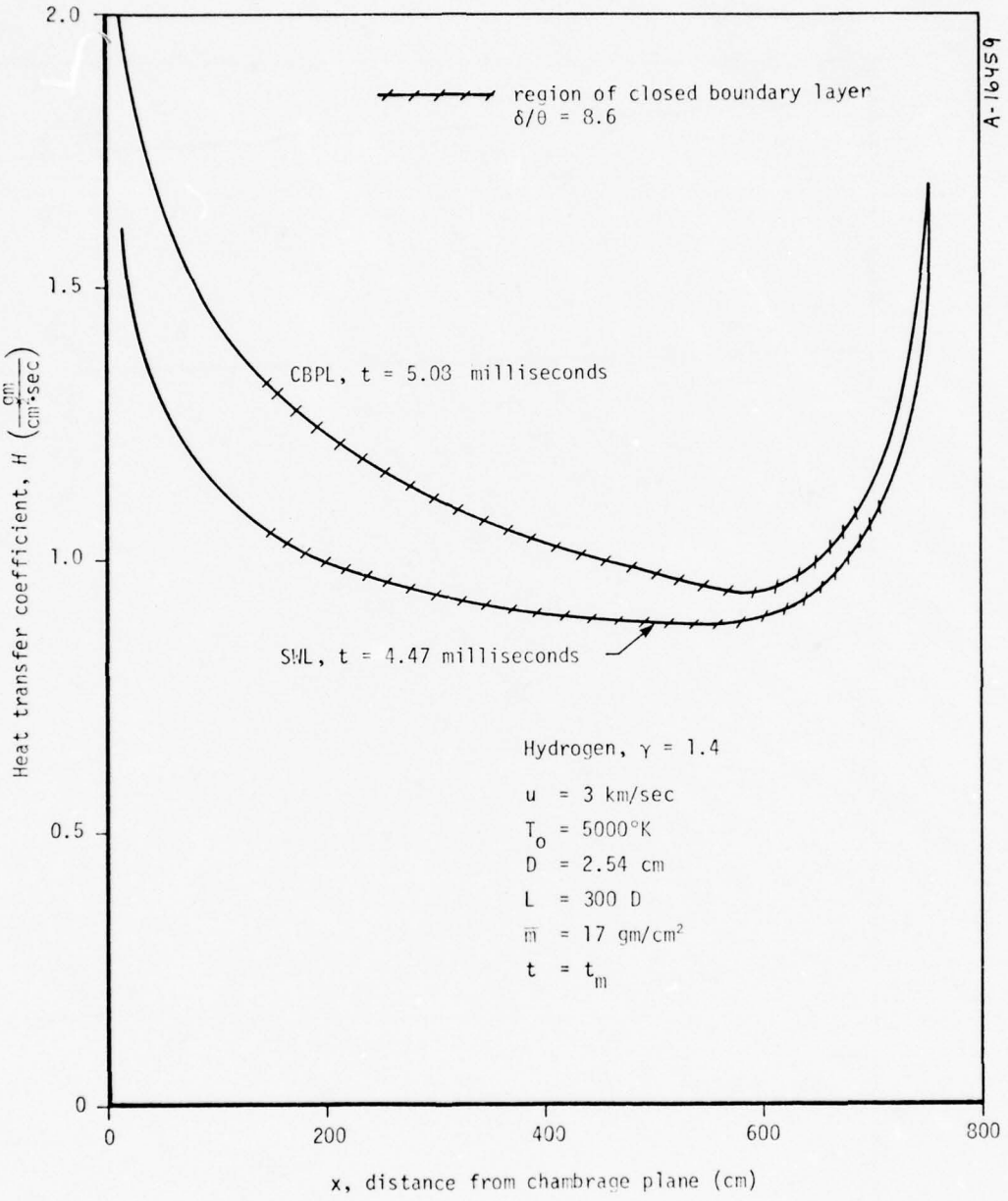

Figure 29a. Axial distribution of heat transfer coefficient at the time of projectile expulsion.

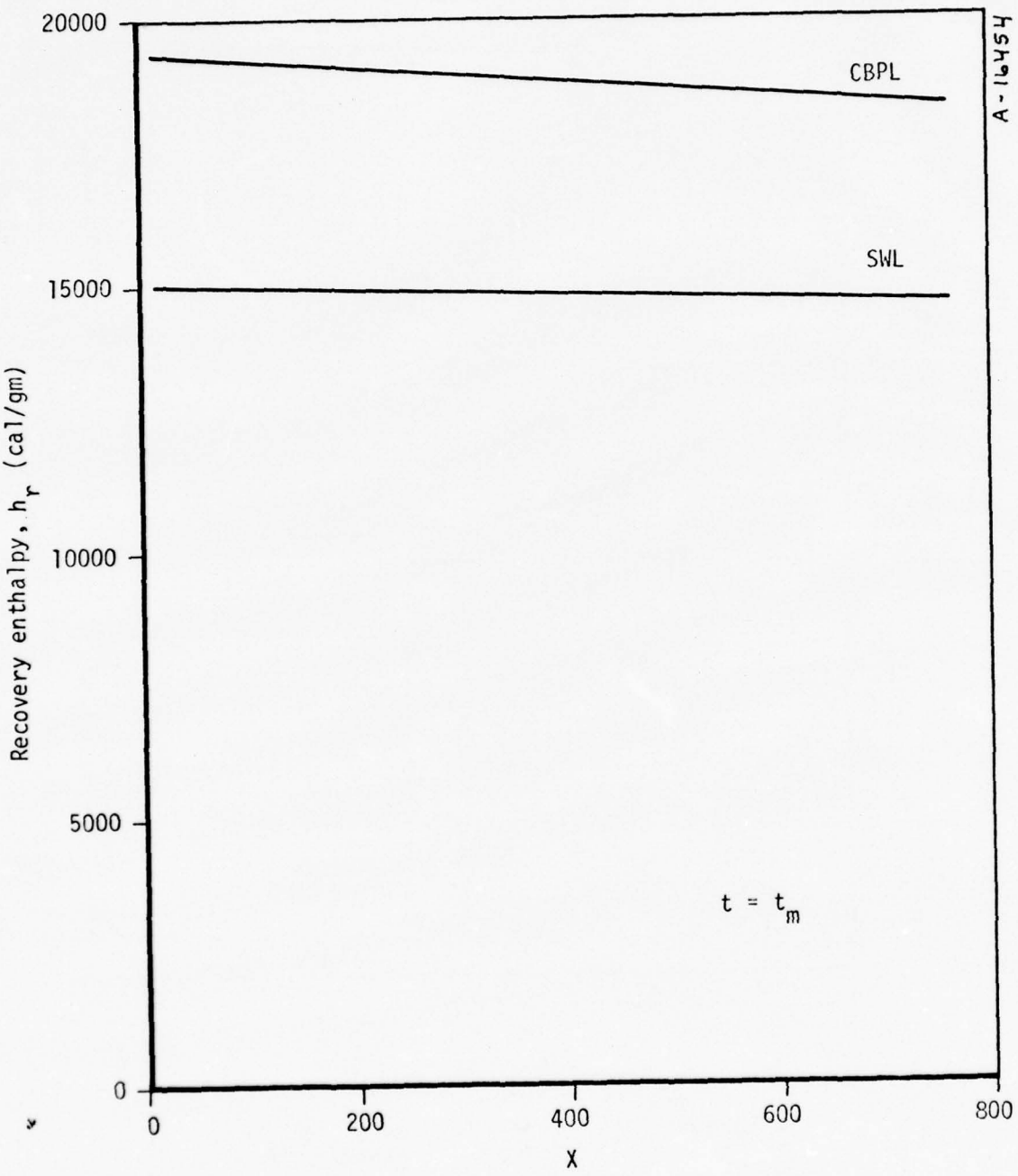

Figure 29b. Axial distribution of recovery enthalpy at the time of projectile expulsion.

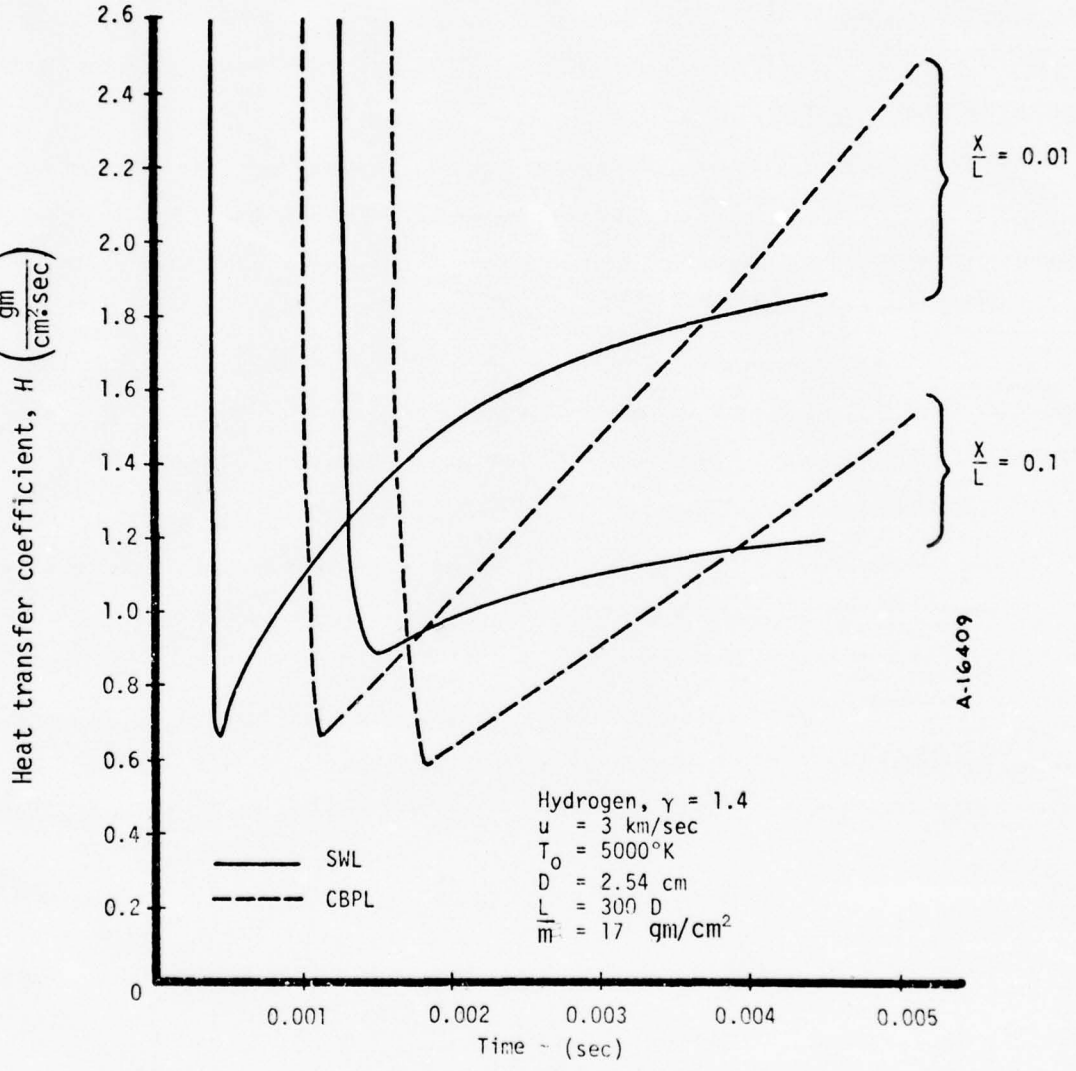

Figure 30a. Time histories of heat transfer coefficient.

It is somewhat surprising that the average transfer coefficients between the time of projectile passage and the time the projectile leaves the barrel are about the same for both idealized cycles. The lengths of the heating pulses are also approximately the same between cycles. However, considering the time histories of local recovery enthalpy shown in Figure 30(b) (the differences in recovery enthalpy between the CBPL and SWL increase with muzzle velocity), important differences in heat transfer exist late in the propulsion cycle.

The time variations of heat transfer rates (based on a constant barrel temperature of 1,000°K*) over the internal surfaces (i.e., integral of heat fluxes over the exposed surface) are shown in Figure 31. The principal cause for the rate increase with time is the increase in exposed surface area with time rather than heat flux.

Note that these predicted heat transfer rates are conservatively high after boundary layer closure. This is primarily because heat loss from the gas causes a reduction of heat transfer driving potential after closure. (The curve labeled "Reference" in Figure 31 addresses this consideration, and will be discussed later.)

Total heat loads (time integrals of rates in Figure 31) for representative conditions are presented in Figure 32. These loads are on the order of the projectile kinetic energies at the muzzle (kinetic energy = 3.7×10^5 calories for M_p = 86 gm, u = 6 km/sec). Consequently, it is clear that they need to be considered in terms of ballistic performance.

The heat load in Figure 32 for the CBPL is 80 percent larger than that of the SWL at 6 km/sec. The heat loads for the two cycles approach each other at lower velocities, which is to be expected (based on equivalence of the cycles at low u_m^*).

Two approaches have been employed to estimate the effects of heat transfer. In the first approach, total heat removal ideally takes place in the chamber prior to projectile motion. Based on early results, heat losses for this analysis have been approximated by the following relationship:

$$Q(\text{cal}) = 3.02 \times 10^4 \left(u_m \frac{\text{km}}{\text{sec}}\right)^{1.34} \tag{33}$$

Results of evaluating Equation (33) are slightly higher than those for the SWL, as shown in Figure 32.

In the calculation, the reservoir state after the heat loss is

$$E_{R,Q} = E_{R,Q=o} - Q \tag{34}$$

*Obviously, heat losses will be lower for higher barrel temperatures.

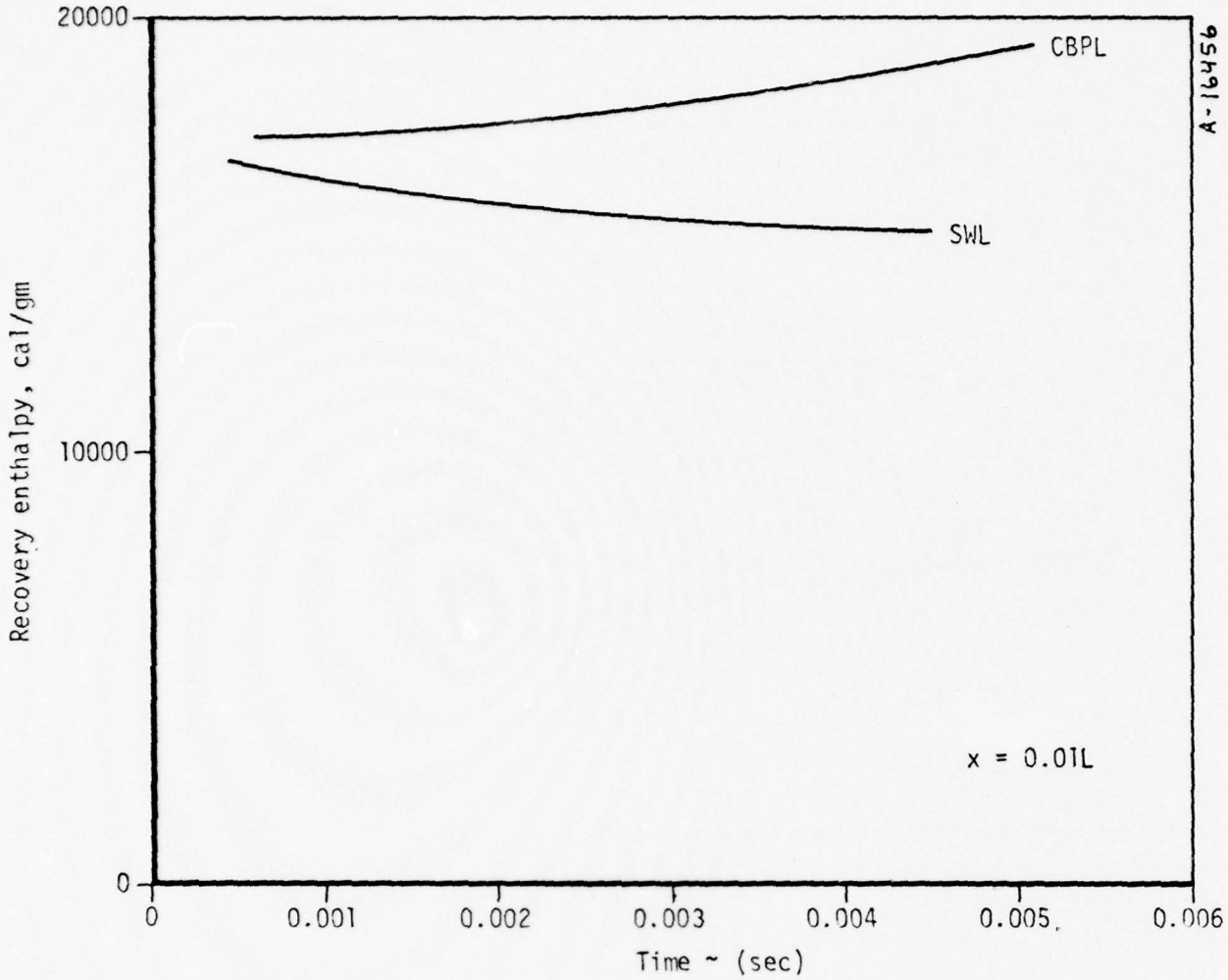

Figure 30b. Time histories of recovery enthalpy.

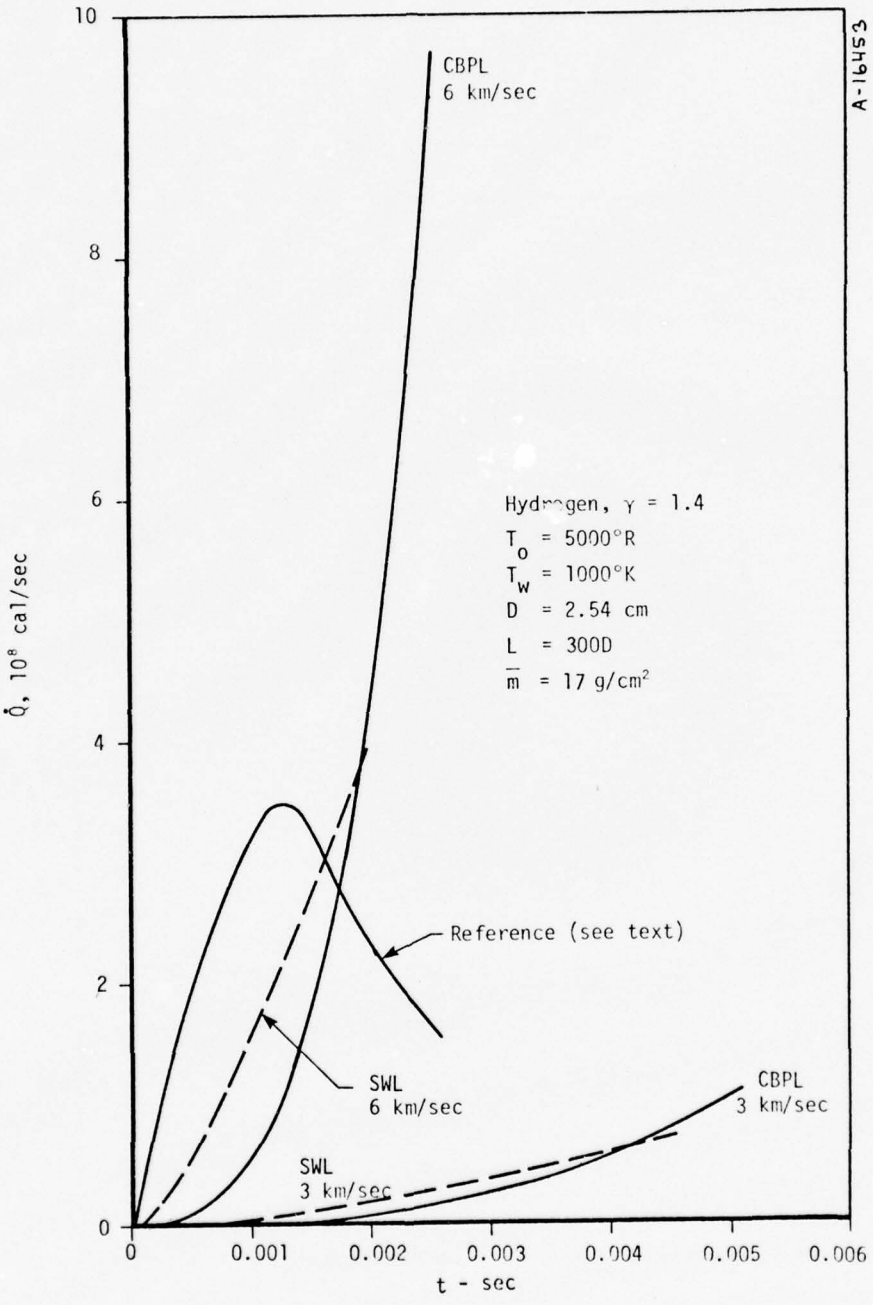

Figure 31. Time histories of total barrel heat transfer rates.

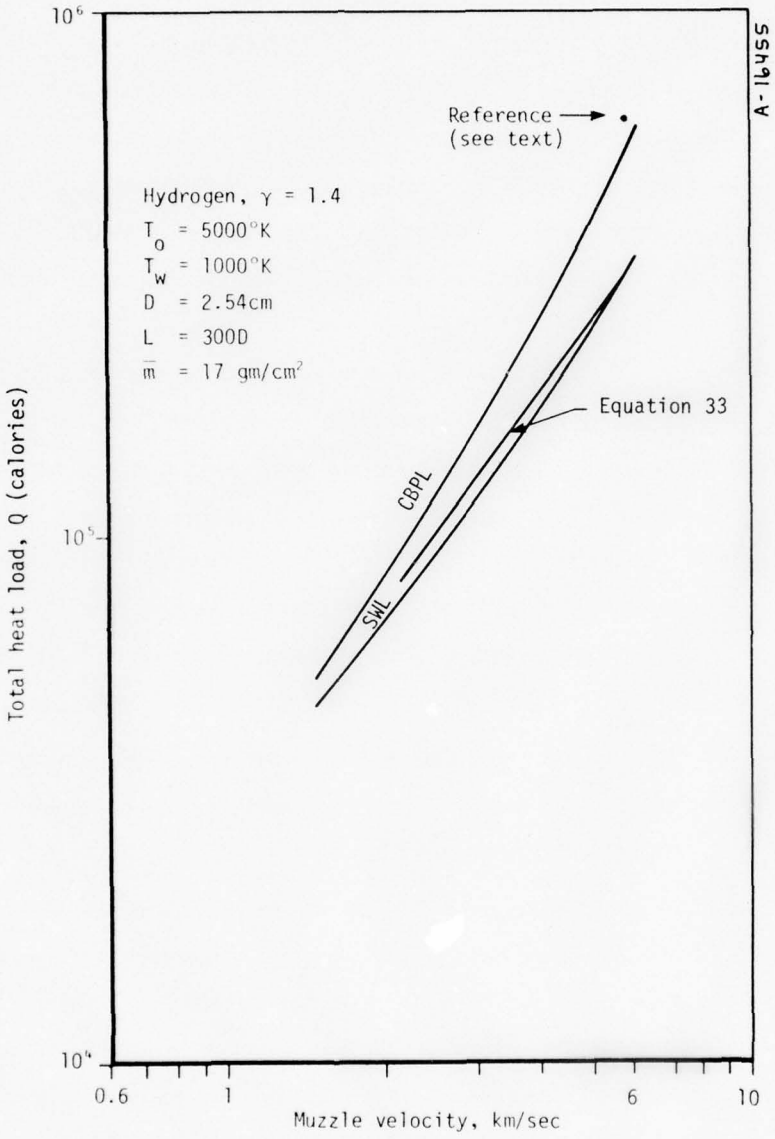

Figure 32. Influence of type of ballistic cycle and muzzle velocity on total heat load to the barrel.

and the modified reservoir parameters are computed as in Section 3 for dissociated hydrogen, including covolume effects. Subsequently, to obtain the estimated performance with heat transfer, ideal performances have been calculated using the Seigel curves. The results are presented in Table 6 where it is seen that the maximum effect is a reduction of less than 9 percent in muzzle velocity.

In an attempt to distribute the heat load during the ballistic cycle in a more representative manner, another idealized cycle was calculated with heat transfer directly coupled into the expansion process. In this technique, nonsteady flow effects are ignored in favor of assuming uniform spatial distribution of density, pressure, and temperature. In addition, convection from the gas is evaluated by applying a fully developed turbulent pipe flow heat transfer relationship. The analytical technique is developed in Reference 11 for application to a low speed pneumatic propulsion concept. Without heat transfer, this analysis yields higher muzzle velocities than that obtained using the Seigel curves.

The condition considered for application of this technique is Case No. 3 of Table 6 (this is also Case No. 7 of Tables 3 and 4). In the calculation, system volumes and masses are the same as in Table 6. However, the method of Reference 11 considers chamber and barrel cross sections to be the same (this requires a very long chamber for the present calculation), and evaluates heat transfer in the chamber as well as in the barrel. Because of the low velocities in the actual compressor section, chamber heat losses are expected to be relatively small compared to losses in the barrel. This consideration (in addition to the expected minimum ballistic effects of heat transfer before closure) suggests that the estimated heat loss effects on ballistics will be conservatively high.

The evaluation is based on a perfect-ideal gas which has been represented by choosing a suitable fictitious molecular weight. The choice was based on matching the isentropic exponent, chamber density, chamber volume, pressure, and temperature of Table 6.

The time history of heat transfer rates from this evaluation is presented as the curve labeled "Reference" in Figure 31. The rates are very much higher than the former data in Figure 31 during the early portion of the cycle due to the computed convection within the chamber; later, the rates decrease due to the loss of energy from the gas. The history of the heat losses for the CBPL and SWL are considerably more accurate, at least prior to the times of boundary layer closure. The total heat load is shown in Figure 32 for the computed ideal velocity of 5.5 km/sec (computed from the method of Reference 11). This heat load is approximately 30 percent higher than for the CBPL at the same muzzle velocity.

The result in Table 6 shows an ideal muzzle velocity approximately 13 percent lower than that computed by the method, shown in Figure 33. The computed velocity degradation due to heat transfer is approximately 16 percent. Also, the computed pressure and temperature at the time of projectile exit are significantly influenced by heat transfer, as shown in Table 7.

TABLE 6. COMPARISON OF SELECTED BALLISTIC CALCULATIONS WITH AND WITHOUT HEAT LOSS FROM RESERVOIR AFTER COMPRESSION AND PISTON STOP

Driver			Compressor			Reservoir								Launch Cycle		
Case No.	Initial Pressure (psi)	Shock Pressure (Kilobars)	Piston Weight (gms)	Piston Velocity (km/sec)	Initial Pressure (psi)	Heat Loss (e.u)	Total Gas Energy (e.u)[a]	P_R (Kilobars)	T_R (°K)	ρ_R (gm/cm^3)	α_R (%)	γ_{isent}	C_R (km/sec)	G/M_p	M_p (gms)	u_p (km/sec)
1	350	0.974	2724	0.9144	350	0.0	38.00	2.98	3715	0.0159	1.0	1.52	5.34	0.96	86	3.70
	350	0.974	2724	0.9144	350	7.31	30.69	2.53	3167	0.0159	0	1.54	4.95	0.96	86	3.40
2	350	0.974	2724	0.9144	3.7	0.0	37.26	2.94	4785	0.0124	5-1/2	1.37	5.69	0.62	86	3.80
	350	0.974	2724	0.9144	3.7	7.57	29.69	2.54	4190	0.0124	2-1/2	1.41	5.35	0.62	86	3.52
3	700	1.99	4540	0.9144	3.7	0.0	72.32	5.05	4803	0.0196	4-1/2	1.50	6.21	1.23	86	4.81
	700	1.99	4540	0.9144	3.7	10.38	61.94	4.58	4372	0.0196	2-1/2	1.53	5.47	1.23	86	4.57
4	700	1.99	4540	1.2192	3.7	0.0	86.00	10.47	5425	0.0308	6-1/2	1.71	7.63	1.23	86	6.12
	700	1.99	4540	1.2192	3.7	13.95	72.05	9.46	4880	0.0308	4	1.78	7.39	1.23	86	5.70

[a] 1 e.u. ≈ 23,900 calories

T 1 15

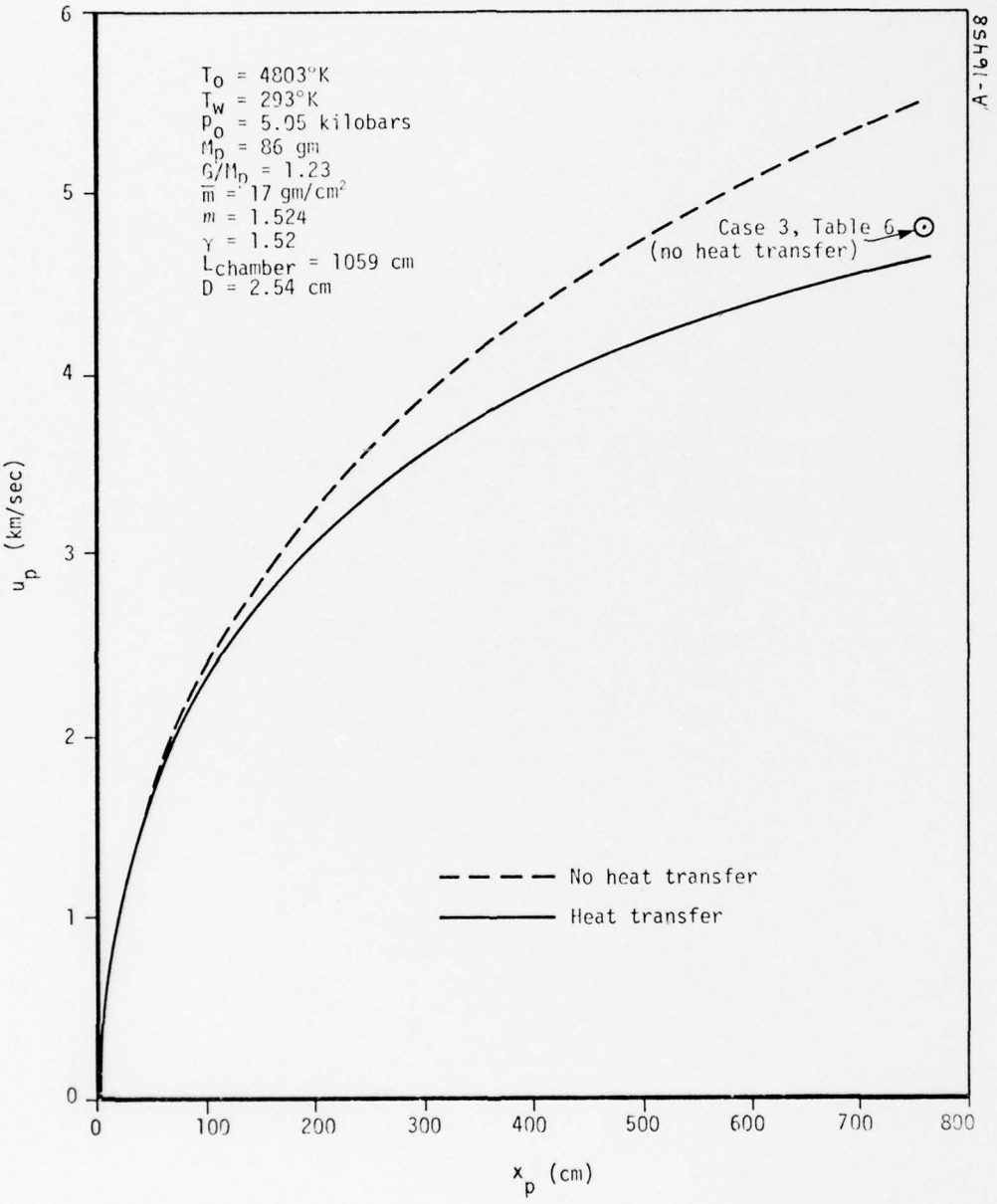

Figure 33. Effect of heat transfer on projectile velocity, method of Reference 11.

TABLE 7. ESTIMATED EFFECTS OF HEAT TRANSFER ON FINAL GAS PRESSURE AND TEMPERATURE (DATA OF FIGURE 33)

	T (°K)	p (kilobars)
No heat transfer	3,623	0.98
Heat transfer	1,602	0.43

If the calculation is extended to greater barrel lengths, projectile velocity will still increase. However, the rate of increase is quite diminished at an L/D of 300.

Based on all these estimates, it is concluded that the heat losses in the PI launcher are not a major cause for performance shortfall, if performance is judged at projectile travels of less than about 300 diameters (a shortfall of approximately 10 percent is to be expected here). If the design requires additional L/D to get performance (based on ideal calculations), the expected results will not be achieved. In the PI tests, maximum projectile velocities were achieved at less than 430* diameters for Test 8, which is not surprising. Muzzle velocity in Test 7 was achieved in about 200 diameters.

*More projectile position data would have been useful here.

SECTION 5

MATERIAL RESPONSE TO HEAT TRANSFER

Heat transfer rates to the barrel are extremely high for the muzzle velocities, projectile areal densities, and the gas enthalpy levels of interest here. Examples of spatial and temporal distributions of heat transfer, as well as integrated heating loads have been presented in Section 4.4. In Section 5, various candidate barrel (or barrel insert) material responses to the heating encountered during specific ballistic cycles are discussed.

The evaluations of material response were performed using the one dimensional "Aerotherm Charring Material Thermal Response and Ablation Program" (CMA). This code is described in Reference 12. Input to the CMA code include pressure and recovery enthalpy (approximated by the total enthalpy) histories from the ballistic cycle, and the heat transfer coefficient distribution from the boundary layer calculations. This code uses real gas thermochemistry (in this case, for hydrogen) generated with the "Aerotherm Chemical Equilibrium" (ACE, Reference 13) code, to determine the wall enthalpy, h_w, as a function of wall temperature and pressure. Thus, the heat flux which is a boundary condition on the conduction problem depends upon its solution through the wall temperature. The transient internal conduction computation uses a numerical finite difference procedure.

The results of Subsection 4.4.2 suggest that heat losses to the barrel do not have a large impact on ballistic performance. Accordingly, the heat transfer problem in the launcher is not a problem of containing the heat, but rather one of handling the heat transfer with minimum damage to launcher components.

The heat transfer can be handled in at least three ways by:

- Selecting a barrel or barrel liner material with properties such that it does not reach failure temperature before completion of the ballistic event. This approach makes use of the heat sink capabilities of the material
- Actively cooling the material below failure temperature (e.g., transpiration cooling)
- Allowing the material to fail (or ablate), and replacing it as required

The best approach is the application of heat sink materials, since they are passive and (ostensibly) will not need to be replaced. Active cooling may be costly and complex, and if used, should be designed to cool to just below the material fail temperature to minimize system convective heat losses. Ablative liners would recede intentionally in a controlled manner and perhaps would survive several launch cycles. This effort has concentrated on evaluating the feasibility of heat sink materials; the only failure mechanism considered was melting.

The relative performance potential for candidate materials can be predicted using the results of transient conduction in a constant property semi-infinite slab subjected to constant heat flux (see for example, Reference 14). For this case the time to melt is

$$t_m \sim \frac{\Delta T^2}{\dot{q}^2} k\rho c \tag{35}$$

where $\Delta T = T_{melt} - T_{initial}$

k = thermal conductivity

c = specific heat

Among structural metals, tungsten has the longest time to melt for a given heat flux, because of its extremely high melting point. On the other hand, steel is inexpensive and strong, and copper has a high thermal conductivity. Relative to tungsten, these materials have melting times (at constant heat flux) of

$$t_{m,\ steel} \approx \frac{1}{15} t_{m,w}$$

and

$$t_{m,\ copper} \approx \frac{1}{4} t_{m,w}$$

In the present case, an additional benefit can be expected from high melt temperatures through the reduction of the heat flux potential, $h_r - h_w$. The results presented below demonstrate that this reduction is an important consideration.

It has been found that even the least severe heating environment can be expected to melt ordinary heat sink materials. Material comparisons were made from thermal response predictions computed for the 3 km/sec CBPL heat transfer coefficient and recovery enthalpy histories shown in Figure 30, together with the appropriate pressure histories. These results are shown in Figure 34.

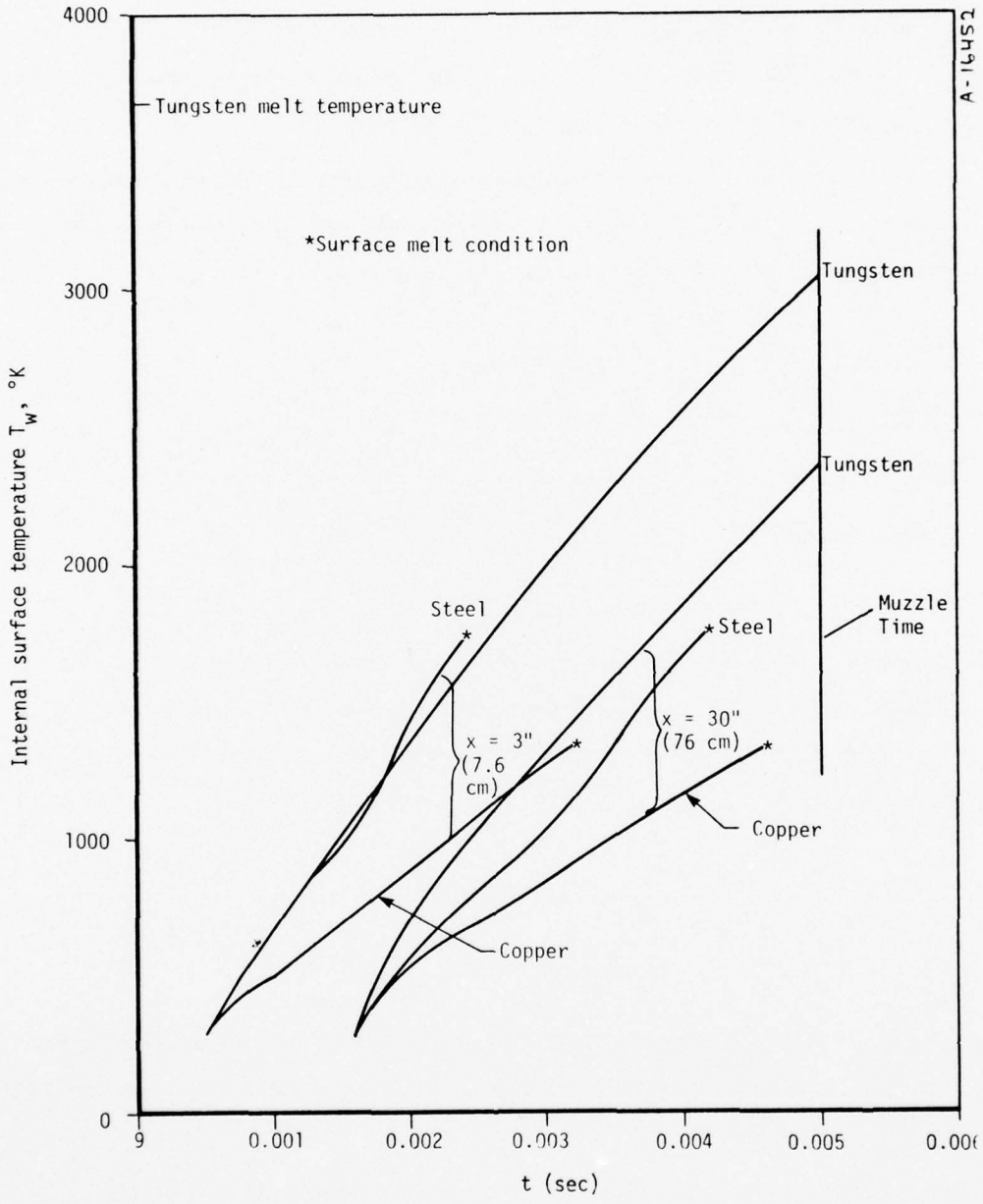

Figure 34. Thermal response of three barrel surface materials to convection near the chambrage plane. CBPL, conditions of Figure 30 (i.e., 3 km/sec, p_o = 1000 atm).

Relative thermal performances (Figure 34) are approximately as expected. These predictions are supported by the fact that melting of steel occured in the PI launcher at the indicated muzzle velocity.* Steel and copper were judged to be inadequate heat sink materials for the desired application (6 km/sec), and predictions at high muzzle velocities were restricted to tungsten.

Tungsten thermal response predictions were performed for a 6 km/sec muzzle velocity at two locations in a 2.54 cm diameter launcher operating either as a CBPL or as a SWL. The heat transfer coefficient histories are similar in shape to those shown in Figure 30, but have a magnitude 5 or 6 times as large. The thermal response predictions, which are displayed in Figure 35, indicate that tungsten will melt in a CBPL at these conditions, but will not melt in a SWL. The reason for the vast difference between the predictions for the two cycles is apparent from the total enthalpy distributions shown in Figure 36.

The total enthalpy is defined (for a perfect gas) as

$$h = C_p T + U^2/2$$

C_p = specific heat at constant pressure

At the time the projectile leaves the muzzle, the velocity at the chambrage plane is 6 km/sec in the CBPL and only 3.5 km/sec in the SWL. Also, the local recovery temperature increases in a CBPL and decreases in a SWL. The net result is that, at muzzle time, the ratio of total enthalpies for the two cycles is about 1.8. Since the enthalpy of hydrogen at the melting temperature of tungsten is almost as large as the SWL total enthalpy, the differences in total enthalpy between the two cycles has a drastic effect on heat transfer. This effect would be decreased for higher initial chamber temperature and magnified for lower temperatures.

Although the SWL results appear encouraging from a material protection point of view, it must be kept in mind that base pressures are prohibitively high at early times in this mode of operation. Figure 37 describes the pressure histories at the chambrage plane (p_R) and on the projectile base (p_p) required to achieve the projectile muzzle velocity of 6 km/sec for this example. The CBPL provides the best ballistic performance for a given base pressure, but has prohibitively high heat transfer rates. Thus, it is apparent that alterations to a given cycle which tend to solve one of

*No calculations were performed for this case for a SWL. Since SWL heat transfer rates are lower near the end of the cycle, it is probable that both copper and steel would survive for this example at x = 30 inches (76.2 cm), but neither would survive at x = 3 inches (7.62 cm).

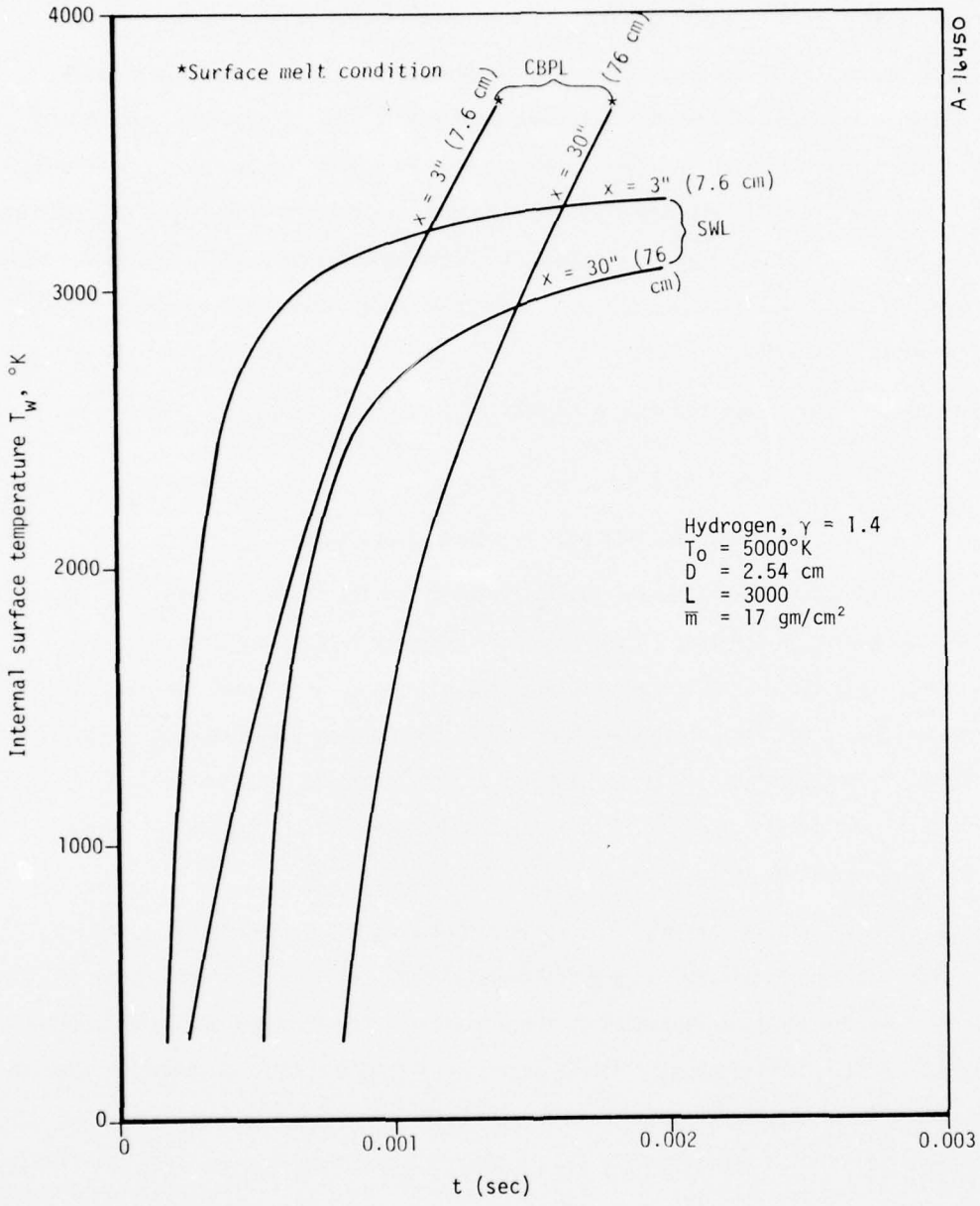

Figure 35. Tungsten thermal response at two locations near the chambrage plane, CBPL and SWL cycles.

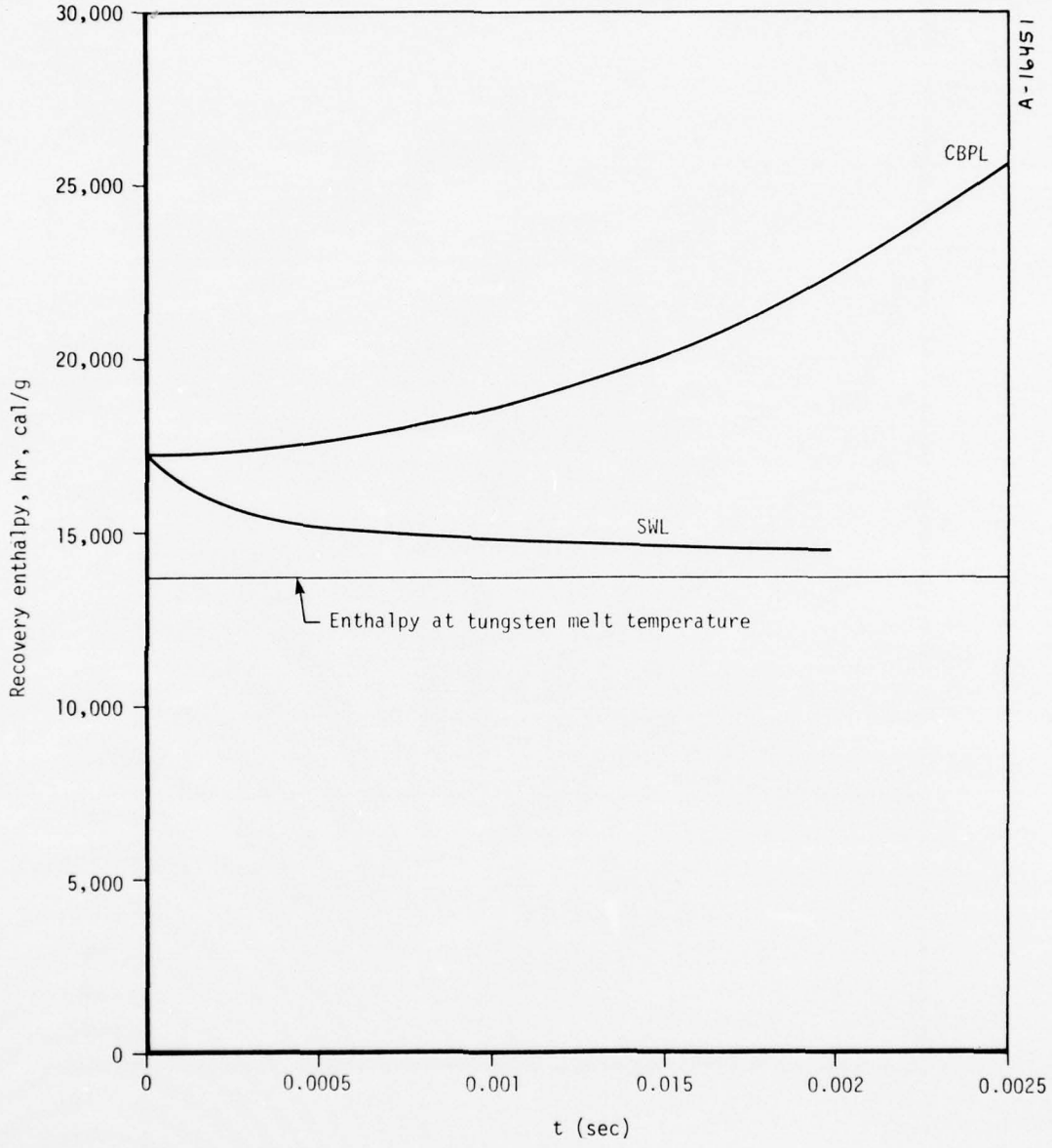

Figure 36. Stagnation enthalpy history input to calculation of Figure 35.

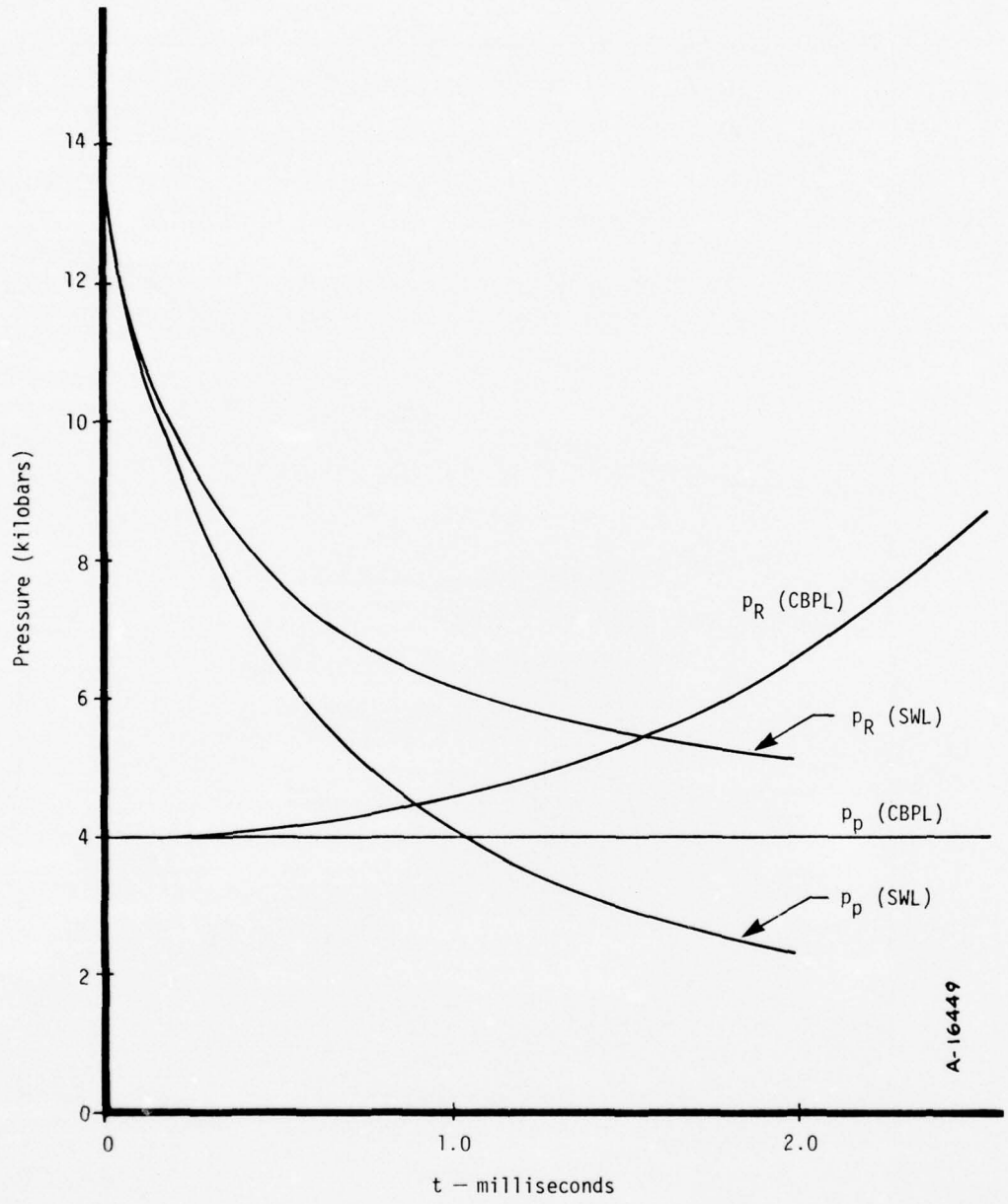

Figure 37. Pressure histories associated with an 86 gram projectile muzzle velocity of 6 km/sec, 762 cm barrel length.

these problems will only tend to aggravate the other. However, a compromise may be feasible, depending on the degree of control of compressor piston motion. The desired motion will achieve near constant base pressure until midway in cycle, and reduced base pressure thereafter in the manner of a SWL to limit recovery enthalpies and heat transfer coefficients.

It may be that a compromise between high muzzle velocity at limited base pressure and limited heat transfer cannot be found which will allow heat sink absorption of the energy without melting. Thermal protection using a subliming ablator (for example, carbon) may be feasible and should be carefully considered in any future design of high performance light gas launchers. The necessary evaluation is beyond the scope of the present work.

SECTION 6

RECOMMENDATIONS

Aerotherm recommends that the hybrid launcher be redesigned to achieve the desired ballistic performance. The redesign must address the following:

- *Hydrogen is the best choice for the working medium.* Within the operating range of the hybrid launcher (1 to 10 kilobars and 1,000 to 6,000 degrees, Kelvin), it is imperative to account for molecular covolume, vibrational excitation, and dissociation.
- Explosive drivers should be designed to operate without jetting or leaking
- The configuration must be such that complete driver gas injection is realized. It may be necessary to use an entirely different configuration.
- The transition section between the compressor chamber and the barrel should conform to a proven nozzle design to reduce heat loads and choking
- The barrel length must be sized to account for momentum losses to the boundary layer (i.e., barrel lengths beyond 400 diameters should be avoided)
- The piston motion must be tailored to achieve a compromise between optimum projectile acceleration and tolerable heat loads (e.g., a CBPL operation for high projectile acceleration until midway in the cycle, and thereafter SWL operation with decreasing base pressure to limit heat loads on materials)
- The steel barrel (and possibly the steel compressor) must be protected from expected heat loads; in conjunction with a tailored piston motion, liner/inserts made of tungsten (or possibly an ablative material such as carbon) should be evaluated for response to heat loads

LIST OF REFERENCES

1. Seifert, K., "Hypervelocity Launcher Design," PIFR-708, Final (Draft) Report prepared for DNA by Physics International Company, December 1975.

2. Seigel, A. E., "The Theory of High Speed Guns," AGARDograph 91, prepared by North Atlantic Treaty Organization Advisory Group for Aerospace Research and Development, May 1965.

3. Bjork, R. L. "The Atomic Hydrogen Gun," Report RM-1707, prepared by Rand Corporation, 1961.

4. Glass, I. I., "Hypervelocity Launchers," Review No. 22, prepared by University of Toronto Institute for Aerospace Studies, January 1963.

5. Watson, J. D., "High-Velocity Explosively Driven Guns," NASA CR-1533, prepared by Physics International Company, June 1970.

6. Liepmann, H. W. and Roshko, A., "Elements of Gasdynamics," John Wiley & Sons, Inc., New York, 1957.

7. Dahm, T. J. and Anderson, L. W., "Propellant Gas Convective Heat Transfer in Gun Barrels," Aerotherm Final Report No. 70-18, August 1970.

8. Anderson, A. D. and Dahm, T. J., "Barrel Boundary Layer Effects Associated with Idealized Projectile Launchers," to be submitted for publication.

9. Dahm, T. J., Cooper, L., Rafinejad, D., Youngblood, S. B and Kelly, J. T., "Inviscid Flow and Heat Transfer Modeling for Reentry Vehicle Nosetips," Aerotherm Final Report No. 76-224, October 1976.

10. Dahm, T. J., personal communication with Mr. Gary Wallace of Acurex Corporation, January 1977.

11. Dahm, T. J., "Analytical and Experimental Behavior of GVT Propulsion, and Computed System Performance Characteristics," Aerotherm Corporation, Final Report No. 68-56, September 1969.

12. Wool, M. R., "User's Manual Aerotherm Charring Material Thermal Response and Ablation Program, Version 3," Aerotherm Report Number UM-70-14 prepared for Air Force Rocket Propulsion Laboratory, April 1970.

13. Powars, C. A. and Kendall, R. M., "User's Manual Aerotherm Chemical Equilibrium (ACE) Computer Program," Aerotherm Report Number UM-69-7, May 1969.

14. Carslaw, H. S. and Jaeger, J. C., "Conduction of Heat in Solids," 2nd Edition, Clarendon Press, Oxford 1959.

APPENDIX A

EQUATION OF STATE FOR HYDROGEN

In a pressure range of 1 kb to 15 kb and a temperature of less than 7,000°K, hydrogen is a reasonably dense gas that is essentially diatomic with some dissociation. Under these conditions, this gas is characterized as a Van der Waals medium which is subject to the effects of molecular attraction and covolume, and influenced by vibrational excitation, dissociation, and ground state electronic excitation.

Accordingly, the equation of state is:

$$p = \rho RT \left\{ 2\alpha+(1-\alpha) \left[\frac{1}{1-(1-\alpha)\rho b} - \frac{a(1-\alpha)\rho}{RT} \right] \right\} \qquad \text{(A-1)}$$

which incorporates the law of partial pressures for hydrogen dissociation:

$$H_2 \rightleftarrows 2H$$

The terms in Equation (A-1) are:

T = Temperature

α = degree of dissociation

a = intermolecular attraction parameter

b = molecular covolume parameter

R = gas constant per gram for molecular hydrogen

In terms of the liquid-vapor critical point for molecular hydrogen:

$$a = \frac{27}{64} \quad \frac{R^2 T_c^{\,2}}{P_c} \quad ; \; b = \frac{V_c}{3}$$

where V_c is the experimentally determined critical volume

= 34.57 cm^3/gm (Reference A-1)

T_c = 33.2°K

p_c = 12.98 x 10^{-3} kb

R = 4.12475 x 10^{-2} $\frac{kb \cdot cm^3}{gm \cdot °K}$ for molecular hydrogen

The degree of dissociation of the gas is derived by considering the gas in equilibrium with Gibbs free energy at a minimum (Reference A-2).

$$\frac{\alpha^2}{1-\alpha} = \frac{\exp(-\theta_d/T)}{\rho}\left[0.0392\sqrt{T}\left\{1-\exp(-\theta_v/T)\right\}\right] \qquad \text{(A-2)}$$

where T = Temperature

θ_d = characteristic dissociational temperature = 51,965°K

θ_v = characteristic vibrational temperature = 6,324°K

The constant "0.0392" is evaluated from fundamental constants

$$M_H\left(\frac{M_H K}{h^2}\right)^{3/2}\theta_R\,\frac{\left(g_o^H\right)^2}{g_o^{H_2}}$$

where M_H = mass of hydrogen atom = 1.67×10^{-24} gm

k = Boltzmann constant = 1.38×10^{-16} erg/°K

h = Plancks constant = 6.625×10^{-27} erg-sec

θ_R = characteristics rotational temperature = 87.5°K (Reference A-1)

g_o^H = ground state electronic partition function for H-atom = 2

$g_0^H 2$ = ground state electronic partition function for H_2-molecule = 1

The internal energy per gram of hydrogen is given by:

$$e = \alpha R\theta_d + RT\left[3\alpha + (1-\alpha)\left\{5/2 + \frac{Z}{\exp Z - 1} - \frac{a(1-\alpha)\rho}{RT}\right\}\right] \qquad \text{(A-3)}$$

where $Z = \theta_v/T$

The Helmholtz free energy per gram for hydrogen is given by:

$$f = -2\alpha RT\left\{\ln\left[\left(\frac{2\pi M_H k}{h^2}\right)^{3/2} 4M_H\right] + \ln\left[\frac{T^{3/2}}{2\alpha\rho}\right] + \frac{\theta_d}{2T} + 1\right\}$$

$$-(1-\alpha)\,RT\left\{\ln\left[\left(\frac{4\pi M_H k}{h^2}\right)^{3/2}\frac{M_H}{\theta_R}\right] + \ln\left[\frac{T^{5/2}\left\{1-(1-\alpha)\rho b\right\}}{(1-\alpha)\rho(1-\exp(-z))}\right] + \frac{a(1-\alpha)}{RT} + 1\right\} \qquad \text{(A-4)}$$

and is derived from $f = \Sigma\, n_i f_i$

where n_i - mass fraction

$f_i = -kT \left\{ \ell n \mathbb{P} + 1 \right\}$

$\mathbb{P}$ = partition function

Partition functions for translation, rotation, ground state electronic excitation, vibration, dissociation, covolume, and Van der Waals attraction are obtained from References (A-1 and A-2)

The entropy per gram of hydrogen is given by:

$$s = \frac{e-f}{T} \tag{A-5}$$

The sound speed, C and isentropic index, γ_{isent} are calculated numerically using (A-1), (A-2), and (A-5)

$$C = \left[\frac{\Delta P}{\Delta \rho} \right]^{1/2}_{\substack{\Delta S = 0 \\ \Delta T = 1°K}} \tag{A-6}$$

$$\gamma_{sent} = \frac{\rho}{p} \left[\frac{\Delta P}{\Delta \rho} \right]_{\substack{\Delta S = 0 \\ \Delta T = 1°K}} \tag{A-7}$$

Figures (A-1) through (A-5) depict the behavior of hydrogen as defined by Equations (A-1) through (A-7). Figure A-1 is a modified "Mollier" diagram of specific internal energy, e vs. scaled entropy, S/R for the range

$$2{,}000°K \leq T \leq 6{,}000°K$$

$$0.0005 \text{ gm/cm}^3 \leq \rho \leq 0.05 \text{ gm/cm}^3$$

The other figures display pressure, degree of dissociation, sound speed and isentropic index variations with density.

AD-A042 986 ACUREX CORP MOUNTAIN VIEW CALIF AEROTHERM DIV F/G 14/2
FEASIBILITY OF A HYBRID HYPERVELOCITY LAUNCHER.(U)
JAN 77 L M COHEN, T J DAHM, J D WATSON DNA001-76-C-0407
UNCLASSIFIED AEROTHERM-TR-77-238(7260) DNA-4226F NL

2 OF 2
AD
A042 986

END
DATE
FILMED
9-77
DDC

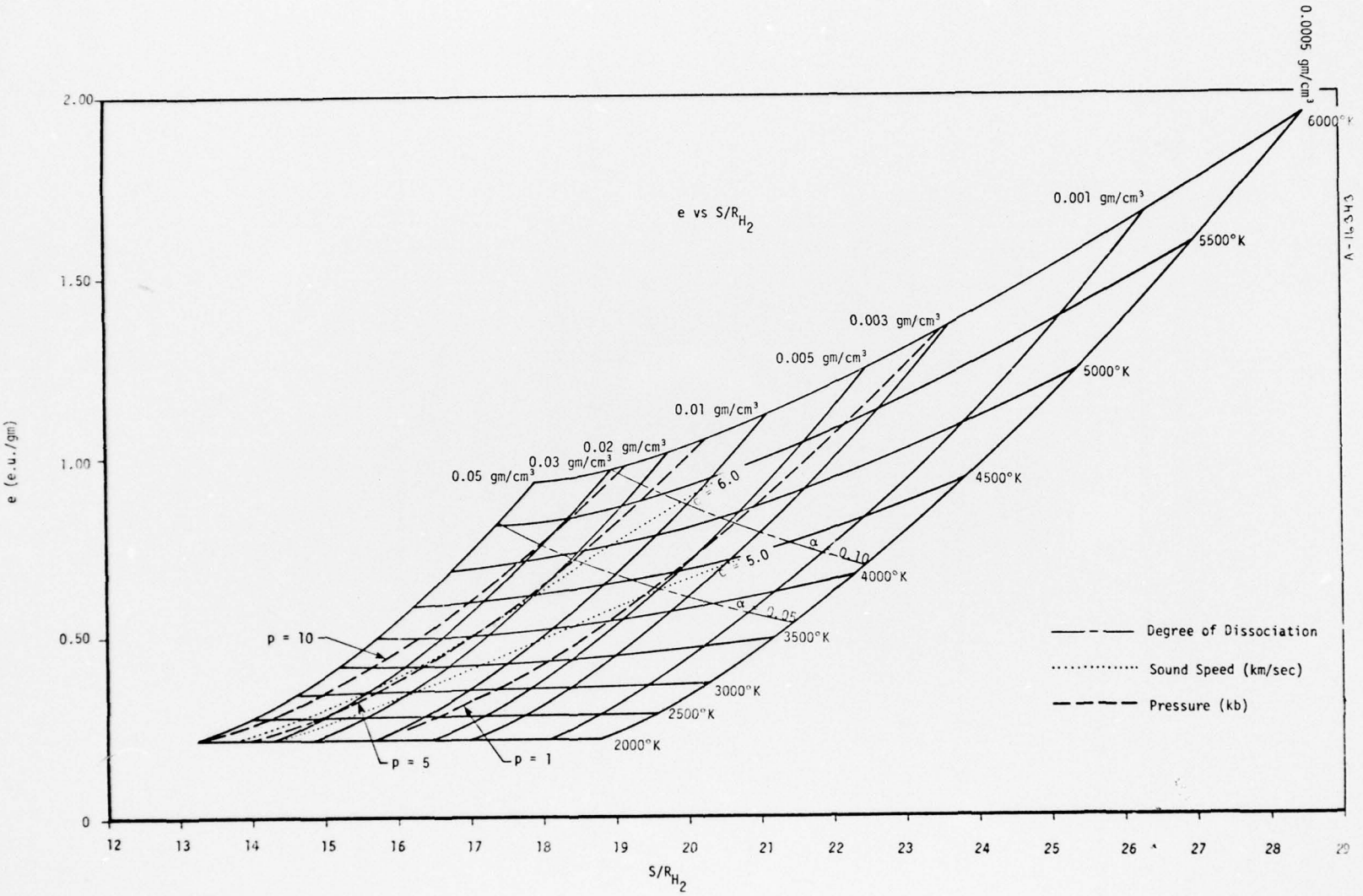

Figure A-1. Modified mollier diagram for hydrogen.

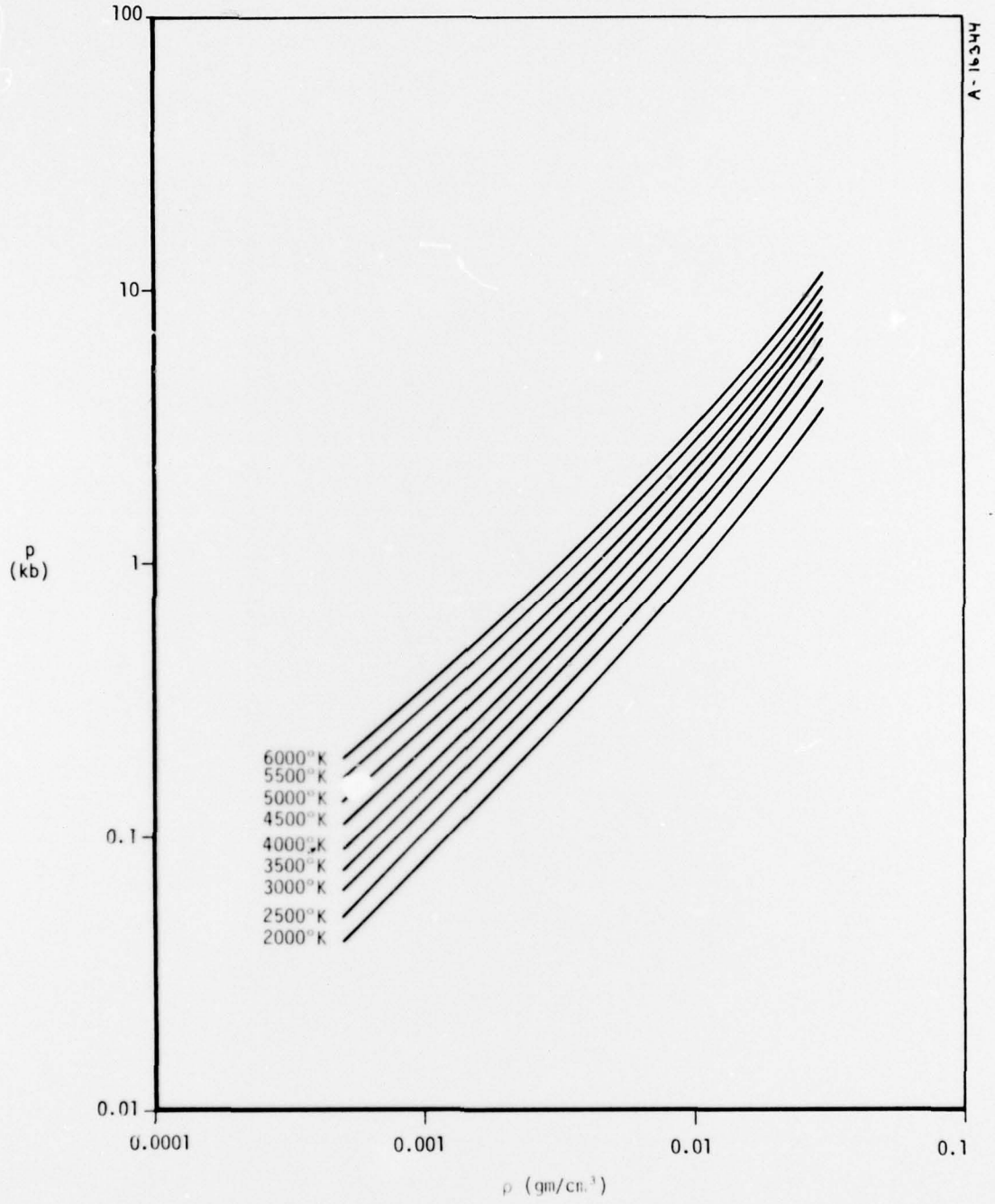

Figure A-2. Pressure dependence on density for hydrogen at various temperatures.

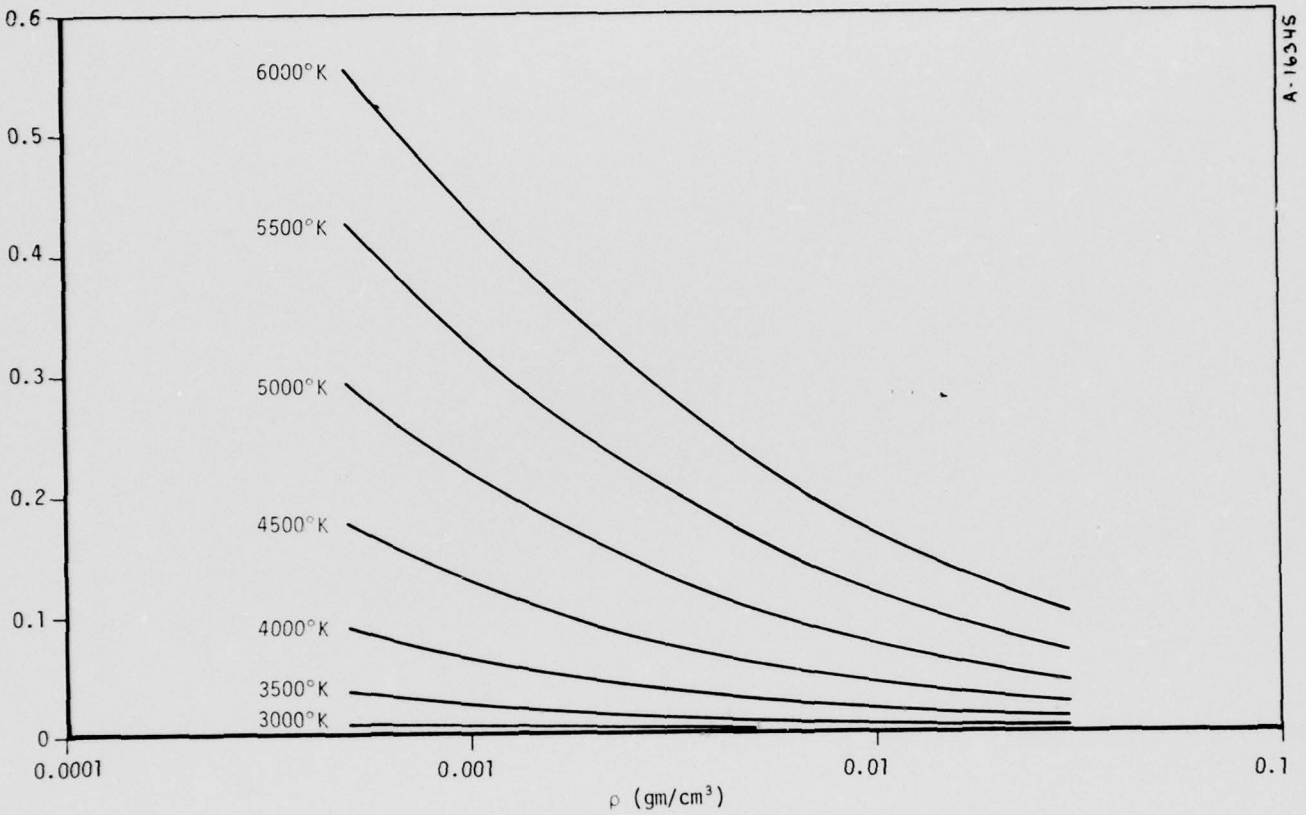

Figure A-3. Dissociation dependence on density for hydrogen at various temperatures.

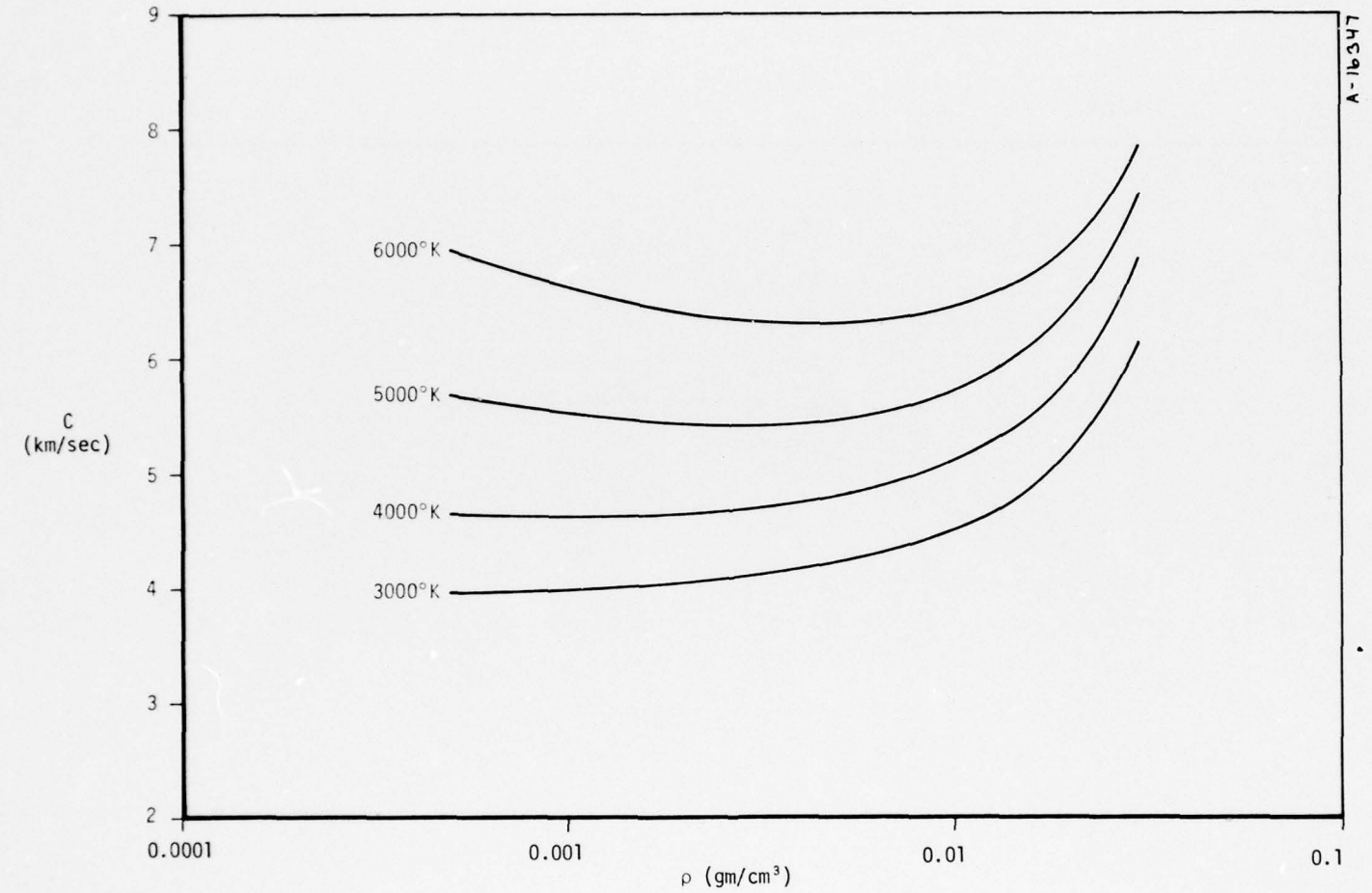

Figure A-4. Acoustic velocity dependence on density for hydrogen at various temperatures.

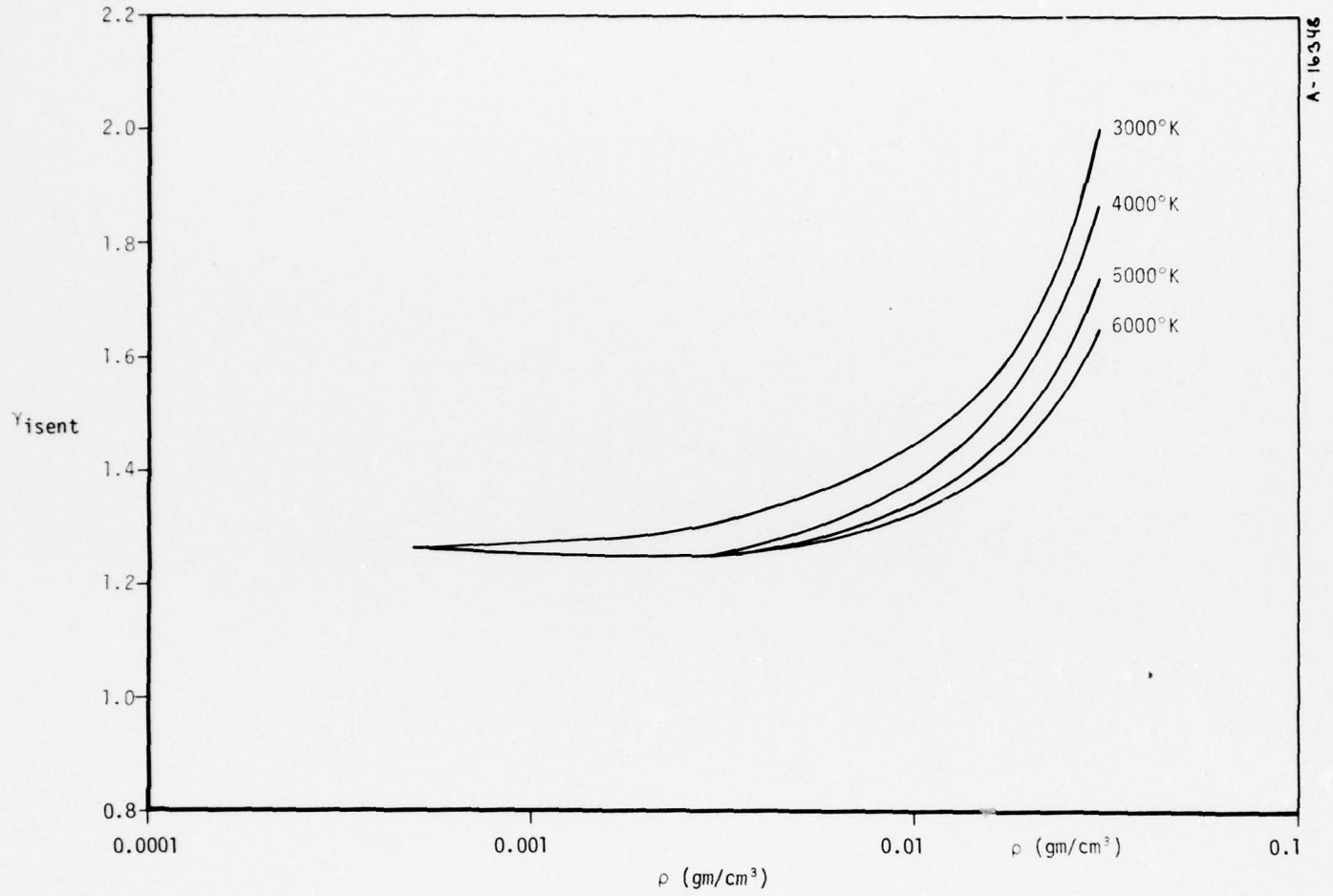

Figure A-5. Isentropic index dependence on density for hydrogen at various temperatures.

REFERENCES FOR APPENDIX A

A-1. Crawford, F. H., "Heat, Thermodynamics and Statistical Physics," Harcourt, Brace and World, Inc., New York, 1963.

A-2. Zel'dovich, Ya. B., and Razier, Yu. P., "Physics of Shock Waves and High-Temperature Hydrodynamic Phenomena," Vol. I and II, Academic Press, New York, 1966.

APPENDIX B

EXAMPLE OF CALCULATION PROCEDURE FOR HYBRID LAUNCHER BALLISTIC CYCLES

Using the methods described in Subsections 3.1 through 3.3, performance estimates can be made for various configurations and initial conditions of the PI launcher. For each estimate, ideal driver performance, complete injection, and an adiabatic reservoir are assumed. The launch tube length is assumed to be 300 bore diameters, a length consistent with experimental and theoretical work on maximum usable barrel lengths, as determined by boundary layer losses.

As an example, a performance estimate can be made using the initial conditions of PI Test 7. In this test both the drivers and compressor section were initially at 350 psia and 288°K and the mass of hydrogen in the system was 83 grams. The drivers are assumed to operate ideally, generating a shocked gas pressure of 0.97 kilobars. All of the gas is assumed to be injected into the compressor so that the injection state prior to compression is determined by its density, $\rho_3 = G/V_{inj} = 0.0067$ gms/cm^3 and internal energy, $e_3 = 0.329$ e.u./gm (1 e.u. = 10^{12} ergs). From Equations (A-1) to (A-5) the other state variables prior to compression are:

$p_3 = 0.8$ kb

$T_3 = 2{,}780°K$

$S/R = 17.25$

The 2,724 gm (6 lb) compressor piston is accelerated to 0.914 km/sec (3,000 fps) and has a total energy of 11.4 e.u. when it begins to compress the gas. The total energy of the gas upon injection is 27 e.u., so the energy contribution of the explosive drivers is substantial.

The piston isentropically compresses the gas, as it decelerates to rest 172 cm downstream of the injection ports (102 cm from the start of the transition section). The final compressed state (reservoir state) is characterized by its density $\rho_4 = 0.0159$ gm/cm^3 and entropy $S_4/R = S_3/R = 17.25$. The other reservoir state variables are calculated from (A-1) to (A-7), and are:

$p_4 = 2.98$ kb

$T_4 = 3{,}715°K$

$C_4 = 5.34$ km/sec

$\gamma_4 = 1.518$

$e_4 = 0.46$ e.u./gm

$\alpha_4 \sim 1\%$

The muzzle velocity is calculated for the following conditions:

$M_p = 86$ gms

$L = 300$ bore diameters $= 762$ cm

$A = \frac{\pi}{4} \times 2.54^2 = 5.07$ cm^3

$p_4 = 2.98$ kb

$\frac{C_4}{\gamma_4} = 3.52$ km/sec

$G/M_p = 83/86 \sim 1$

$D_{21} = 3$ (The Seigel curves for $D_{21} = 2$ and $D_{21} = 5$ are nearly identical, so either can be used)

$C_4' = 4.93$ km/sec for $\gamma_4' = 1.4$

The ballistic parameter, $\bar{x} = 0.55$, is used in Figure 6 for $G/M_p = 1$ and gives a dimensionless velocity $\bar{u} = 0.75$. Thus, estimated projectile velocity is $\bar{u}_p = \bar{u}C_4' = 3.70$ km/sec. This compares with PI's computed velocity of 3.65 km/sec (Reference 1) determined by the *PISCES code for the same* initial conditions.

The entire calculation can be repeated with the covolume forces suppressed to give the following reservoir conditions:

$p_4 = 2.89$ kb

$\rho_4 = 0.0187$ gm/cm^3

$T_4 = 3{,}715°K$

$\alpha_4 \sim 1\%$

$C_4 = 4.43$ km/sec

$\gamma_4 = 1.26$

$C_4/\gamma_4 = 3.5$ km/sec

It is interesting to note that p_4, T_4 and C_4/γ_4 are essentially unchanged, while ρ_4, C_4 and γ_4 are considerably different. Since p_4 and C_4/γ_4 are essentially unchanged, the calculated muzzle velocity of 3.67 km/sec with covolume forces suppressed is very close to that calculated with the full hydrogen equation of state, 3.70 km/sec.

DISTRIBUTION LIST

DEPARTMENT OF DEFENSE

Director
Defense Advanced Research Proj. Agency
ATTN: Strategic Tech. Office

Defense Documentation Center
12 cy ATTN: TC

Director
Defense Intelligence Agency
ATTN: DI-7D
ATTN: DT-1B
ATTN: DT-2, Weapons & Sys. Div.

Director
Defense Nuclear Agency
3 cy ATTN: SPAS
ATTN: STSI, Archives
3 cy ATTN: STTL, Tech. Library
ATTN: DDST
ATTN: STSP

Director of Defense Research & Engineering
Department of Defe
ATTN: S&S

Commander
Field Comma
Defense Nu ency
ATTN: FCPR

Director
Joint Strat. Target Planning Staff JCS
ATTN: JLTW-2
ATTN: JPTM

Chief
Livermore Division, Field Command, DNA
Lawrence Livermore Laboratory
ATTN: FCPRL

OJCS/J-5
ATTN: J-5 Plans & Policy Nuc. Div.

DEPARTMENT OF THE ARMY

Director
BMD Advanced Tech. Center
Huntsville Office
ATTN: ATC (Mel Capps)

Program Manager
BMD Program Office
ATTN: Technology Division

Dep. Chief of Staff for Research Dev. & Acq.
Department of the Army
ATTN: NCB Division

Deputy Chief of Staff for Ops. & Plans
Department of the Army
ATTN: Dir. of Chem. & Nuc. Ops.

DEPARTMENT OF THE ARMY (Continued)

Commander
Harry Diamond Laboratories
ATTN: DRXDO-RBH
ATTN: DRXDO-RC
ATTN: DRXDO-NP

Commander
US Army Missile Command
ATTN: DRSMI-XS, Chief Scientist

Commander
Picatinny Arsenal
ATTN: SMUPA-MD
ATTN: SARPA-ND-C-T

Director
US Army Ballistic Research Labs.
ATTN: Robert E. Eichelberger

Commander
US Army Mat. & Mechanics Research Center
ATTN: DRXMR-HH

Commander
US Army Materiel Dev. & Readiness Command
ATTN: DRCDE-D

Commander
US Army Nuclear Agency
ATTN: ATCA-NAW

Commander
BMD System Command
ATTN: BMDSC-TEB, R. Simpson

DEPARTMENT OF THE NAVY

Chief of Naval Operations
Navy Department
ATTN: OP 604C4

Director
Naval Research Laboratory
ATTN: Code 2600, Tech. Lib.

Commander
Naval Sea Systems Command
Navy Department
ATTN: Code 0351

Commander
Naval Surface Weapons Center
ATTN: Code 323

Director
Strategic Systems Project Office
Navy Department
ATTN: NSP-272
ATTN: Fred Wimberly

DEPARTMENT OF THE AIR FORCE

Commandant
AF Flight Dynamics Laboratory, AFSC
ATTN: FXG

DEPARTMENT OF THE AIR FORCE (Continued)

AF Geophysics Laboratory, AFSC
ATTN: Chan Touart

AF Materials Laboratory, AFSC
ATTN: LTM
ATTN: MBC

AF Rocket Propulsion Laboratory, AFSC
ATTN: RTSN

AF Weapons Laboratory, AFSC
ATTN: DYV
ATTN: SUL
ATTN: Dr. Minge

Headquarters
Air Force Systems Command
ATTN: F. Celec

Commander
Arnold Engineering Development Center
ATTN: XOA

Commander
Foreign Technology Division, AFSC
ATTN: PDBG

Hq. USAF/RD
ATTN: RDQ
2 cy ATTN: RDQSM

SAMSO/DY
ATTN: DYS

SAMSO/MN
ATTN: MNNR

SAMSO/RS
ATTN: RSSE
ATTN: RST
ATTN: RSS

Commander In Chief
Strategic Air Command
ATTN: NRI
ATTN: XOBM
ATTN: DOXT

ENERGY RESEARCH & DEVELOPMENT ADMINISTRATION

Division of Military Application
US Energy Research & Dev. Admin.
ATTN: Doc. Con. for Res. & Dev. Branch

University of California
Lawrence Livermore Laboratory
ATTN: G. Staihle, L-24
ATTN: Larry W. Woodruff, L-96
ATTN: C. Joseph Taylor, L-92
ATTN: Charles S. Godfrey

Los Alamos Scientific Laboratory
ATTN: Doc. Con. for J. W. Taylor
ATTN: Doc. Con. for John McQueen

ENERGY RESEARCH & DEVELOPMENT ADMINISTRATION (Continued)

Sandia Laboratories
Livermore Laboratory
ATTN: Doc. Control for C. S. Hoyle
ATTN: Doc. Control for T. Gold
ATTN: Raymond Ng

Sandia Laboratories
ATTN: Doc. Con. for Walter Herrmann
ATTN: Doc. Con. for A. W. Synder
ATTN: Doc. Con. for Albert Chabai
ATTN: Doc. Con. for D. McCloskey

DEPARTMENT OF DEFENSE CONTRACTORS

Acurex Corporation
ATTN: J. Courtney
2 cy ATTN: J. Huntington
ATTN: J. D. Watson
ATTN: T. J. Dahm
ATTN: A. D. Anderson
ATTN: L. M. Cohen

Aeronautical Research Assoc. of Princeton, Inc.
ATTN: Coleman Donaldson

Aerospace Corporation
ATTN: D. H. Platus
ATTN: W. Barry
ATTN: Robert L. Strickler
ATTN: Thomas D. Taylor
ATTN: R. H. Palmer
ATTN: D. T. Nowlan
ATTN: H. F. Dyner

ARO, Incorporated
ATTN: John C. Adams
ATTN: Glenn Norfleet

AVCO Research & Systems Group
ATTN: S. Skemp, J200
ATTN: John E. Stevens, J100
ATTN: George Weber

Battelle Memorial Institute
ATTN: Merwyn R. Vanderlind
ATTN: W. Pfeifer

The Boeing Company
ATTN: Brian Lempriere
ATTN: Robert Holmes

Brown Engineering Company, Inc.
ATTN: Ronald Patrick

California Research & Technology, Inc.
ATTN: Ken Kreyenhagen

Calspan Corporation
ATTN: M. S. Holden

Effects Technology, Inc.
ATTN: Robert Wengler

General Electric Company
Space Division
Valley Forge Space Center
ATTN: Phillip Cline
ATTN: A. Martellucci
ATTN: C. Kyriss

DEPARTMENT OF DEFENSE CONTRACTORS (Continued)

General Electric Company
TEMPO-Center for Advanced Studies
ATTN: DASIAC

General Research Corporation
ATTN: Robert E. Rosenthal

Institute for Defense Analyses
ATTN: Joel Bengston
ATTN: IDA Librarian, Ruth S. Smith

ION Physics Corporation
ATTN: Robert D. Evans

Kaman Sciences Corporation
ATTN: Frank H. Shelton
ATTN: Thomas Meagher

Lockheed Missiles & Space Company, Inc.
ATTN: Gerald T. Chrusciel
ATTN: Charles M. Lee
ATTN: Donald A. Price
ATTN: Robert Au

Lockheed Missiles & Space Company
ATTN: T. R. Fortune

Martin Marietta Aerospace
Orlando Division
ATTN: Laird Kinnaird
ATTN: James M. Potts, MP-61
ATTN: William A. Gray, MP-61

McDonnell Douglas Corporation
ATTN: L. Cohen
ATTN: H. Hurwicz
ATTN: R. J. Reck

National Academy of Sciences
ATTN: National Materials Advisory Board for
Donald G. Grove

DEPARTMENT OF DEFENSE CONTRACTORS (Continued)

Pacific-Sierra Research Corp.
ATTN: Gary Lang

Physical Sciences, Inc.
ATTN: M. S. Finson

Physics International Company
ATTN: Doc. Con. for James Shea
ATTN: Doc. Con. for K. Seifert
ATTN: Doc. Con. for D. J. Mumma
ATTN: Doc. Con. for L. Behrman

Prototype Development Associates, Inc.
ATTN: L. Hudack
ATTN: J. E. Dunn

R & D Associates
ATTN: Albert L. Latter
ATTN: Raymond F. Ross
ATTN: F. A. Field

Science Applications, Inc.
ATTN: John Warner

Science Applications, Inc.
ATTN: Lyle Dunbar
ATTN: Carl Swain

Science Applications, Inc.
ATTN: George H. Burghart
ATTN: Ken Kratch

Southern Research Institute
ATTN: C. D. Pears

Stanford Research Institute
ATTN: Donald Curran
ATTN: George R. Abrahamson

Systems, Science and Software, Inc.
ATTN: G. A. Gurtman

TRW Systems Group
ATTN: I. E. Alber, R1-1008
ATTN: Thomas G. Williams
ATTN: W. W. Wood
ATTN: D. H. Baer
ATTN: A. W. Zimmerman

TRW Systems Group
San Bernardino Operations
ATTN: William Polich
ATTN: Earl W. Allen, 520/141
ATTN: V. Blankenship
ATTN: E. Y. Wong, 527/712
ATTN: L. Berger